ABSTRACT

SPAYD, KIMBERLY RENEE. Two Phase Flow in Porous Media: Traveling Waves and Stability Analysis. (Under the direction of Michael Shearer.)

The Buckley-Leverett equation for two phase flow in a porous medium is modified by including dependence of the capillary pressure on the time derivative of saturation. This model, due to Hassanizadeh and Gray, results in a nonlinear pseudoparabolic partial differential equation that includes a mixed third order derivative representing dispersion. Both quadratic and fractional relative permeability functions are considered in the model. Phase plane analysis, including a separation function to measure the distance between invariant manifolds, is used to determine when the equation supports traveling waves corresponding to undercompressive shocks. The Riemann problem for the underlying conservation law is solved in the case of each relative permeability constitutive equation. The structures of the various solutions are confirmed with numerical simulations of the partial differential equation. Specific effects of the mixed third order derivative are investigated in the context of the Benjamin-Bona-Mahony equation modified with a cubic flux function and Burgers term.

Further, the Saffman-Taylor viscous fingering instability is examined and a generalized criterion given for variable saturations. Two dimensional stability of plane wave solutions is governed by the hyperbolic/elliptic system obtained by ignoring capillary pressure, which is diffusive. The growth rate of perturbations of unstable waves is linear in the wave number to leading order. This gives a sharp boundary in the state space of upstream and downstream saturations separating stable from unstable waves. The role of this boundary, derived from the linearized hyperbolic/elliptic system, is verified by numerical simulations of the full nonlinear parabolic/elliptic equations.

Two Phase Flow in Porous Media: Traveling Waves and Stability Analysis

by
Kimberly Renee Spayd

A dissertation submitted to the Graduate Faculty of
North Carolina State University
in partial fulfillment of the
requirements for the Degree of
Doctor of Philosophy

Mathematics

Raleigh, North Carolina

2012

APPROVED BY:

_____   _____
Mansoor Haider   Negash Medhin

_____   _____
Stephen Schecter   Michael Shearer
                                                       Chair of Advisory Committee

DEDICATION

To my beloved family - Chuck Wessell, Rachel Wessell, Michael Spayd and most

especially Shirley Spayd,

without whom this work would not be possible.

Thank you for every bit of your love, support and hard work on my behalf.

BIOGRAPHY

The author obtained her Bachelors degree in Mathematics with a concentration in Applied Mathematics and a minor in Art History from the University of Notre Dame, then a Masters degree in Statistics from the University of North Carolina. Now a Doctorate in Mathematics from North Carolina State University is happily completed.

ACKNOWLEDGEMENTS

TABLE OF CONTENTS

LIST OF FIGURES

Chapter 1

Introduction

A porous medium is a solid mass containing void spaces called pores. Natural and manufactured examples are ubiquitous, ranging from bones and rocks such as granite and limestone to paper, concrete and cloth. Quantitative measures of porous media include porosity and permeability. Porosity, represented by ϕ, is the volume fraction of pore space in the medium:

$$\phi = \frac{\text{pore volume}}{\text{total volume}}.$$

Granite, for example, typically has a low porosity as it has a small amount of void space while cloth, with large pores, has a high porosity. A medium's pore structure determines its permeability: a measure of the ease with which fluids and gases are transmitted through it. The units of measurement are those of area, such as square meters, square centimeters, darcy (approximately 10^{-14} square meters) or millidarcy, as permeability can be determined experimentally by using Darcy's law, Eq. (2.3) [15].

When two fluids, or phases, flow through a porous medium, one of them is more likely to make contact with the solid surface of the medium. This fluid is known as the wetting

phase and the other as the non-wetting phase. Contaminant flow in groundwater is an application of two phase flow in a porous medium [42], the water and pollutant being the two fluid phases and the surrounding solid ground being the porous medium. Another example is the passage of hydrogen and oxygen through a porous filter in a fuel cell.

Arguably, the most historically significant application of two phase flow in porous media is that of secondary oil recovery by water flood, in which water is the wetting phase and oil is the non-wetting phase [15, 49]. Primary oil recovery, relying on high pressures underground, accounts for only approximately fifteen percent of the original oil in the reservoir. Another fifteen to twenty percent can be recovered via secondary methods such as water-flooding, first introduced in the 1940s.

In this process, water is pumped into the porous medium of the reservoir through injection wells, displacing some of the remaining oil, which is forced out of a production well. See Figure 1.1 for an illustration. This method is best suited for crude oil having a relatively low viscosity, since otherwise water breaks through to the production well at an early stage. When the proportion of water in the production fluid eventually becomes too high for profitability, the reservoir is abandoned. It is estimated that approximately a third of the original oil is recovered from primary and secondary methods. Tertiary methods, also known as enhanced oil recovery, include thermal, solvent-based and other chemical approaches [43].

The Buckley-Leverett equation for two phase flow in a homogeneous and isotropic porous medium was formulated in the 1940s to model the dynamics of water and oil, or more generally two immiscible fluids, in porous rock or compacted sand [12]. In its original form, the equation is a first order nonlinear scalar conservation law expressing the unidirectional nonlinear transport of the two phases through a medium with uniform porosity. The variable used to quantify the flow is the saturation of the wetting phase, a

2
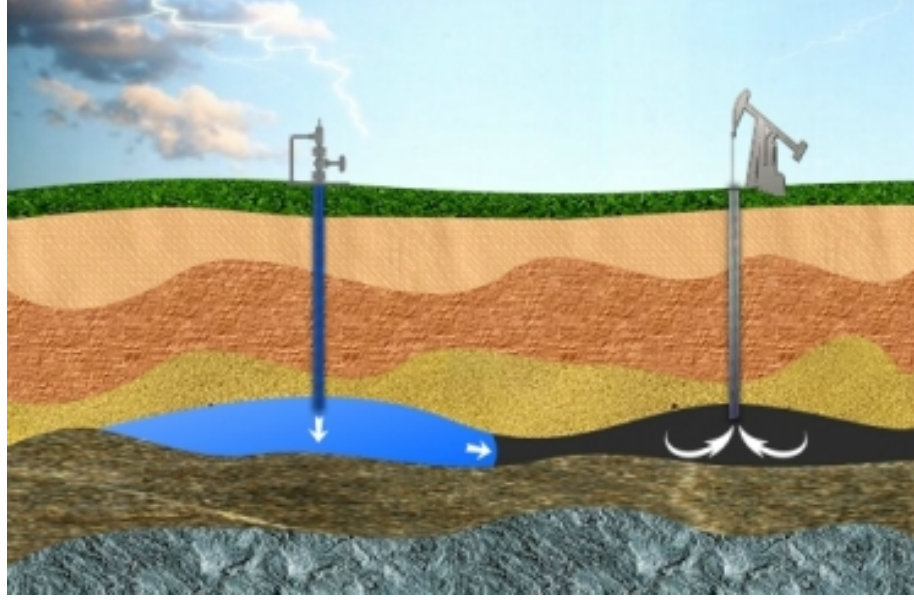
Figure 1.1: Illustration of secondary oil recovery in one dimension; taken from http://www.amerexco.com/recovery.html

volume fraction of the pore space filled by the wetting fluid. Solutions include rarefactions and shock waves which correspond to jumps in the saturation across an interface. In fact, a combination of a rarefaction and shock connect an initial upstream saturation of one and an initial downstream saturation of zero. More recently, versions of the Buckley-Leverett equation have included capillary pressure as a dissipative term [49, 55] which smooths the solutions of the conservation law. This pressure has typically been treated as though interfacial forces equilibrate on a fast time scale, an assumption brought into question by Hassanizadeh and Gray, who formulated a dynamic capillary pressure law [30, 31]. Dynamic capillary pressure is given as the difference between equilibrium capillary pressure and a rate dependent correction involving the time derivative of saturation.

Experimental results from DiCarlo, described in [22], have led to renewed interest in the Buckley-Leverett equation modified by the inclusion of dynamic capillary pressure.

Non-monotonic saturation profiles in the gravity driven infiltration experiments from [22] were unexplained in the regime of classically understood capillary pressure models. Even though DiCarlo's experiments are more suitably modeled by Richards equation for unsaturated flow [25], the results motivated much interest in modifying the Buckley-Leverett equation by including dynamic capillary pressure in the derivation. The rate dependence introduces an additional time derivative, resulting in a dispersive third order derivative that is a nonlinear version of the dispersive term in the Benjamin-Bona-Mahony (BBM) equation [9]. A detailed derivation is given in chapter two. It is interesting to note that in [23], DiCarlo uses further experimental results to debate the role of dynamic capillary pressure, as defined by Hassanizadeh and Gray, in the saturation overshoot observed in [22].

Much of the recent effort has focused on characterizing traveling wave solutions of the so-called *modified* Buckley-Leverett equation under various simplifications and constitutive assumptions [17, 18, 34, 38, 47, 62, 63]. In [63], the authors study a linearized version of the modified Buckley-Leverett equation; the nonlinearity of the regularization terms is neglected in an effort to understand existence and uniqueness properties. In contrast here, traveling wave solutions of the fully nonlinear modified Buckley-Leverett equation are carefully considered in chapter three.

Other works [18, 38, 62] examine the full equation and degeneracies resulting from the use of specific constitutive equations. In [18, 62], existence and non-existence results are given for traveling wave solutions when the model incorporates general relative permeability functions, contrary to the linearized analysis in [63] for which the relative permeability functions are taken to be quadratic. Further, the existence of "sharp" traveling waves is introduced in [62], unique to the regime in which relative permeability functions are fractional instead of quadratic or higher. These sharp fronts are travel-

ing wave solutions between an upstream saturation of one and a nonzero downstream saturation. The topics of fractional relative permeabilities, sharp traveling waves and their impact on the Riemann problem for the modified Buckley-Leverett equation are all addressed in detail in chapter four. Further, numerical codes from [37, 65] are used to illustrate boundaries between solution regions for the Riemann problem and simulate sharp traveling waves.

A striking novel feature of the recent analysis is the presence of traveling waves that are *undercompressive* in the sense of shock waves [33, 39, 46]. Undercompressive shock waves are discontinuous solutions of hyperbolic conservation laws with non-convex non-linear fluxes that fail to satisfy the Lax entropy condition [44], but instead require an additional condition known as a *kinetic relation* [1]. Typically the kinetic relation describes when the shock can be approximated by smooth traveling waves of the conservation law enhanced by additional dissipative and dispersive terms that smooth solutions. Undercompressive traveling waves and their role in the theory of hyperbolic conservation laws have been explored in various contexts [8, 46, 57], both for scalar equations and for systems. It is the presence of undercompressive shocks that captures the non-monotonicity observed in [22].

In addition, other theoretical arguments [5, 6, 59] and experimental results [45, 56, 68] suggest that capillary pressure as well as relative permeability functions depend on time through the saturation rate of change. It is argued, along the same lines as Hassanizadeh and Gray, that there are significant non-equilibrium effects in the process of spontaneous imbibition, introducing a need for relaxation terms in the model. With this hypothesis, Barenblatt *et al.* [5, 6] derive the Buckley-Leverett equation with time dependent dissipation and dispersion. Existence and uniqueness results for traveling wave solutions of their model are presented in [5]. Comparisons between experimental data and simula-

tions in [56] show improved matching when all constitutive equations are rate dependent as opposed to not. There does not appear to be any work which compares experimental results to both types of models: one which only includes rate dependence through capillary pressure and one which includes rate dependence through relative permeabilities and capillary pressure.

While there are many works that address the role of dynamic capillary pressure in the context of the Buckley-Leverett equation, it is difficult to understand the effects analytically due to the complex nonlinearity. To this end, a treatment of the BBM equation is given in chapter five with the amendments of cubic flux and dissipation given by a Burgers term. Jacobs *et al.* [39] provide a detailed and thorough treatment of traveling wave solutions of the modified Korteweg-de Vries-Burgers (KdVB) equation, which is similar to the modified BBM-Burgers equation in all aspects except the rate dependent dispersion. With a cubic flux function, they are able to analytically characterize the existence of undercompressive shocks. When the dispersion term is given by a mixed partial derivative, reflecting the influence of dynamic capillary pressure on the Buckley-Leverett model, it is still possible to describe the existence of undercompressive shocks completely analytically. The resulting formulae are used to solve the Riemann problem for the corresponding conservation law in chapter five.

Early experiments and analysis of stability of fronts in water flood date back to the work of Chouke *et al.* [14], Engelberts and Klinkenberg [26] as well as Hill [35] in the 1950s. Most famously, Saffman and Taylor [52] provide a stability criterion in the circumstance of a less viscous fluid such as water displacing a more viscous fluid such as oil in a Hele-Shaw cell. The criterion states that a sharp front between the fluids suffers a fingering instability (see Figure 1.2) if the mobility of the displacing fluid is less than that of the displaced fluid. Since they consider flow in a Hele-Shaw cell, the effects of

6

porosity are not included in their analysis. For a thorough review of early work in this area, see [36].

Figure 1.2:   Development of the Saffman-Taylor viscous fingering instability for interface between air and glycerine in a Hele-Shaw cell, taken from [52]

In [52], the mobilities are assumed to be constants, since only a sharp front between pure water and pure oil is considered. This condition is realized in a Hele-Shaw cell, in which the fluid displacement involves only uniform saturations (i.e. pure immiscible fluids). However, in a porous medium, while the fluids may reasonably be assumed to remain pure and unmixed in individual pores, the arrangement of the fluids is complex, and saturations, defined as local averages, provide a natural and simple description of the flow.

The sharp interface studied by Saffman and Taylor [52] is a weak solution of the Buckley-Leverett equation, but it is unphysical in the sense that it gives way in one

7

space dimension to the Buckley-Leverett rarefaction-shock, and is therefore unstable to one-dimensional perturbations. In fact, the Saffman-Taylor front fails to satisfy the Lax entropy condition.

Yortsos and Hickernell perform linearized stability analysis of smooth traveling waves for the full two-dimensional system of equations for conservation of mass and incompressibility [66]. Matched asymptotic expansions lead to formulae for the first two terms in the long-wave expansion of the growth rate. Aiming to simplify the stability analysis in [66], Daripa and Pasa [20] make far-field assumptions on the base states of saturation and pressure that substantially simplify the equations of the model. The new approach taken in chapter six yields the same leading order term as in [66] but is considerably simpler than their asymptotic analysis and highlights the hyperbolic nature of the long-wave instability.

Other stability analysis of the two phase flow equations varies widely in method and interest. Barenblatt *et al.* [4] also consider long wave stability analysis in the absence of capillary effects. Their generalized stability criterion is dependent on the total mobilities ahead of and behind the sharp front, as is the result from [66] and chapter six; however, the approach used in [4] relies on solving an equation for the amplitude of a single mode sinusoidal perturbation and does not exploit the hyperbolic properties of the two-dimensional system as in chapter six. With the inclusion of capillary pressure, approximations and numerical investigations appear in [13, 29, 40, 67]. Particular attention is given to the dissipation of short wavelength perturbations in [3] and radial displacement in [10]. The shape and width of viscous fingers is characterized analytically by DiCarlo and Blunt in [24] in a regime for which capillary pressure depends on the velocity of the interface, in this way being dynamic, but not on the time derivative of saturation as in [30, 31].

Simulations of unstable waves, in the context of two phase flow, have been studied by Riaz and Tchelepi [50, 51]. In [50], the authors investigate the roles of viscous, capillary and gravitational forces in generating the fingering instability. Several parameter studies for the widths of the dispersion curves and maximum growth rates are given in [51]. The numerical simulations presented in chapter six confirm analytical results for stable and unstable waves in the case of quadratic relative permeabilities. Additionally in chapter six, comparison plots are given for the growth and decay rates with those predicted by the linear approximation of the dispersion relation and with the prediction of Yortsos and Hickernell in [66].

Chapter 2

Preliminaries

This chapter introduces the model equations in the context of both the two-dimensional hyperbolic/elliptic system and the one-dimensional pseudoparabolic partial differential equation. Traveling waves and their role in the analysis of the one-dimensional model are introduced. Finally, weak solutions of scalar conservation laws are reviewed, along with necessary conditions on shocks pertaining to analysis that follows in later chapters.

2.1   Two Dimensional Flow Equations

The saturation of either phase is defined as the fraction of the pore volume occupied by the phase. It is denoted by u^j where $j = w, n$ is an index for wetting and non-wetting phases, respectively. Assuming that the void space is completely filled by the two phases so that $u^w + u^n = 1$, the saturation of the non-wetting phase can be represented in terms of the saturation of the wetting phase: $u^n = 1 - u^w$. With this in mind, the indices are dropped from the previous notation in favor of u and $1 - u$ representing the saturations of the wetting and non-wetting phases, respectively.

Mass conservation of the wetting phase is represented by the equation

$$\varphi \frac{\partial u}{\partial t} + \nabla \cdot \mathbf{v^w} = 0 \tag{2.1}$$

where ϕ is the porosity of the porous medium and $\mathbf{v^w}$ is the velocity of the wetting phase; the rate of change in the wetting phase saturation is balanced by the spatial flux. Incompressibility of the fluids, i.e. the inability of a representative amount of either fluid to change volume as it moves through the porous medium, is expressed by

$$\nabla \cdot \mathbf{v^T} = 0, \tag{2.2}$$

in which $\mathbf{v}^T = \mathbf{v}^w + \mathbf{v}^n$ is the total velocity. See [2] for a derivation of Eq. (2.2).

Next, Darcy's law for two phase flow relates the phase velocity and pressure gradient by

$$\mathbf{v^j} = -\frac{Kk^j}{\mu^j}\nabla p^j, \tag{2.3}$$

where K is the absolute permeability of the porous medium, k^j is a relative permeability function depending on the phase saturation, μ^j is the phase viscosity and p^j is the phase pressure. The relative permeability functions $k^w(u)$, $k^n(1-u)$ describe how the presence of one phase inhibits the flow of the other. Figure 2.1 from [49] shows experimentally measured relative permeability curves as functions of the wetting saturation u. Note that $k^w(u)$ and $k^n(1-u)$ are both increasing functions of their respective arguments. It is clear that quadratic functions are reasonable approximations [34, 49, 63], although fractional exponents are also used frequently [11, 18, 21, 28, 58, 60]. In much of this analysis (specifically chapters three and six), quadratic relative permeabilities are used to generate specific functional forms. In chapter four, smaller fractional exponents are

11

used in order to satisfy a specific integrability condition from [18]. For ease of notation, let

$$\lambda^w(u) = \frac{Kk^w(u)}{\mu^w}, \quad \lambda^n(u) = \frac{Kk^n(1-u)}{\mu^n}, \tag{2.4}$$

referred to as phase mobility functions. Then $\lambda^T = \lambda^w + \lambda^n$ is the total mobility of the two phases.

(a)   (b)
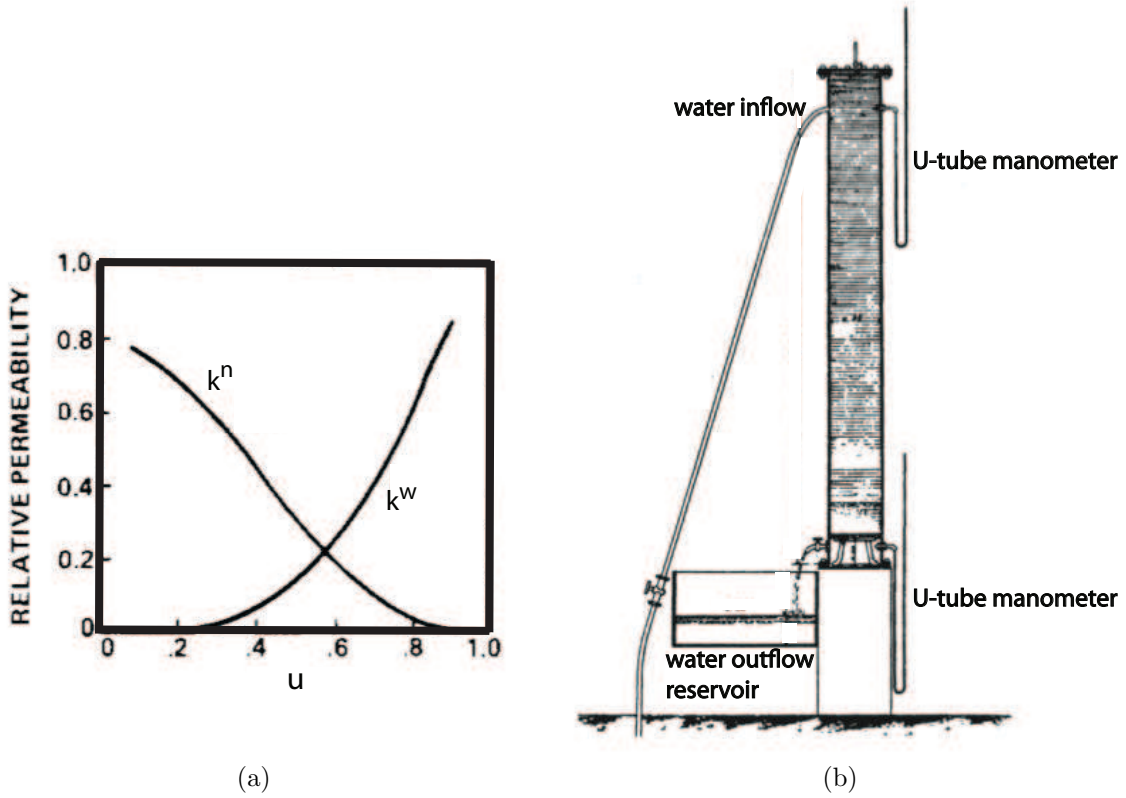
Figure 2.1: (a) Experimentally measured relative permeability curves as functions of wetting phase saturation; taken from [49]   (b) Darcy's experimental design showing column of packed sand, water inflow and outflow reservoir, U-tube manometers at top and bottom to measure flow rates and pressures; taken from [7]

Henri Darcy was the water engineer in Dijon, France in the middle of the 19th century.

He performed various experiments regarding single phase flow, specifically water through a vertical column filled with homogeneous packed sand. His experimental set-up is illustrated in Figure 2.1 by his own sketch [7]. After injecting water into the column from the top, he measured the flow rate and pressures at the top and bottom using U-tube manometers. From the data collected, he formulated an empirical law stating that the fluid velocity is linearly dependent on the pressure difference. Formally, on a continuum scale, Darcy's law for single phase flow, $\mathbf{v} = -\frac{K}{\mu}\nabla p$, is derived from the Navier-Stokes equations [7] and is a momentum balance equation. Darcy's law for two phases, Eq. (2.3), includes relative permeability functions, k^j, since the two phases affect each other's flow.

At the microscopic level, consider an individual pore in the medium which contains an interface between the wetting and non-wetting phases. The curvature of such an interface and the resulting surface tension yield different pressures in each phase. Capillary pressure, p^c, is defined as the difference of the phase pressures and is related to surface tension and curvature through the Young–Laplace equation

$$p^c = p^n - p^w = \frac{2\gamma}{R},\tag{2.5}$$

where γ is the interfacial (surface) tension of the interface between the two phases and R is the radius of curvature of the surface. Averaging over many local pores introduces saturation of the wetting phase as a natural measure of fluid flow at the continuum level. In this way, capillary pressure becomes a function of saturation and has a dissipative effect on sharp solutions of the governing equations, Eq. (2.1) and Eq. (2.2).

Substituting Eq. (2.3) into both Eq. (2.1) and Eq. (2.2), then factoring out a negative

sign gives

$$\varphi \frac{\partial u}{\partial t} - \nabla \cdot (\lambda^w(u)\nabla p^w) = 0 \qquad (2.6)$$

$$\nabla \cdot (\lambda^w(u)\nabla p^w + \lambda^n(u)\nabla p^n) = 0. \qquad (2.7)$$

Adding and subtracting $\lambda^n(u)\nabla p^w$ to Eq. (2.7) then factoring appropriately allows p^n to be eliminated from Eq. (2.7) (using Eq. (2.5)):

$$\nabla \cdot \left(\lambda^T(u)\nabla p^w + \lambda^n(u)\nabla p^c(u)\right) = 0. \qquad (2.8)$$

Now p^n is not an additional variable in the model and p^c is a function of saturation, u. Thus the two dimensional system for two phase flow in a porous medium that will be considered throughout this work is comprised of Eq. (2.6), a hyperbolic PDE for mass conservation, and Eq. (2.8), an elliptic PDE for incompressibility. Stability analysis of this two dimensional system is given in chapter six while the one dimensional model (developed in the next section) is considered in chapters three and four.

2.2   The Modified Buckley-Leverett Equation

In one dimension, Eq. (2.1), Eq. (2.2), Eq. (2.3) and Eq. (2.5) combine into a scalar PDE known as the Buckley-Leverett equation. Starting with capillary presssure, the spatial derivative of Eq. (2.5) is $p^c(u)_x = p^n_x - p^w_x$. Then Eq. (2.3) is used to replace the phase pressures:

$$p^c(u)_x = -\frac{v^n}{\lambda^n(u)} + \frac{v^w}{\lambda^w(u)}. \qquad (2.9)$$

14

The velocity of the nonwetting phase is eliminated by using the total velocity v^T, a constant parameter which sets the velocity scale from Eq. (2.2). Now, in one dimension, $\frac{d}{dx} v^T = 0$ and so v^T is a scalar. Then $v^n = v^T - v^w$ and Eq. (2.9) becomes

$$
\begin{aligned}
p^c(u)_x &= -\frac{v^T - v^w}{\lambda^n(u)} + \frac{v^w}{\lambda^w(u)} \\
&= -\frac{v^T}{\lambda^n(u)} + \frac{\lambda^w(u) + \lambda^n(u)}{\lambda^w(u)\lambda^n(u)} v^w
\end{aligned}
$$

Thus the velocity of the wetting phase is expressed in terms of the phase mobilities, total velocity and capillary pressure:

$$
v^w = \frac{\lambda^w(u)}{\lambda^T(u)} v^T + \frac{\lambda^n(u)\lambda^w(u)}{\lambda^T(u)} p_x^c. \tag{2.10}
$$

Now Eq. (2.10) is substituted into the one-dimensional version of Eq. (2.1)

$$
\phi u_t + \left(\frac{\lambda^w(u)}{\lambda^T(u)} v^T + \frac{\lambda^n(u)\lambda^w(u)}{\lambda^T(u)} p_x^c \right)_x = 0
$$

to obtain the Buckley-Leverett equation

$$
\phi u_t + v^T f(u)_x = - \left(\frac{K}{\mu^n} H(u) p_x^c \right)_x. \tag{2.11}
$$

In this equation, the flux, $f(u)$, is a fractional flow rate given by

$$
f(u) = \frac{\lambda^w(u)}{\lambda^T(u)} = \frac{k^w(u)}{k^w(u) + m k^n(1-u)}, \tag{2.12}
$$

15

in which $m = \mu^w/\mu^n$ and the function

$$H(u) = \frac{k^w(u)k^n(1-u)}{k^w(u) + mk^n(1-u)} \qquad (2.13)$$

is known as the capillary induced diffusion coefficient [18].

In [30, 31], Hassanizadeh and Gray propose a macroscopic constitutive equation for capillary pressure that is rate dependent. Instead of averaging microscopic quantities from Eq. (2.5) over a representative elementary volume, they use balance equations for energy, mass and momentum at the macroscopic level to develop a constitutive theory that explicitly includes saturation of the wetting phase along with other intrinsic properties of the porous medium. Specifically, they provide a non-equilibrium equation for capillary pressure, known as dynamic capillary pressure

$$p^c(u, u_t) = p^c_e(u) - \frac{1}{\Pi^w}\frac{\partial u}{\partial t} \qquad (2.14)$$

in which $p^c_e(u)$ is the equilibrium capillary pressure and Π^w is a positive material coefficient. This linear rate dependence on saturation is the lowest order correction to include dynamic effects; note that, at equilibrium, Eq. (2.14) is equivalent to an averaged macroscopic version of Eq. (2.5).

In 2004, DiCarlo observed non-monotonic saturation profiles, as seen in Figure 2.2, in infiltration experiments described in [22]. This unexplained behavior was the impetus for van Duijn, Peletier, Pop and others to incorporate dynamic capillary pressure, as given by Eq. (2.14), into two phase flow models [17, 18, 34, 38, 47, 63, 62].

With the introduction of dynamic capillary pressure, the derivation of the Buckley-
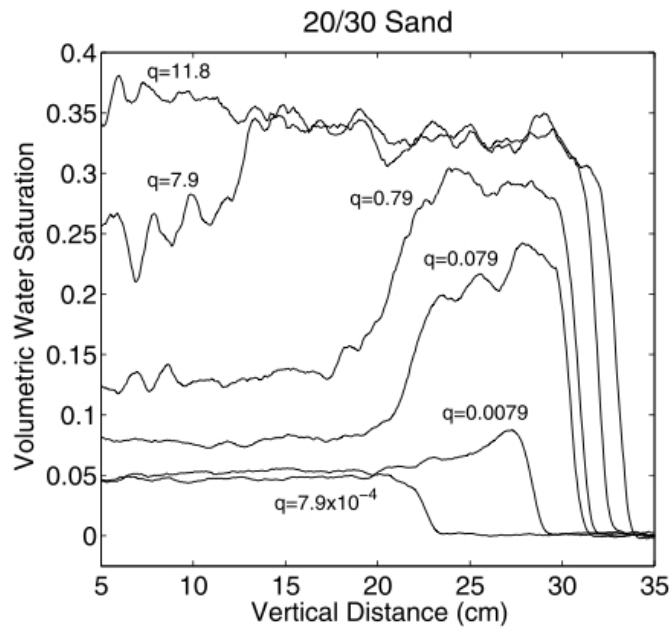
Figure 2.2: Experimentally determined saturation profiles for varying applied flux values, q (related to initial water saturation and velocity), at the top boundary; taken from [22]

Leverett equation is altered. Now, Eq. (2.9) is replaced by

$$p_e^c(u)_x - \frac{1}{\Pi^w} u_{xt} = -\frac{v^n}{\lambda^n(u)} + \frac{v^w}{\lambda^w(u)}$$

so that Eq. (2.10) becomes

$$v^w = \frac{\lambda^w}{\lambda^T} v^T + \frac{\lambda^w \lambda^n}{\lambda^T} \left(p_e^c(u) - \frac{1}{\Pi^w} u_t \right)_x. \qquad (2.15)$$

Next, Eq. (2.15) is substituted into Eq. (2.1):

$$\phi u_t + \left(\frac{\lambda^w}{\lambda^T} v^T \right)_x = -\left[\frac{\lambda^w \lambda^n}{\lambda^T} \left(p_e^c(u) - \frac{1}{\Pi^w} u_t \right)_x \right]_x. \qquad (2.16)$$

Note that Eq. (2.16) differs from Eq. (2.11) with the presence of the nonlinear dispersion term on the right hand side. Thus the rate dependence in the constitutive equation for dynamic capillary pressure influences the Buckley-Leverett equation through the regularization.

To nondimensionalize Eq. (2.16) (as in [47]), characteristic time and length scales are introduced: $x = L\bar{x}$ and $t = T\bar{t}$, where the bar notation denotes a dimensionless variable. Then Eq. (2.16) becomes

$$\frac{\phi}{T} u_{\bar{t}} + \frac{v^T}{L} f(u)_{\bar{x}} = -\frac{K}{\mu^n L^2} \left[H(u) \left(p_e^c(u) - \frac{1}{\Pi^w T} u_{\bar{t}} \right)_{\bar{x}} \right]_{\bar{x}}.$$

The following equalities are obtained by balancing coefficients:

$$\frac{\phi}{T} = \frac{v^T}{L} = \frac{K}{\mu^n L^2}.$$

18

The characteristic time scale is thus determined to be $T = \frac{L\phi}{v^T} = \frac{\phi\mu^n L^2}{K}$. Now, the dimensionless dispersion coefficient is denoted by $\tau = \frac{1}{\Pi^w T} = \frac{K}{\Pi^w L^2 \phi\mu^n}$ and is included in the *modified Buckley-Leverett equation* (bars omitted):

$$u_t + f(u)_x = -\left[H(u) \left(p_e^c(u) - \tau u_t \right)_x \right]_x, \tag{2.17}$$

which will be considered in depth in chapters three and four. The equilibrium capillary pressure p_e^c has been scaled by a typical pressure $\bar{p} = \frac{v^T L \mu^w}{K}$, and is now dimensionless.

As previously mentioned, the relative permeability functions $k^w(u)$, $k^n(1-u)$ are often assumed to be quadratic in the work presented here. Specifically, let $k^j(u) = \kappa^j u^2$, where $\kappa^j > 0$ is constant. Then $f(u)$ and $H(u)$ have the functional forms

$$f(u) = \frac{u^2}{u^2 + M(1-u)^2}, \qquad H(u) = \frac{\kappa^n u^2 (1-u)^2}{u^2 + M(1-u)^2}, \qquad M = \frac{\kappa^n}{\kappa^w} m.$$

The flux function, $f(u)$, is convex-concave with a single inflection point at some $u_I \in (0,1)$ [27]. The shape of $f(u)$ is significant when describing the hyperbolic wave structure of solutions, as in [46]. Graphs of these functions are shown in Figure 2.3 for $\kappa^n = 1$ and various values of M. In their original paper [12], Buckley and Leverett use $M = 0.5$. However, $M = 2$ can be regarded as a representative choice [63] and is used throughout chapters three and four. In this case, $u_I = 0.613$.

The equilibrium capillary pressure, $p_e^c(u)$, is generally taken to be a smooth and decreasing function of saturation [49]. For simplicity, it is taken to be linear here: $p_e^c(u) = -u$. Then Eq. (2.17) becomes

$$u_t + f(u)_x = \left[H(u) \left(u_x + \tau u_{xt} \right) \right]_x. \tag{2.18}$$
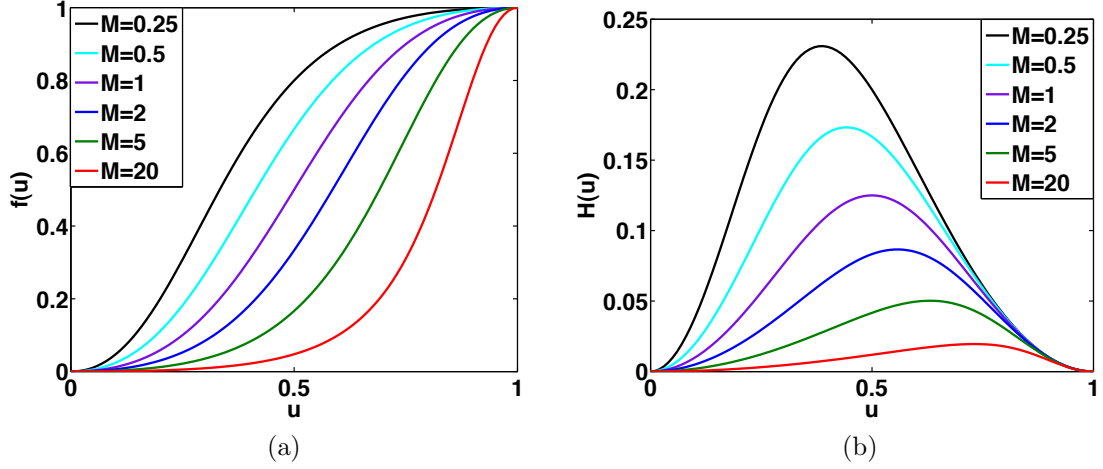
Figure 2.3: (a) Fractional flow rate $f(u)$ (b) Capillary induced diffusion coefficient $H(u)$ in Eq. (2.17)

Linearizing about a constant $u = u_e$, a linear PDE is obtained for the perturbation $v(x, t)$ of u_e :

$$v_t + f'(u_e)v_x = H(u_e)(v_{xx} + \tau v_{xxt}).$$ (2.19)

Solutions of Eq. (2.19) of the form $v = e^{\lambda t} e^{ikx}$ are specified by the dispersion relation

$$\lambda + ikf'(u_e) = -k^2 H(u_e) - \lambda k^2 \tau H(u_e).$$

Thus,

$$\lambda = -ik\frac{f'(u_e)}{1 + k^2\tau H(u_e)} - \frac{k^2 H(u_e)}{1 + k^2\tau H(u_e)}.$$

Let $c(k) = \dfrac{f'(u_e)}{1 + k^2\tau H(u_e)}$ and $\mu(k) = \dfrac{k^2 H(u_e)}{1 + k^2\tau H(u_e)}$. Then

$$v = e^{ik(x-c(k)t)} e^{-\mu(k)t}.$$

Thus the solution has wave speed $c(k)$ bounded above by the characteristic speed $f'(u_e)$ for all k. Moreover, $\mu(k) \to 1/\tau$ as $k \to \infty$, suggesting that τ is akin to a relaxation time.

2.3 Traveling Waves

A traveling wave solution of Eq. (2.18) is of the form $u(x,t) = \tilde{u}(\eta)$, $\eta = x - st$. Substitution into Eq. (2.18) gives the third order ODE (omitting tildes)

$$-su' + (f(u))' = [H(u)u']' - s\tau \left[H(u)u''\right]' \tag{2.20}$$

where $' = d/d\eta$. Integrating Eq. (2.20) with boundary conditions

$$u(\pm\infty) = u_{\pm}, \quad u'(\pm\infty) = 0, \quad u''(\pm\infty) = 0, \tag{2.21}$$

leads to the second order ODE

$$-s(u - u_-) + f(u) - f(u_-) = H(u)u' - s\tau H(u)u'', \tag{2.22}$$

together with the Rankine-Hugoniot condition

$$-s(u_+ - u_-) + f(u_+) - f(u_-) = 0. \tag{2.23}$$

As in [63], it is convenient to write $\hat{u}(\xi) = u(\eta)$ where $\xi = \eta/\sqrt{s\tau}$. Then Eq. (2.22) becomes (hats omitted)

$$H(u)u'' - \frac{H(u)}{\sqrt{s\tau}}u' - s(u - u_-) + f(u) - f(u_-) = 0, \tag{2.24}$$

where $' = d/d\xi$. Equation (2.24) is written as a first order system of ODEs:

$$u' = v \tag{2.25a}$$

$$v' = \frac{1}{\sqrt{s\tau}}v + \frac{1}{H(u)}\left[s(u - u_-) - f(u) + f(u_-)\right]. \tag{2.25b}$$

Traveling waves correspond to heteroclinic orbits between equilibria $(u_\pm, 0)$ of system (2.25), analyzed in detail in chapter three.

2.4 Rarefactions and Shocks

A scalar conservation law is obtained when the right hand side of Eq. (2.17) is set to zero:

$$u_t + f(u)_x = 0. \tag{2.26}$$

The two types of weak solutions of Eq. (2.26) are reviewed in this section.

Definition A *rarefaction wave* is a continuous weak solution of Eq. (2.26) and has the form

$$u(x, t) = \begin{cases} u_- & \text{if } x < f'(u_-)t \\ r(\frac{x}{t}) & \text{if } f'(u_-)t \leq x \leq f'(u_+)t \\ u_+ & \text{if } x > f'(u_+)t \end{cases}$$

where $u_\pm$ are the initial downstream and upstream saturations, respectively, and $u = r(\xi)$ is defined by $f'(u) = \xi$. Note that this makes sense if $f'(u)$ is increasing from $f'(u_-)$ to $f'(u_+)$.

Definition A *shock wave* from u_- to u_+ with speed s is a discontinuous weak solution of Eq. (2.26) and has the form

$$u(x,t) = \begin{cases} u_- & \text{if } x < st \\ u_+ & \text{if } x > st, \end{cases}$$

where s is defined by the Rankine-Hugoniot condition (Eq. (2.23)) as the slope of the chord connecting the points $(u_-, f(u_-))$ and $(u_+, f(u_+))$ on the flux curve.

Only constant values of $u_\pm$ and s are considered here; more generally, $u_\pm$ would be one-sided limits at a discontinuity $x = \tilde{x}(t)$ with speed $s(t) = \tilde{x}'(t)$.

Definition A shock from u_- to u_+ with speed s is *admissible* if there exists a solution $(u,v)(\xi)$ of Eq. (2.25) such that $(u,v)(\pm\infty) = (u_\pm, 0)$.

Two types of shock solutions are analyzed throughout this work: Lax and undercompressive. A Lax shock satisfies the Lax entropy condition [44]

$$f'(u_+) \le s \le f'(u_-), \tag{2.27}$$

so that characteristics $x(t) = f'(u_\pm)t + x_0$ converge on the shock from each side. This type of shock is illustrated in Figure 2.4a. Because the flux function $f(u)$ changes concavity, there are admissible shocks which violate Eq. (2.27). See Figure 2.4b. Such a shock is known as undercompressive [39] since characteristics converge on the shock only from

23

ahead of the wave. The presence of these undercompressive shocks is the novel feature of the one-dimensional model and is discussed in detail in the following chapter.
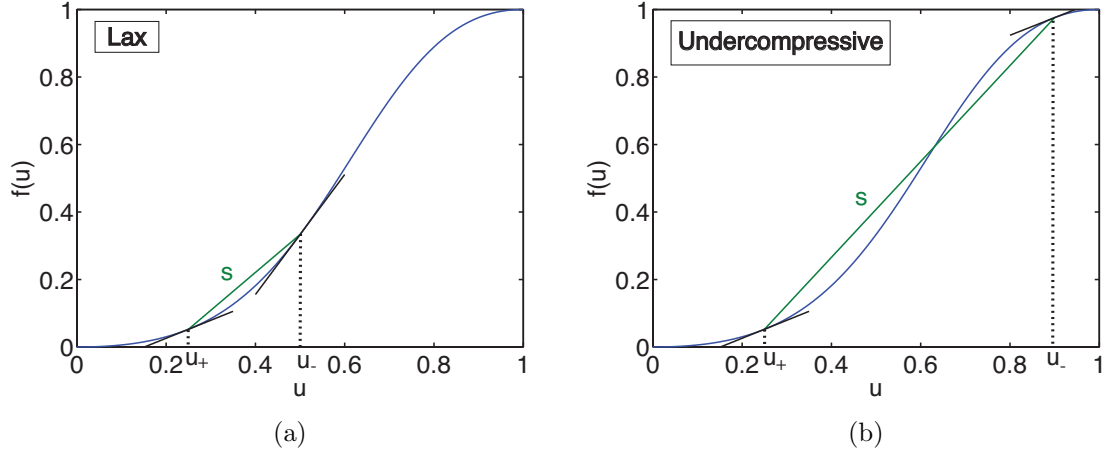
Figure 2.4: (a) Shock solution of Eq. (2.26) which satisfies the Lax entropy condition, Eq. (2.27) (b) Undercompressive shock solution of Eq. (2.26)

Chapter 3

The Modified Buckley-Leverett Equation with Quadratic Relative Permeabilities

The focus of this chapter is on the one-dimensional model with dynamic capillary pressure and quadratic relative permeability functions. Under these assumptions, the modified Buckley-Leverett equation has the form

$$u_t + f(u)_x = [H(u)\,(u_x + \tau u_{xt})]_x,\qquad(3.1)$$

with

$$f(u) = \frac{u^2}{u^2 + M(1-u)^2}, \qquad H(u) = \frac{\kappa^n u^2(1-u)^2}{u^2 + M(1-u)^2}.$$

Without loss of generality, $\kappa^n \equiv 1$ throughout this chapter. Recall from chapter two that the corresponding ODE system for a traveling wave, $u(\eta)$ with $\eta = x - st$, is

$$u' = v \tag{3.2a}$$

$$v' = \frac{1}{\sqrt{s\tau}}v + \frac{1}{H(u)}\left[s(u - u_-) - f(u) + f(u_-)\right]. \tag{3.2b}$$

In what follows, system (3.2) is analyzed in depth as a means to solving the Riemann problem for the hyperbolic conservation law associated with Eq. (3.1). In particular, phase portraits of system (3.2) are studied and used to determine when there is a heteroclinic orbit between saddle equilibria. The values of $u_\pm$ for which there is such an orbit form a curve in the $u_\pm$ plane; certain properties of these curves are proven rigorously. Finally, solutions of the Riemann problem are presented, along with numerical simulations to verify the theoretical findings.

3.1 Equilibria and Phase Portraits

Equilibria for system (3.2) are points $(u, v) = (u, 0)$, where $s(u - u_-) = f(u) - f(u_-)$; these correspond to points of intersection between the graph of $f(u)$ and the line with slope s through $(u_-, f(u_-))$. In particular, for the shock wave

$$u(x, t) = \begin{cases} u_- & \text{if } x < st \\ u_+ & \text{if } x > st, \end{cases}$$

$(u_\pm, 0)$ are equilibria. When there are three equilibria, they will be denoted with the notation $u_{bot} < u_{mid} < u_{top}$.

The Jacobian of Eq. (3.2),

$$J(u, 0) = \begin{pmatrix} 0 & 1 \\ \dfrac{s - f'(u)}{H(u)} & \dfrac{1}{\sqrt{s\tau}} \end{pmatrix},$$

has eigenvalues

$$\lambda_\pm = \frac{1}{2} \left\{ \frac{1}{\sqrt{s\tau}} \pm \sqrt{\frac{1}{s\tau} + 4\frac{s - f'(u)}{H(u)}} \right\}. \tag{3.3}$$

Consequently, the outside equilibria, $u = u_{bot}$ and $u = u_{top}$, are saddle points since $f'(u) < s$. The middle equilibrium u_{mid} is an unstable node or spiral since $f'(u_{mid}) > s$.

Definition A *saddle-saddle connection* from u_- to u_+ is a heteroclinic orbit from $(u_-, 0)$ to $(u_+, 0)$ when $(u_\pm, 0)$ are saddle point equilibria of system (3.2).

When $u_{bot} = u_- < u_{top} = u_+$, this saddle-saddle connection occurs in the upper half plane. On the other hand, when $u_{bot} = u_+ < u_{top} = u_-$, the connection lies in the lower half plane. Note that homoclinic orbits are possible only as $\tau = \infty$ since the system is conservative only in this limit.

For each $u_- \in [0, 1]$, consider the equation

$$f'(u) = \frac{f(u) - f(u_-)}{u - u_-}, \quad 0 < u < 1. \tag{3.4}$$

Lemma 3.1.1. *Suppose $f : [0, 1] \to [0, 1]$ is continuous and C^4 on $(0, 1)$. Suppose further that $f'(0) = f'(1) = 0$, $(u - u_I)f''(u) < 0$ for $u \neq u_I$ and $f'''(u_I) < 0$. Then there is a*

continuous function $u_\alpha : [0, 1] \to [0, 1]$ *that is* C^4 *on* $(0, 1)$ *such that for each* $u_- \neq u_I$, $u = u_\alpha(u_-)$ *is the unique solution of Eq. (3.4); moreover,* $u_\alpha(u_I) = u_I$, *and* $u'_\alpha(u_I) = -\frac{1}{2}$.

Proof. Let

$$g(u_-, y) := f'(y)(y - u_-) - f(y) + f(u_-) \tag{3.5}$$

with $u_-, y \in (0, 1)$. Without loss of generality, assume $u_- < u_I \leq y$. The existence of $u_\alpha(u_-)$ will be shown first. By the Mean Value Theorem, $f'(z) = \dfrac{f(y) - f(u_-)}{y - u_-}$ for some z depending on y with $u_- < z < y$. Letting $y = u_-$, then $f'(z) < f'(u_I)$ for all z, $u_- < z < u_I$ so that $f'(u_I) > \dfrac{f(u_I) - f(u_-)}{u_I - u_-}$. Thus $g(u_-, u_I) > 0$. On the other hand, if $y = 1$, then $f'(z) > f'(1) = 0$ so that $g(u_-, 1) < 0$. By continuity, there is a value $u_\alpha(u_-) \in (u_I, 1)$ such that $g(u_-, u_\alpha(u_-)) = 0$. Uniqueness follows from the inequality

$$\frac{\partial g}{\partial y} = (y - u_-)f''(y) < 0 \qquad \text{for } y > u_I. \tag{3.6}$$

Repeatedly differentiating Eq. (3.5) and evaluating at $u_- = y = u_I$ leads to $u'_\alpha(u_I) = -\dfrac{1}{2}$. Regularity follows from Eq. (3.6) and the Implicit Function Theorem except at $u_- = u_I$ where the proof involves taking limits. This completes the proof of Lemma 3.1.1. $\square$

The range of the continuous function u_α is an interval $I_\alpha = \{u_\alpha(u_-) : u_- \in [0, 1]\}$. Let $u_\gamma : I_\alpha \to [0, 1]$ be the inverse of u_α. Then $u_+ = u_\gamma(u_-)$ gives the intersection of the tangent through $(u_-, f(u_-))$ with the graph of $f(u)$ (where this intersection is in the unit interval):

$$f'(u_-) = \frac{f(u_\gamma(u_-)) - f(u_-)}{u_\gamma(u_-) - u_-}. \tag{3.7}$$

Figure 3.1b shows the curves A and B defined by $A = \{(u_\alpha(u_+), u_+) : u_+ \in [0, 1]\}$, $B = \{(u_-, u_\alpha(u_-)) : u_- \in [0, 1]\}$. The regions between these curves represent pairs (u_-, u_+) for which system (3.2) has three equilibria and $u_\pm$ are the saddle points.
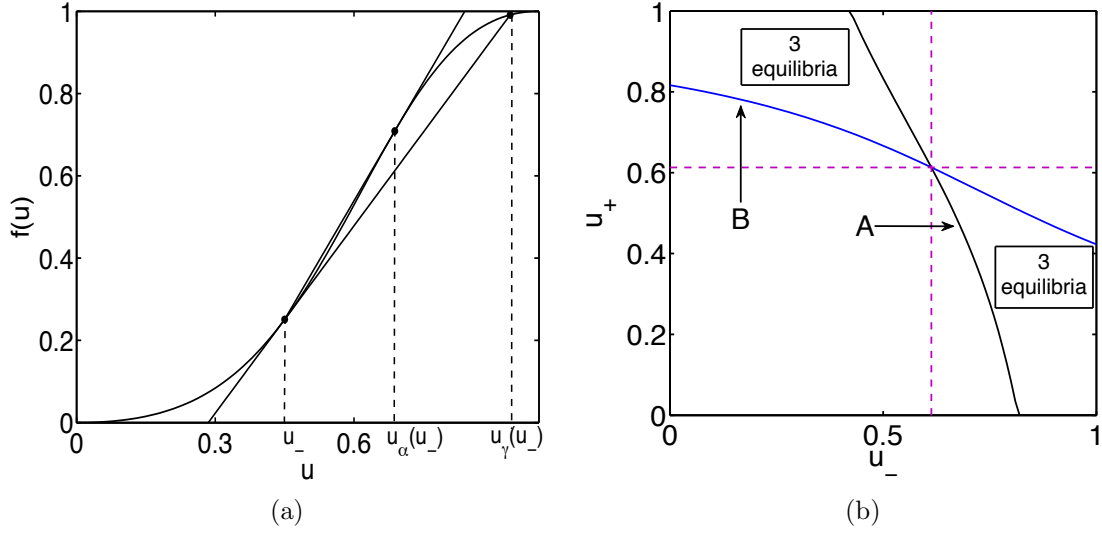
Figure 3.1: Values of $u_\pm$ for which there are three equilibria of Eq. (3.2); (a) Definitions of $u_\alpha(u_-)$, $u_\gamma(u_-)$ on flux function curve, (b) Graphs A, B of functions $u_\gamma(u_-)$, $u_\alpha(u_-)$, respectively.

Various phase portraits for which system (3.2) has two or three equilibria are illustrated in Figure 3.2. The first three portraits in Figure 3.2 show three equilibria; the outside two are saddles while the middle is an unstable node. The trajectories connecting u_{mid} to u_{bot} and u_{mid} to u_{top} in Figure 3.2a correspond to admissible Lax shocks with $u_- = u_{mid}$. However, in Figure 3.2b, there is no trajectory from u_{mid} to u_{top}, even though $u_- = u_{mid}$, $u_+ = u_{top}$ satisfy the Lax entropy condition, Eq. (2.27). Figure 3.2c illustrates a saddle-saddle connection corresponding to an admissible undercompressive shock between $u_{bot} = u_-$ and $u_{top} = u_+$. This case separates those shown in Figure 3.2a and Figure 3.2b.

Given a pair $(u_-, u_+ = u_\gamma(u_-))$ on curve A, system (3.2) has only two equilibria: a degenerate saddle-node at u_- and a saddle at u_+. The two possible phase portraits for such a pair with $u_- < u_I$ are shown in Figures 3.2d, 3.2e. As $u_{bot} = u_-$ and u_{mid}

29

approach each other, Figure 3.2a becomes Figure 3.2d, with the connection between u_{mid} and $u_{top} = u_+$ being preserved, and Figure 3.2b transforms into Figure 3.2e. Between these two cases is a limiting version of Figure 3.2c in which $u_{mid} = u_{bot}$. In contrast to Figure 3.2d there are no trajectories from $(u_{bot}, 0)$ above the stable manifold of $(u_{top}, 0)$.

3.2   Separation Function

In this section, a separation function $R(\nu)$ is defined for each value of the parameters $\nu = (\beta, s, u_-, M)$ where $\beta = 1/\sqrt{s\tau}$. Zeroes of the separation function determine parameters for which there is a saddle-saddle trajectory from u_- to u_+, where $u_+ \neq u_-$ depends on u_- and s through the Rankine-Hugoniot condition, Eq. (2.23). The separation function R, defined in [33, 54], measures a distance between the unstable manifold emanating from $(u_-, 0)$ and the stable manifold entering $(u_+, 0)$.

Let $\phi = (u, v)$. The notation $\nu^0 = (\beta^0, s^0, u_-^0, M^0)$ and $\phi^0 = (u^0, v^0)$ is used to represent specific values of the parameters and variables. Let $K(\phi; \nu)$ denote the vector field in system (3.2):

$$K(\phi; \nu) = \begin{pmatrix} v \\ \beta v + \frac{1}{H(u)}(s(u - u_-) - f(u) + f(u_-)) \end{pmatrix}.$$

Suppose that for a particular β^0 and pair $u_\pm^0$ (with $u_-^0 < u_+^0$), there is a saddle-saddle connection from u_-^0 to u_+^0 and let $\phi^0(\xi) = (u^0, v^0)(\xi)$ be the corresponding trajectory. That is, $\phi^0(\xi)$ is a solution of system (3.2) with boundary values $\phi^0(\pm\infty) = (u_\pm^0, 0)$. For parameter values ν near ν^0, there are saddle points $(u_\pm, 0)$ near $(u_\pm^0, 0)$; the solution of system (3.2) along the unstable manifold of the saddle equilibrium at u_- is represented by $\phi_-(\xi; \nu)$ and similarly $\phi_+(\xi; \nu)$ is the solution along the stable manifold of $(u_+, 0)$. It

30
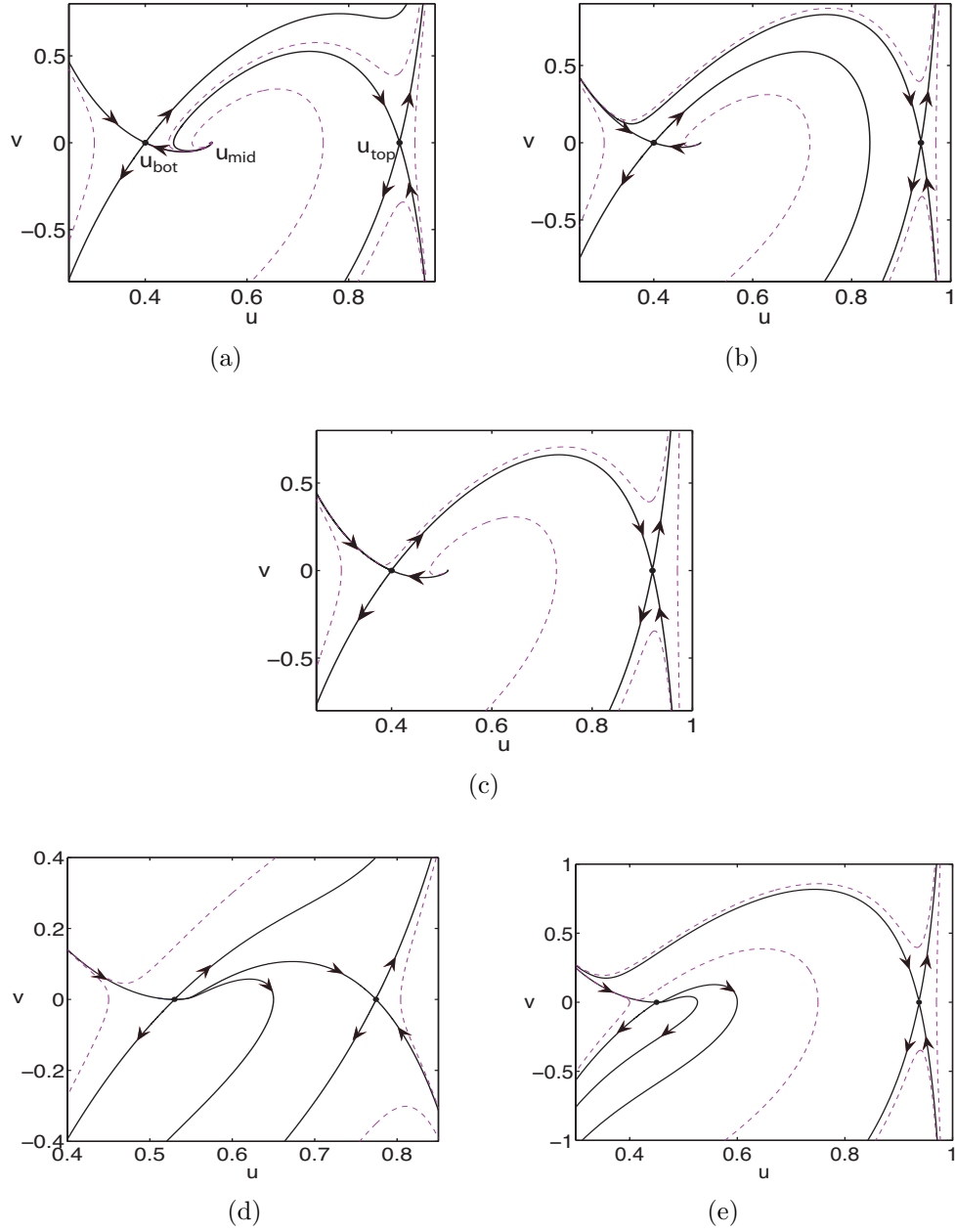
Figure 3.2: Phase portraits of system (3.2) with $M = 2, \tau = 0.1$ for various pairs (u_-, u_+) in the region marked "3 equilibria" in Figure 3.1b, with $u_- < u_I$. (a) The unstable manifold from $u_- = u_{bot}$ is above the stable manifold at $u_+ = u_{top}$. (b) The unstable manifold from u_- is below the stable manifold into u_+. (c) Saddle-saddle connection from u_- to u_+. (d) A single trajectory from the degenerate saddle-node at u_- connects to the saddle at u_+. (e) There is no connection between the degenerate saddle-node at u_- and the saddle at u_+.

31

is required that $\phi_\pm \in C^1$ in both ξ and ν (near ν^0) and that $\phi_\pm$ satisfy:

$$\phi_-(\xi, \nu^0) = \phi^0(\xi), \ \xi \in (-\infty, 0]; \qquad \phi_+(\xi, \nu^0) = \phi^0(\xi), \ \xi \in [0, \infty);$$

$$\phi_-(-\infty; \nu) = (u_-, 0); \qquad \phi_+(\infty; \nu) = (u_+, 0).$$

Let $y(\xi) = K(\phi_-(\xi; \nu), \nu) \times \partial_\theta \phi_-(\xi; \nu)$ where $\theta = \beta$, s, u_- or M. (The product $U \times V$ means the 2×2 determinant formed from column vectors U, V.) Then, using the fact that $K = \partial_\xi \phi$,

$$
\begin{aligned}
\frac{dy}{d\xi} &= \left(\frac{\partial K(\phi_-, \nu)}{\partial \phi_-} \frac{\partial \phi_-(\xi; \nu)}{\partial \xi} \right) \times \frac{\partial \phi_-(\xi; \nu)}{\partial \theta} + K \times \frac{\partial^2 \phi_-(\xi; \nu)}{\partial \theta \partial \xi} && (3.8) \\
&= \partial_{\phi_-} K \partial_\xi \phi_- \times \partial_\theta \phi_- + K \times \left(\partial_{\phi_-} K \partial_\theta \phi_- + \partial_\theta K \right) && (3.9) \\
&= \partial_{\phi_-} K \partial_\xi \phi_- \times \partial_\theta \phi_- + \partial_\xi \phi_- \times \partial_{\phi_-} K \partial_\theta \phi_- + K \times \partial_\theta K && (3.10) \\
&= \left(\mathrm{tr} \partial_{\phi_-} K \right) \left(K \times \partial_\theta \phi_- \right) + K \times \partial_\theta K && (3.11) \\
&= \beta y + r(\xi) && (3.12)
\end{aligned}
$$

where $r(\xi) = K(\phi_-(\xi; \nu), \nu) \times \partial_\theta K(\phi_-(\xi; \nu), \nu)$. Equation (3.12) is a linear differential equation and is solved by using the integrating factor $e^{-\beta \xi}$:

$$y(0) = \int_{-\infty}^0 e^{-\beta \xi} r(\xi) d\xi. \tag{3.13}$$

The separation function is defined as $R(\nu) = K(\phi^0(0), \nu^0) \times (\phi_-(0; \nu) - \phi_+(0; \nu))$; then Eq. (3.13) and the corresponding formula for ϕ_+ give

$$\frac{\partial R}{\partial \theta}(\nu^0) = \int_{-\infty}^\infty e^{-\beta \xi} \left(K(\phi^0(\xi), \nu^0) \times \frac{\partial K}{\partial \theta}(\phi^0(\xi), \nu^0) \right) d\xi \tag{3.14}$$

for each parameter θ.

Next, Eq. (3.14) is used to calculate the sign of each of the derivatives of $R(\nu)$ with respect to the parameters β, u_-, s. First, let $\theta = \beta$. Then

$$\frac{\partial K}{\partial \beta} = \begin{pmatrix} 0 \\ v \end{pmatrix}, \qquad K \times \frac{\partial K}{\partial \beta} = v^2.$$

Consequently,

$$\frac{\partial R}{\partial \beta}(\nu^0) = \int_{-\infty}^{\infty} e^{-\beta\xi}(v^0)^2 d\xi > 0. \tag{3.15}$$

Next consider $\theta = u_-$. Since

$$\frac{\partial K}{\partial u_-} = \begin{pmatrix} 0 \\ \frac{1}{H(u)}(-s + f'(u_-)) \end{pmatrix}, \qquad K \times \frac{\partial K}{\partial u_-} = \frac{v}{H(u)}(f'(u_-) - s),$$

Eq. (3.14) takes the form:

$$\frac{\partial R}{\partial u_-}(\nu^0) = \int_{-\infty}^{\infty} e^{-\beta\xi}\frac{v^0}{H(u^0)}(f'(u_-^0) - s^0)d\xi < 0. \tag{3.16}$$

Finally, for $\theta = s$,

$$\frac{\partial K}{\partial s} = \begin{pmatrix} 0 \\ \frac{1}{H(u)}(u - u_-) \end{pmatrix}, \qquad K \times \frac{\partial K}{\partial s} = \frac{v}{H(u)}(u - u_-).$$

Thus,

$$\frac{\partial R}{\partial s}(\nu^0) = \int_{-\infty}^{\infty} e^{-\beta\xi}\frac{v^0}{H(u^0)}(u^0 - u_-^0)d\xi > 0. \tag{3.17}$$

For a fixed $\nu = (\beta, s, u_-, M)$, trajectories $\phi_\pm(\xi; \nu)$, from $\xi = \pm\infty$ respectively, are

computed until they cross the vertical line $u = u_{mid}$ at the middle equilibrium. Let $v_\pm^m(\nu)$ denote the corresponding values of v. The function $\tilde{R}(u_+) = v_-^m(\nu) - v_+^m(\nu)$, in which s varies with u_+, is used to compute values of the separation function R numerically. Specifically, $\tilde{R}(u_+) = 0$ is solved for fixed values of τ, M and u_-. Note that this is equivalent to computing zeroes of $R(\nu)$.

The first step is to choose two values of u_+ for which $\tilde{R}(u_+)$ has opposite signs; for $u_- < u_I$, this is the case for $u_+^{(1)} = u_\alpha(u_-) + \delta$ and $u_+^{(2)} = u_\gamma(u_-) - \delta$ if $u_- \in I_\alpha$ or $u_+^{(2)} = 1 - \delta$ if $u_- \notin I_\alpha$, where the small parameter $\delta > 0$ is needed to avoid degenerate equilibria. The process of interval division continues until a zero of $\tilde{R}(u_+)$ is obtained. From Eq. (3.17) and the monotonic dependence of s on u_+, the zero $u_+ = u_\Sigma(u_-, \tau)$ of $\tilde{R}(u_+)$ is unique; this will be shown in the next section.

3.3 Σ_τ Curves

The points $(u_-, u_\Sigma(u_-, \tau))$ lie on a curve Σ_τ, in the u_-, u_+ plane of Figure 3.3; Σ_τ has two connected components that terminate at points $(\underline{u}, \underline{u}_+)$, $(\bar{u}, \bar{u}_+)$ on the curve. In Figure 3.3, they are labeled only for the case $\tau = 0.1$.

As $\tau > 0$ varies, the Σ_τ curves change as suggested in Figure 3.3. The curves fill a region bounded by the Σ_∞ curve, the curve labeled A and either the u_- axis or the horizontal line $u_+ = 1$. In particular, each Σ_τ curve approaches a corner $(u_-, u_+) = (0, 1)$ or $(u_-, u_+) = (1, 0)$. As observed in [18], for quadratic relative permeabilities there can be no traveling wave connected to an equilibrium with $u_\pm = 0$ or 1. Although there is not a saddle-saddle connection from $u_- = 0$ to $u_+ = 1$, or from $u_- = 1$ to $u_+ = 0$, the limits of the Σ_τ curves can be regarded as representing these connections.

The structure seen in Figure 3.3 is established in two steps: first with $\tau = \infty$ and
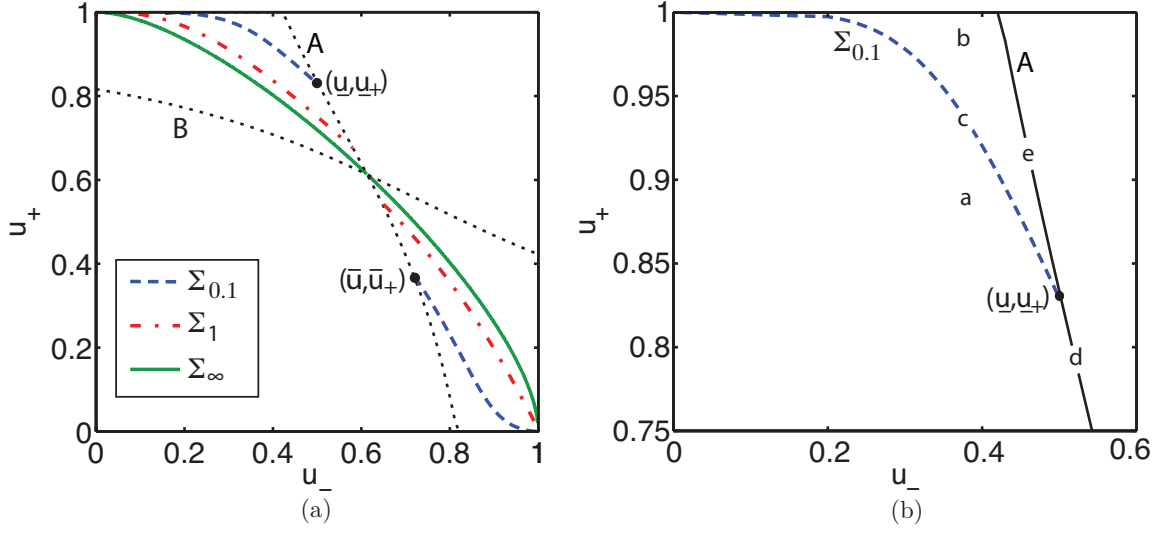
Figure 3.3: (a) Σ_τ curves for $\tau = 0.1, 1, \infty$. The Σ_τ curves are contained in the region between curves A and B. (b) Region $0 \leq u_+ \leq u_I \leq u_-$ of (a) with only curves A and $\Sigma_{0.1}$ shown. The labels a-e refer to corresponding phase portraits in Figure 3.2.

then $0 < \tau < \infty$. In both cases, an identity is used that involves integrating system (3.2) along a saddle-saddle trajectory from u_- to $u_+ = u_\Sigma(u_-)$ with speed $s = s(u_-, u_+)$ given by the Rankine-Hugoniot condition, Eq. (2.23). Along a saddle-saddle trajectory, $v = v(u)$ is a function of u. Then

$$v\frac{dv}{du} = \beta v + \frac{s(u - u_-) - f(u) + f(u_-)}{H(u)}.$$

Let

$$G(u; u_-, s) = \frac{s(u - u_-) - f(u) + f(u_-)}{H(u)}. \tag{3.18}$$

Then integrating from u_- to $u > u_-$:

$$\frac{1}{2}v^2(u) = \beta \int_{u_-}^{u} v(y)\, dy + \int_{u_-}^{u} G(y; u_-, s)\, dy. \tag{3.19}$$

35

For definiteness, suppose $u_- < u_+$. Then, letting $u = u_+$ and since $v(u) = u' \geq 0$,

$$\int_{u_-}^{u_+} G(y; u_-, s) \, dy = -\beta \int_{u_-}^{u_+} v(y) \, dy \leq 0, \qquad (3.20)$$

with equality only for $\beta = 0$. Let

$$h(u_-, u_+) = \int_{u_-}^{u_+} G(y; u_-, s) \, dy.$$

The equation $h(u_-, u_+) = 0$ gives pairs (u_-, u_+) for which there is a saddle-saddle connection from u_- to u_+ for $\beta = 0$, i.e., in the limit $\tau \to \infty$.

In what follows, it is useful to record the signs of $\dfrac{\partial s}{\partial u_-}$ and $\dfrac{\partial s}{\partial u_+}$ when $u_\pm$ correspond to saddle point equilibria.

Lemma 3.3.1. *For $u_- < u_I$ and $u_+ > u_\alpha(u_-)$, $\dfrac{\partial s}{\partial u_+} < 0$ and $\dfrac{\partial s}{\partial u_-} > 0$.*

Proof. First consider $\dfrac{\partial s}{\partial u_+}$, calculated from Eq. (2.23):

$$\frac{\partial s}{\partial u_+} = \frac{1}{u_+ - u_-}(f'(u_+) - s) < 0,$$

since $u_- < u_+$ and $f'(u_+) < s$. Similarly,

$$\frac{\partial s}{\partial u_-} = \frac{1}{u_+ - u_-}(s - f'(u_-)) > 0.$$

$\square$

The asymptotic behavior of the functions $f(u)$ and $H(u)$ will also be necessary in the proof of the following proposition; thus formulae are given in the next two lemmas.

Lemma 3.3.2. *For* $u_- < u_I$, *as* $u_- \to 0+$,

$$f(u) \sim \frac{u^2}{M} + O(u^3), \qquad H(u) \sim \frac{u^2}{M} + O(u^3).$$

Proof. The flux function $f(u)$ is expressed using the sum of a geometric series with $-1 < \frac{1}{1+\frac{u^2}{M(1-u)^2}} < 1$:

$$
\begin{aligned}
f(u) &= \frac{u^2}{M} \left(\frac{1}{1-u} \right)^2 \frac{1}{1 + \frac{u^2}{M(1-u)^2}} \\
&\sim \frac{u^2}{M} \left(1 + u + u^2 + \dots \right)^2 \left(1 - \frac{u^2}{M(1-u)^2} + \frac{u^4}{M^2(1-u)^4} - \dots \right) \\
&\sim \frac{u^2}{M} + O(u^3).
\end{aligned}
$$

Now $H(u)$ is written in terms of $f(u)$:

$$H(u) = (1-u)^2 f(u) \sim \frac{u^2}{M} + O(u^3)$$

as $u \to 0+$. $\qquad\square$

Lemma 3.3.3. *For* $u_- < u_I$, *as* $u_+ \to 1-$,

$$f(u) \sim 1 - M(1-u)^2 + O((1-u)^3), \qquad H(u) \sim (1-u)^2 + O((1-u)^4).$$

Proof. The flux function $f(u)$ is expanded about $u = 1$ and again expressed as the sum

of a geometric series, as in Lemma 3.3.2:

$$
\begin{aligned}
f(u) &= 1 - \frac{M(1-u)^2}{u^2} + \frac{M^2(1-u)^4}{u^4} - \dots \\
&= 1 + \frac{1}{(1-(1-u))^2}\left[-M(1-u)^2 + \frac{M^2(1-u)^4}{u^2} - \dots \right] \\
&= 1 + \left[1 + (1-u) + (1-u)^2 + \dots\right]^2 \left[-M(1-u)^2 + \frac{M^2(1-u)^4}{u^2} - \dots \right] \\
&\sim 1 - M(1-u)^2 + O((1-u)^3).
\end{aligned}
$$

Then

$$
\begin{aligned}
H(u) &\sim (1-u)^2 \left[1 - M(1-u)^2 + O((1-u)^3)\right] \\
&\sim (1-u)^2 + O((1-u)^4)
\end{aligned}
$$

as $u \to 1-$. $\qquad\square$

Proposition 3.3.1. *($\tau = \infty$) The level curve $\{(u_-, u_+) : h(u_-, u_+) = 0\}$ is a smooth monotonic curve $u_+ = u_\infty(u_-)$ joining $(u_-, u_+) = (0, 1)$ to $(u_-, u_+) = (1, 0)$. Moreover, $u_\infty(u_-) \sim 1 - u_-^M$ as $u_- \to 0+$ and $u_\infty(u_-) \sim (1 - u_-)^{1/M}$ as $u_- \to 1-$.*

Proof. The existence of the function $u_+ = u_\infty(u_-)$ such that $h(u_-, u_\infty(u_-)) = 0$ is established first. In the following lemma, u_- is restricted to the interval $(0, u_I)$, without loss of generality.

Lemma 3.3.4. *For every $u_- < u_I$, there exists a unique $u_+ = u_\infty(u_-) > u_I$ such that $h(u_-, u_+) = 0$. Moreover, $\lim\limits_{u_- \to u_I-} u_\infty(u_-) = u_I$ and $\lim\limits_{u_- \to 0+} u_\infty(u_-) = 1$.*

Proof. It is first shown that as $u_+ \to 1-$ with fixed $u_- < u_I$, $h(u_-, u_+) \to -\infty$. Using

Lemma 3.3.3,

$$G(u; u_-, s) = G(u; u_+, s) \;=\; \frac{s(u - u_+) - f(u) + f(u_+)}{H(u)} \tag{3.21}$$

$$= \frac{s(1 - u_+)}{(1 - u)^2} - \frac{s}{1 - u} + F_1(u, u_+, s) \tag{3.22}$$

where $F_1(u, u_+, s)$ has the property that $\int_{u_-}^{u_+} F_1(u, u_+, s)\, du$ has a finite limit as $u_+ \to 1-$.
Consequently,

$$h(u_-, u_+) = \int_{u_-}^{u_+} G(u; u_+, s)\, du \sim s \ln(1 - u_+), \quad \text{as} \quad u_+ \to 1 - . \tag{3.23}$$

On the other hand, for $u_+ = u_I$, the area between the chord joining u_- and u_+ and the curve $f(u)$ is positive (since the chord lies above the graph of f); thus $h(u_-, u_I) > 0$. Since $h(u_-, u_+)$ changes sign, there is a value of u_+ such that $h(u_-, u_+) = 0$. Uniqueness is established by the calculation

$$\frac{\partial h}{\partial u_+} = \int_{u_-}^{u_+} \frac{u - u_-}{H(u)} \frac{\partial s}{\partial u_+}\, du < 0. \tag{3.24}$$

Now consider the case near the inflection point; suppose that u_- is close to u_I. Then $G(u; u_-, s) < 0$ for $u \in (u_-, u_\gamma(u_-))$. Thus $h(u_-, u_\gamma(u_-)) < 0$. Since $h(u_-, u_I) > 0$ (as observed above), then $u_I < u_\infty(u_-) < u_\gamma(u_-)$. But $u_\gamma(u_-) \to u_I$ as $u_- \to u_I$, so that $\lim_{u_- \to u_I-} u_\infty(u_-) = u_I$.

To show $\lim_{u_- \to 0+} u_\infty(u_-) = 1$, first observe that $G(u)$, as in Eq. (3.18), can be expressed

39

asymptotically as (using Lemma 3.3.2)

$$G(u; u_-, s) \sim \frac{(u - u_-)[s - \frac{1}{M}(u + u_-) + O(u^2 + u_-^2)]}{\frac{u^2}{M} + O(u^3)}$$

$$\sim \frac{sM}{u} - \frac{sMu_-}{u^2} + O(u^2 + u_-^2)$$

as u and u_- approach zero. Thus $h(u_-, u_+)$ for fixed $u_+ < 1$ has the asymptotic form

$$\int_{u_-}^{a} G(u; u_-, s) \, du \sim -sM \ln u_- \quad \text{as} \quad u_- \to 0+ . \tag{3.25}$$

Consequently, since $h(u_-, u_\infty(u_-)) = 0$, it must be that $u_+ \to 1$ as $u_- \to 0+$ to avoid the singularity in Eq. (3.25). (This idea is pursued more quantitatively below.) This completes the proof of the lemma. $\qquad \square$

Next, it is shown that $u_\infty(u_-) \sim 1 - u_-^M$ as $u_- \to 0+$. Express $h(u_-, u_+)$ with $u_+ = u_\infty(u_-)$ as a sum of three integrals:

$$h(u_-, u_+) = \int_{u_-}^{a} G(u; u_-, s) \, du + \int_{a}^{b} G(u; u_-, s) \, du + \int_{b}^{u_+} G(u; u_-, s) \, du = 0, \tag{3.26}$$

where a and b are chosen such that $\int_{a}^{b} G(u; u_-, s) \, du = 0$. Then the first and third terms in Eq. (3.26) must balance each other as $u_- \to 0+$ and $u_+ \to 1-$. As in Eq. (3.23) and Eq. (3.25), respectively,

$$\int_{b}^{u_+} G(u; u_-, s) \, du \sim s \ln(1 - u_+) \quad \text{as} \quad u_+ \to 1- \tag{3.27}$$

$$\int_{u_-}^{a} G(u; u_-, s) \, du \sim -sM \ln u_- \quad \text{as} \quad u_- \to 0+ .$$

The terms from these two integrals must add to zero which gives $u_+ = u_\infty(u_-) \sim 1 - u_-^M$

40

as $u_- \to 0+$.

To show monotonicity of $u_\infty(u_-)$, the identity $h(u_-, u_\infty(u_-)) = 0$ is differentiated with respect to u_-:

$$\frac{\partial h}{\partial u_-} + \frac{\partial h}{\partial u_+} u'_\infty(u_-) = 0.$$

From Eq. (3.24), $\dfrac{\partial h}{\partial u_+} < 0$ and $\dfrac{\partial h}{\partial u_-}$ is calculated using Eq. (3.21) and Lemma 3.3.1 with $s = s(u_-, u_+)$:

$$\frac{\partial h}{\partial u_-} = \int_{u_-}^{u_+} \frac{u - u_+}{H(u)} \frac{\partial s}{\partial u_-} du < 0.$$

Therefore, $u'_\infty(u_-) < 0$. Defining $u_\infty(0) = 1$ and $u_\infty(u_I) = u_I$, the smooth curve

$$\Sigma_\infty = \{(u_-, u_\infty(u_-)) : 0 \le u_- \le u_I\}$$

decreases monotonically from $(0, 1)$ to (u_I, u_I).

A similar argument for $u_- > u_I$ shows that Σ_∞ extends monotonically from (u_I, u_I) to $(1, 0)$ with $u_\infty(u_-) \sim (1 - u_-)^{1/M}$ as $u_- \to 1-$. This completes the proof of Proposition 3.3.1. $\qquad\square$

In defining the separation function R, it is natural to have it depend on parameters u_-, s, β. However, in the following proposition, properties of the Σ_τ curves are established in the (u_-, u_+) plane. It is thus convenient to express zeroes of R in terms of parameters $u_\pm, \tau$; let

$$\hat{R}(u_-, u_+, \tau) = R(u_-, s(u_-, u_+), \beta), \quad \text{in which} \quad \beta = 1/\sqrt{s(u_-, u_+)\tau}.$$

Note that $\hat{R}$ is not the same as the function $\tilde{R}(u_+)$ used to calculate zeroes of R. The

41

proof of the next proposition uses the inequality

$$\frac{\partial \hat{R}}{\partial u_+}(u_-, u_\Sigma(u_-, \tau), \tau) < 0, \qquad u_- \neq u_I. \tag{3.28}$$

That is, $\hat{R}$ is strictly decreasing in u_+ at the zero $u_+ = u_\Sigma(u_-, \tau)$ of $\hat{R}$. Numerical results show clearly that $\hat{R}(u_-, u_+, \tau)$ is strictly decreasing as a function of u_+, but proving this property is problematic for extreme values of the parameters (specifically large values of τ). Consequently, Eq. (3.28) is an assumption in the proposition.

Proposition 3.3.2. $(0 < \tau < \infty)$ *For each $\tau > 0$, there is $\underline{u} = \underline{u}(\tau)$ with the property that, for each $u_- \in (0, \underline{u})$, the equation $\hat{R}(u_-, u_+, \tau) = 0$ has a solution $u_+ = u_\Sigma(u_-, \tau)$. Moreover, assuming Eq. (3.28),*

1. $u_+ = u_\Sigma(u_-, \tau)$ is unique and $u_\Sigma(u_-, \tau)$ is a C^∞ function;

2. $\dfrac{\partial u_\Sigma}{\partial \tau} < 0$ and $\dfrac{\partial u_\Sigma}{\partial u_-} < 0$.

Remark: In this proposition, $\tau > 0$ is fixed and pairs (u_-, u_+) are identified for which there is a traveling wave from u_- to u_+. This is a slightly different approach from that in [62], where for each fixed pair (u_-, u_+) with $u_- < u_+, h(u_-, u_+) < 0$, and $u_+ > u_\alpha(u_-)$, the existence of a traveling wave from u_- to u_+ is established for some (unique) value of τ.

Proof. Let $u_- < u_I$. From Proposition 3.3.1, let $u_+^0 > u_-^0$ satisfy $h(u_-^0, u_+^0) = 0$. Then $\int_{u_-^0}^{u_+^0} G(y; u_-^0, s^0)\, dy = 0$ and $\int_{u_-^0}^{u} G(y; u_-^0, s^0)\, dy > 0$ for $u_-^0 < u < u_+^0$. The point $(u_+^0, 0)$ is an equilibrium with $s^0 = s(u_-^0, u_+^0)$. Then from Eq. (3.19), with $u_- = u_-^0$, $v(u) > 0$ for $u_-^0 < u < u_+^0$. Consequently, note that $\hat{R}(u_-^0, u_+^0, \tau^0) > 0$ by comparing the unstable manifold from $(u_-^0, 0)$ to the stable manifold entering $(u_+^0, 0)$. This corresponds to the phase portrait shown in Figure 3.2a.

42

Let u_* be defined by Eq. (3.7) when $u_\gamma(u_*) = 1$. It is argued next that $\hat{R}(u^0_-, u_+, \tau^0) < 0$ for $u^0_- < u_*$ and u_+ near 1. Suppose for a contradiction that $v(u) > 0$ for $u \in (u^0_-, u_+]$ and so $\hat{R}(u^0_-, u_+, \tau^0) > 0$. From Eq. (3.27),

$$\int_{u^0_-}^{u_+} G(u; u^0_-, s(u^0_-, u_+)) \, du \to -\infty, \quad \text{as} \quad u_+ \to 1^-.$$

However, $\int_{u_-}^{u} v(u) \, du$ is uniformly bounded. Thus the right hand side of Eq. (3.19) is negative for u_+ close enough to 1 while the left hand side of Eq. (3.19) is positive for all u. This contradiction implies $v(u) = 0$ for some $u < u_+$, as in Figure 3.2b.

For (u_-, u_+) on the curve A, $(u_-, 0)$ is a saddle-node equilibrium. In fact, the equilibrium has a positive eigenvalue $\lambda_+ = \beta$ and a well defined eigenvector with corresponding unstable manifold. For this reason, as in [53], the separation function $\hat{R}(u_-, u_+, \tau)$ is well defined on A and continuous on $U \cup A \cup \Sigma_\infty$, where U is the open region bounded by A, Σ_∞ and the line $u_+ = 1$.

For (u_-, u_+) on A near $(u_*, 1)$, $\hat{R} < 0$ since $\int_{u_-}^{u_+} G(u; u_-, s) \, du \to -\infty$ as $u_+ \to 1$. Also observe that $\hat{R}(u_-, u_+, \tau) \to 0$ as $(u_-, u_+) \to (u_I, u_I)$. Setting $\hat{R}(u_I, u_I, \tau) = 0$, let $\underline{u} = min\{u_- : \hat{R}(u_-, u_\gamma(u_-), \tau) = 0, u_* < u_- \le u_I\}$. Consequently, $\hat{R}(u_-, u_\gamma(u_-), \tau) < 0$ for $u_* < u_- < \underline{u}$.

For each u_-, $0 < u_- < \underline{u}$, values of u_+ at which $\hat{R}$ has opposite signs have been identified. Thus, by continuity, there exists a value of $u_+ = u_\Sigma(u_-, \tau)$ for which $\hat{R} = 0$. With existence established, note that uniqueness follows directly from assuming Eq. (3.28).

It follows from Eq. (3.28) and the Implicit Function Theorem that u_Σ is a C^∞ function. Differentiating $\hat{R}(u_-, u_\Sigma(u_-, \tau), \tau) = 0$ with respect to τ gives

$$\frac{\partial \hat{R}}{\partial u_+} \frac{\partial u_\Sigma}{\partial \tau} + \frac{\partial \hat{R}}{\partial \tau} = 0. \tag{3.29}$$

43

But $\dfrac{\partial \hat{R}}{\partial \tau} = \dfrac{\partial R}{\partial \beta}\dfrac{\partial \beta}{\partial \tau} < 0$ from Eq. (3.15) and $\beta = 1/\sqrt{s\tau}$. It now follows from Eq. (3.28) and Eq. (3.29) that $\dfrac{\partial u_\Sigma}{\partial \tau} < 0$.

Similarly differentiating $\hat{R}(u_-, u_\Sigma, \tau) = 0$ with respect to u_- gives

$$\frac{\partial \hat{R}}{\partial u_-} + \frac{\partial \hat{R}}{\partial u_+}\frac{\partial u_\Sigma}{\partial u_-} = 0. \tag{3.30}$$

But

$$
\begin{aligned}
\frac{\partial \hat{R}}{\partial u_-} &= \frac{\partial R}{\partial u_-} + \frac{\partial R}{\partial s}\frac{\partial s}{\partial u_-} + \frac{\partial R}{\partial \beta}\frac{\partial \beta}{\partial s}\frac{\partial s}{\partial u_-} \\
&< \int_{-\infty}^{\infty} e^{-\beta\xi}\frac{v^0}{H(u^0)}\frac{f'(u_-) - s}{u_+ - u_-}(u_+ - u)d\xi < 0,
\end{aligned}
$$

where Eq. (3.16) and Eq. (3.17) have been combined and Eq. (3.15) has been used together with Lemma 3.3.1. Now it follows from Eq. (3.28) and Eq. (3.30) that $\dfrac{\partial u_\Sigma}{\partial u_-} < 0$. This completes the proof of Proposition 3.3.2. $\qquad\square$

3.4 The Riemann Problem

In this section, solutions of the Riemann problem

$$u_t + f(u)_x = 0 \tag{3.31a}$$

$$u(x,0) = \begin{cases} u_l & \text{if } x < 0 \\ u_r & \text{if } x > 0 \end{cases} \tag{3.31b}$$

are presented.

Solutions of Eq. (3.31) are leading order approximations to solutions of Eq. (3.1) with

jump initial data. The discontinuity is propagated as combinations of shock and rarefaction waves, suggesting the decomposition of solutions of general initial value problems for Eq. (3.1) into combinations of traveling waves approximating shocks and smooth waves approximating rarefaction waves. The solution of Eq. (3.31) relies crucially on the description of undercompressive shocks, since these represent the boundary between admissible and inadmissible Lax shocks.

In Figure 3.4, the solution of the Riemann problem is presented for all data given by Eq. (3.31b). The structure of the solution is independent of $\tau > 0$, so for definiteness the solution is shown schematically for $\tau = 1$. In Figure 3.4a, open regions are labeled according to the combination of shock and rarefaction waves appearing in the solution: classical rarefaction and shock waves are denoted by R and S, respectively, while nonclassical undercompressive shocks are denoted by Σ. The horizontal dashed line is located at $u_r = u_I$, the inflection point of $f(u)$. The horizontal lines at $u_r = \underline{u}_+$ and $u_r = \bar{u}_+$ form the boundaries between the regions labeled RS and $R\Sigma$. The curve separating regions $R\Sigma$ and $S\Sigma$ is the set of points (u_ℓ, u_r) for which there is an undercompressive shock from u_ℓ to u_r (as in Figure 3.3a). The curves separating the S and $S\Sigma$ regions represent the middle equilibria of undercompressive shocks: they consist of pairs (u_{mid}, u_r), for which $u_{mid} = u_{mid}(u_-)$ is the middle equilibrium for some u_- and $u_r = u_\Sigma(u_-)$ is the right state of an undercompressive shock. Notice that these curves intersect the axes $u_r = 0, 1$ in Figure 3.4 at the same value of $u_{mid} = 2/3$ for $M = 2$. Since they are monotonic, it is convenient to parameterize these curves by u_r. Accordingly, let $u_o(u_r) = u_{mid}^{-1}(u_r), u_\sigma(u_r) = u_\Sigma^{-1}(u_r)$. The short curve through the point (u_I, u_I) consists of the points $(u_\alpha(u_r), u_r)$. It is part of the curve labeled 'A' in Figure 3.1b.

Solutions of the Riemann problem are described by fixing $u_r < u_I$ in two cases (the construction for $u_r > u_I$ is similar) and varying u_ℓ. This approach is simpler than fixing
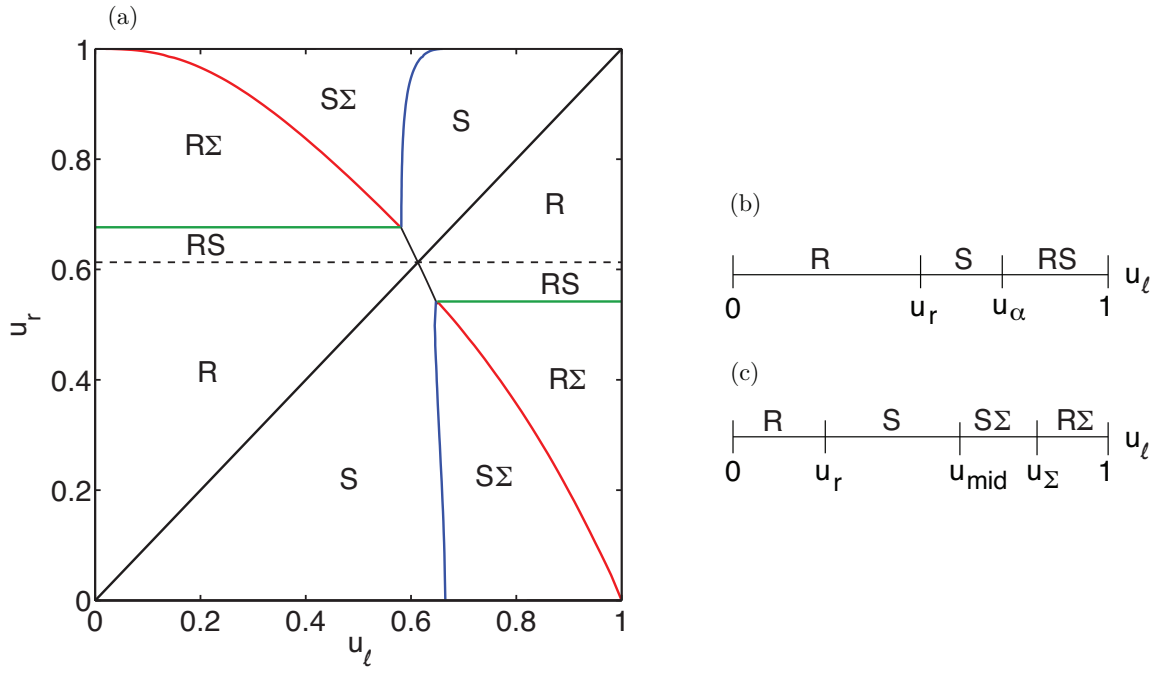
Figure 3.4: Solution of the Riemann problem for $\tau = 1, M = 2$: (a) solutions for all values of u_ℓ, u_r, (b) classical solutions as u_ℓ varies and u_r is fixed, (c) classical and nonclassical solutions as u_ℓ varies and u_r is fixed

u_ℓ, as in [33], which involves many more cases and is more complicated because of the shape of the curves separating regions S and $S\Sigma$.

- For $\bar{u}_+ < u_r < u_I$ (Figure 3.4b), the Riemann problem has only classical solutions as u_ℓ varies between 0 and 1. When $u_\ell < u_r$, a rarefaction wave joins the two states as, in this region, characteristic speeds are increasing from u_ℓ to u_r. An admissible Lax shock from u_ℓ to u_r exists when $u_\ell \in (u_r, u_\alpha(u_r))$. For $u_\alpha(u_r) < u_\ell < 1$, the solution is a rarefaction-shock, a combination of a rarefaction wave from u_ℓ to $u_\alpha(u_r)$ and an admissible Lax shock between $u_\alpha(u_r)$ and u_r with speed $f'(u_\alpha(u_r))$.

- For $0 < u_r < \underline{u}_+$ (Figure 3.4c), solutions are either classical or a combination of classical and nonclassical waves, depending on the value of u_ℓ. As in the previous case, a rarefaction wave joins u_ℓ to u_r when $u_\ell < u_r$. Recall that $u_o = u_o(u_r), u_\sigma = u_\sigma(u_r)$ are the middle and top equilibria for the undercompressive shock from u_σ to u_r. The graphs of these functions form the boundaries between the regions $S, S\Sigma, R\Sigma$. For $u_\ell \in (u_r, u_o)$, the solution to Eq. (3.31) is an admissible Lax shock. Once $u_\ell > u_o$, an admissible Lax shock connects u_ℓ to u_σ and then an admissible undercompressive shock joins u_σ and u_r. This structure persists as long as $u_\ell < u_\sigma$. Finally, for $u_\sigma < u_\ell < 1$, the solution is a combination of a rarefaction wave from u_ℓ to u_σ and an admissible undercompressive shock from u_σ to u_r.

It is worth pointing out that by construction, even though double shock solutions $S\Sigma$ of the Riemann problem are not monotonic, the values of u remain in the physically valid interval $0 \leq u \leq 1$. As seen in the construction of traveling waves for undercompressive shocks, this is a consequence of the degeneracy of $H(u)$ at $u = 0, 1$. Positive invariance of the unit interval has been proven in [48] for the fully nonlinear equation with regularization; however, it is unknown how this result exactly relates to the observed behavior

of the double shock solutions for the conservation law.

As $\tau \to 0$, note that $\beta = 1/\sqrt{s\tau} \to \infty$ since $1 \leq s \leq f'(u_I)$. To understand this limit, let $\xi = \beta\zeta$ so that Eq. (2.24) becomes

$$\frac{1}{\beta^2}u'' = u' + \frac{1}{H(u)}\left[s(u - u_-) - f(u) + f(u_-)\right],$$

in which $' = d/d\zeta$. In the limit $\beta \to \infty$, this ODE reduces to

$$u' = -\frac{1}{H(u)}\left[s(u - u_-) - f(u) + f(u_-)\right].$$

Consequently, the traveling waves connect only adjacent equilibria u_-, u_+ satisfying the Rankine-Hugoniot condition (Eq. (2.23)), corresponding to Lax shocks. The solution of the Riemann problem is therefore entirely classical. This is manifested in Figure 3.4a by the Σ_τ curves (separating regions $R\Sigma$ and $S\Sigma$ in the figure) approaching the horizontal lines $u_+ = 0$ and $u_+ = 1$, thereby collapsing the regions indicating undercompressive shocks.

For fluxes with different dependence of relative permeability on saturation, the Σ_τ curves of traveling wave pairs (u_-, u_+) can fail to include the corners $(0, 1), (1, 0)$ of the saturation domain [62]. In this case, non-smooth traveling waves emerge that have corners at $u = 0$ or at $u = 1$, and connect to a value of u in the open interval $0 < u < 1$; this issue is addressed in detail in the next chapter.

3.5 PDE Simulations

To verify the solution structures obtained in the previous section, numerically simulated solutions of Eq. (2.18) with jump initial data (3.31b) are included here. The parameter τ

is taken to be one for simplicity while M is taken to be two, following [63]. Computations are performed on the interval $-2 \leq x \leq 4$, with $\Delta x = h = 0.002$ for the rarefaction and rarefaction-undercompressive shock solutions and $h = 0.005$ in other cases. All solutions are shown at time $t = 1$, with $\Delta t = k = 0.1\,(\Delta x)^2$. The pairs (u_ℓ, u_r) are chosen in each case by consulting Fig. 3.4a; for example, the pair $(u_\ell, u_r) = (0.8, 0.2)$ is chosen to generate the shock-undercompressive shock solution so that the size of the jumps and separation between shocks are clear in the plots.

(a)   (b)
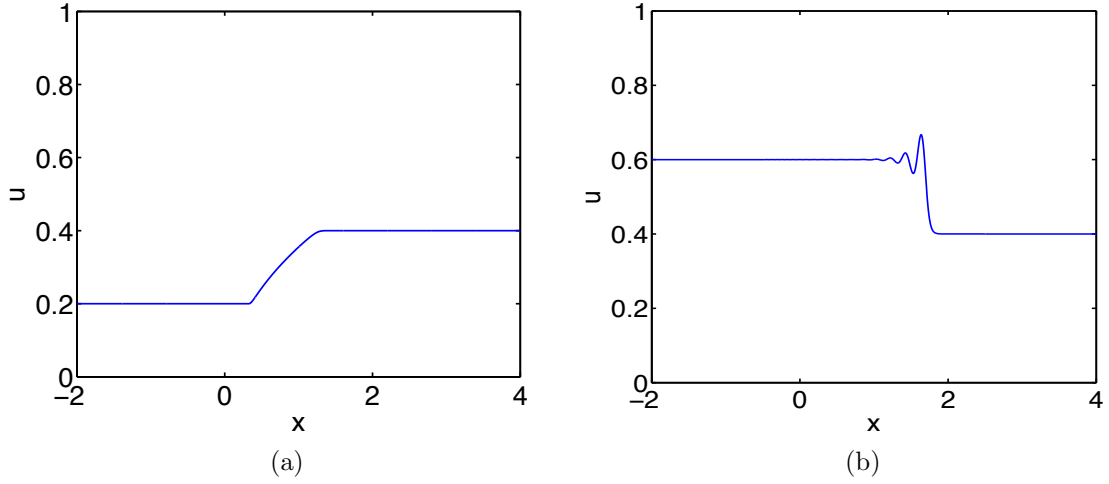
Figure 3.5: (a) Rarefaction wave solution for $u_\ell = 0.2, u_r = 0.4, \epsilon = 0.01, \tau = 1, M = 2$.
(b) Admissible Lax shock for $u_\ell = 0.6, u_r = 0.4, \epsilon = 0.05, \tau = 1, M = 2$.

By scaling x and t by a small parameter ϵ, the effects of the regularization terms are controlled in Eq. (2.18). Specifically, let $u(x, t) = \hat{u}(\psi)$ with $\psi = \dfrac{x - st}{\epsilon}$. Traveling waves then have width on the order of ϵ. With this scaling, Eq. (2.18) becomes

$$\frac{\partial u}{\partial t} + \frac{\partial f(u)}{\partial x} = \frac{\partial}{\partial x}\left[H(u)\left(\epsilon \frac{\partial u}{\partial x} + \epsilon^2 \tau \frac{\partial^2 u}{\partial x \partial t}\right)\right].$$
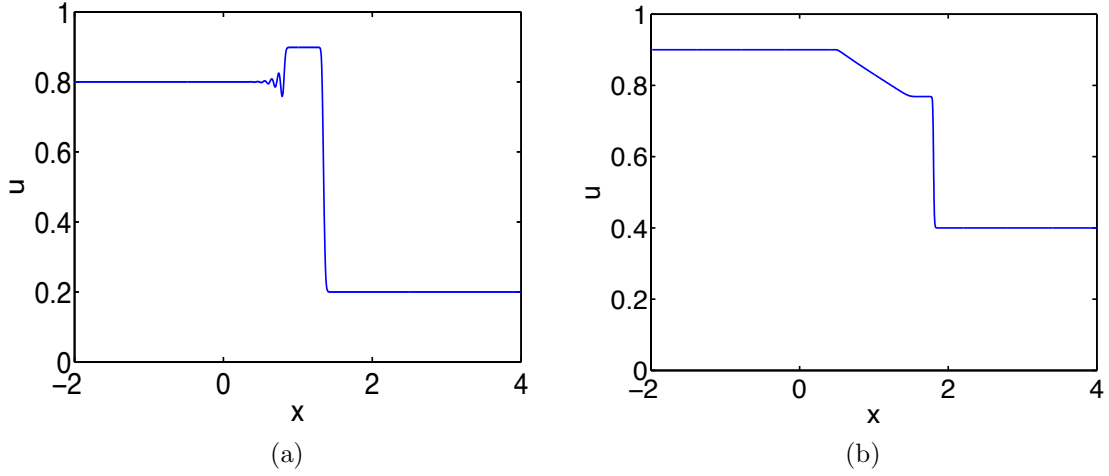
Figure 3.6: (a) Admissible Lax shock trailing the undercompressive shock for $u_\ell = 0.8, u_r = 0.2, \epsilon = 0.05, \tau = 1, M = 2$. (b) Rarefaction wave trailing the undercompressive shock for $u_\ell = 0.9, u_r = 0.4, \epsilon = 0.01, \tau = 1, M = 2$.

The corresponding finite difference scheme is:

$$\frac{u_j^n - u_j^{n-1}}{k} + \frac{g_{j+1/2} - g_{j-1/2}}{h} =$$

$$\frac{\epsilon}{h^2} \left[H\left(\bar{u}_{j+\frac{1}{2}}^n\right)(u_{j+1}^n - u_j^n) - H\left(\bar{u}_{j-\frac{1}{2}}^n\right)(u_j^n - u_{j-1}^n) \right] +$$

$$+\frac{\epsilon^2 \tau}{h^2 k} \left[H\left(\bar{u}_{j+\frac{1}{2}}^n\right)(u_{j+1}^n - u_j^n - u_{j+1}^{n-1} + u_j^{n-1}) - H\left(\bar{u}_{j-\frac{1}{2}}^n\right)(u_j^n - u_{j-1}^n - u_j^{n-1} + u_{j-1}^{n-1}) \right]$$

$$(3.32)$$

where $\bar{u}_{j+\frac{1}{2}} = \frac{1}{2}(u_j + u_{j+1})$, and $g_{j+1/2} = \frac{1}{12}(-f(u_{j+2}) + 7f(u_{j+1}) + 7f(u_j) - f(u_{j-1}))$ is

a high order approximation of the flux function, $f(u)$ [33]. Specifically, it has truncation

error that is $O(h^3)$ and so is higher order than the truncation error from the right hand

side of Eq. (3.32), which is $O(\epsilon h^2)$, provided $h \ll \epsilon$. Even though $H(u)$ is nonlinear, the

modified equation has the same form as in [33]:

$$u_t + f(u)_x = \epsilon(H(u)u_x)_x + \epsilon^2 \tau(H(u)u_{xt})_x + O(h^3) + O(\epsilon h^2).$$

The initial condition (3.31b) is smoothed slightly to avoid spurious small oscillations:

$$u_j(0) = -\tanh(\delta x_j)\frac{u_\ell - u_r}{2} + \frac{u_\ell + u_r}{2},$$

with $\delta = 250$ in these simulations. It is worth noting that discontinuities in initial data are likely to persist and decay, as shown in [16] for a related equation.

In Figure 3.5a, a smooth rarefaction wave connects $u_\ell = 0.2$ to $u_r = 0.4$. The classical Lax shock from $u_\ell = 0.6$ to $u_r = 0.4$ is shown in Figure 3.5b. In Figure 3.6a, there is a Lax shock from $u_\ell = 0.8$ to the plateau value of u_σ, and a faster undercompressive shock from u_σ to $u_r = 0.2$. Both shock solutions have exponentially decaying oscillations behind the Lax shock due to the complex eigenvalues at u_ℓ. The oscillation wavelengths can be computed from the coefficients of the eigenvalues' imaginary parts. In the case of Figure 3.5b, Eq. (3.3) with $u = u_\ell = 0.6, u_r = 0.4$ and $\epsilon = 0.05$ gives $\text{Im}(\lambda_\pm) = 1.598$. Then the wavelength of the oscillation is calculated to be $\frac{2\pi}{\frac{1.598}{0.05}} = 0.196$. This value compares well with the observed distance between successive maxima, approximately 0.2. For the two simulations involving shocks only, $\epsilon = 0.05$ in order to show the oscillations clearly. When the simulations are done with $\epsilon = 0.01$, the predicted oscillations are too compressed to be seen clearly. Finally, Figure 3.6b illustrates the rarefaction-undercompressive shock solution. The rarefaction wave connects $u_\ell = 0.9$ to u_σ and the undercompressive shock takes u_σ to $u_r = 0.4$.

The numerical simulation of solutions of these equations is notoriously difficult; thus attention has been restricted here to a specific numerical scheme that is consistent and stable for the carefully chosen parameters and data selected. Issues surrounding the use of numerical schemes to compute undercompressive shocks and their traveling waves are discussed in [32]. In particular, Hayes and LeFloch provide conditions under which an

undercompressive shock is generated numerically. They also compute kinetic functions for various schemes and compare them to continuous traveling wave solutions.

Chapter 4

The Modified Buckley-Leverett Equation with Fractional Relative Permeabilities

The relative permeability functions in this chapter are generalized from the previous chapter; now let $k^w(u) = \kappa^w u^p$, $k^n(u) = (1-u)^q$ where p, q are allowed to vary. Particular attention is given to values of p and q between one and two. Unlike in the previous chapter, it is assumed throughout this chapter that $0 \leq u_+ < u_-$. Phase portraits are used to understand the appearance of so-called "sharp" traveling waves [62] in this new context. These waves offer a new solution structure for the Riemann problem which is verified with numerical simulations.

4.1 Previous Results

In [18, 62], the authors provide an integrability condition for the existence of traveling waves of system (3.2) between a nonzero upstream saturation u_- and zero downstream saturation u_+, provided that the exponent of the wetting phase relative permeability function is strictly between one and two. Namely, the integrability of the function $G(u)$ defined in Eq. (3.18) is a necessary condition for the existence of traveling waves between $u_- \in (0, 1)$ and $u_+ = 0$. This is in contrast to the results from chapter three in which there are no connections to $u_\pm = 0$ except in the limiting cases discussed in the context of Eq. (3.26) and seen in Figure 3.3 as the Σ_τ curves approach the corners $(u_-, u_+) = (0, 1), (1, 0)$. The integrability result from [18, 62] is reproduced here for thoroughness, with the notation previously introduced. It is noteworthy that the exponents need not be equal; the following non-existence result is generalized for variable exponents in the open interval $(1, 2)$. If either exponent is less than or equal to one, the flux function loses its characteristic S shape. On the other hand, if either exponent is greater than or equal to two, $G(u)$ is no longer integrable for $u_+ = 0$.

Proposition 4.1.1. [18, 62] *Let $0 \le u_+ < u_-$ with u_- fixed. Consider Eq. (2.22) with boundary conditions given in Eq. (2.21).*

1. *If a traveling wave solution exists, then*

$$0 \le \int_{u_+}^{u_-} G(y; u_+, s)dy < \infty \qquad (4.1)$$

   where $G(u; u_+, s)$ is given by Eq. (3.18).

2. *If $p \ge 2$, then there is no solution with $u_+ = 0$ and $0 < u_- \le 1$.*

Proof. Suppose there exists a traveling wave from u_+ to u_-. Then $v = u'$ can be expressed as a function of u and is negative. Recall Eq. (3.20):

$$\int_{u_-}^{u_+} G(y; u_-, s) dy = -\beta \int_{u_-}^{u_+} v(y) dy \leq 0. \tag{4.2}$$

Reversing $u_\pm$ gives

$$\int_{u_+}^{u_-} G(y; u_+, s) dy \geq 0$$

since $\beta = \frac{1}{\sqrt{s\tau}} \geq 0$. Further, $v(u)$ is continuous on the compact interval $[u_+, u_-]$. Thus $v(u)$ is bounded. Then

$$\int_{u_-}^{u_+} G(y; u_-, s) dy = -\beta \int_{u_-}^{u_+} v(y) dy < \infty.$$

Combining this with Eq. (4.2) yields

$$0 \leq \int_{u_+}^{u_-} G(y; u_+, s) dy < \infty.$$

To prove the second part of the proposition, recall the asymptotic expansions given in Lemmas 3.3.2, 3.3.3. For general p, q,

$$f(u) \sim \frac{u^p}{M}, \quad H(u) \sim \frac{u^p}{M}, \quad G(u) \sim sMu^{1-p} \tag{4.3}$$

as $u \to 0+$ and

$$f(u) \sim 1 - M(1-u)^q, \quad H(u) \sim (1-u)^q, \quad G(u) \sim -s(1-u)^{1-q} \tag{4.4}$$

as $u \to 1-$. Then, using Eq. (4.3),

$$\int_{u_+}^{u_-} G(y; u_+, s)dy \sim \int_{u_+}^{u_-} sMy^{1-p}dy \to \infty$$

as $u_+ \to 0+$ since $p \geq 2$. Thus, using the first part of the proposition, no traveling wave solutions exist with $u_+ = 0$. $\square$

In this chapter, for simplicity, the representative exponent value of $p = q = \frac{3}{2}$ is used for the relative permeability of both wetting and non-wetting phases. Then the conditions of Proposition 4.1.1 are satisfied with

$$f(u) = \frac{u^{3/2}}{u^{3/2} + M(1-u)^{3/2}}, \qquad H(u) = \frac{\kappa^n u^{3/2}(1-u)^{3/2}}{u^{3/2} + M(1-u)^{3/2}} \tag{4.5}$$

in Eq. (3.1). In comparison to Figure 2.3, the fractional exponents elongate the convex portion of the flux curve by increasing the location of the inflection point to $u_I \approx 0.6926$ when $M = 2$. The capillary induced diffusion coefficient curve has a larger maximum value than in Figure 2.3 for $M = 2$ but is still weighted to the right. See Figure 4.1.

Still in the larger context of fractional exponents, van Duijn *et al.* [62] consider sharp traveling waves which satisfy system (3.2) with $u_- = 1, u_+ > 0$ but have a discontinuity in u' at the transition from $u = 1$ to $u < 1$. Specifically, the traveling wave has a corner there. Proposition 4.1.1 is satisfied with the single degenerate value, albeit at $u_- = 1$ instead of $u_+ = 0$. The authors provide a result for the existence of such sharp fronts as well as numerical simulations but offer nothing pertaining to their role in solutions of the Riemann problem. In the work presented in this chapter, phase portraits are used to understand the mechanism underlying the sharp profiles. Further, a new type of solution of the Riemann problem is described for an upstream saturation of one and a downstream
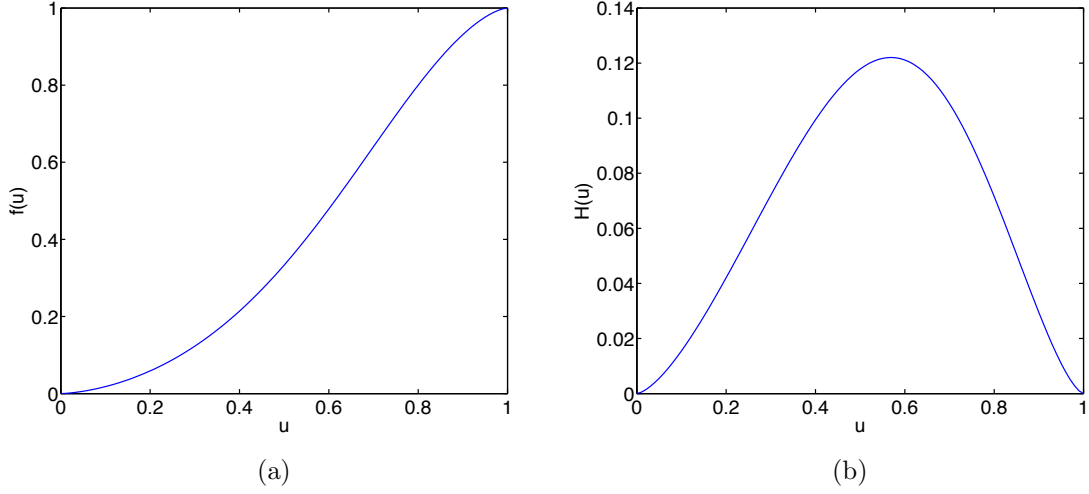
Figure 4.1: (a) Flux $f(u)$ (b) Capillary induced diffusion coefficient $H(u)$ given by Eq. (4.5) with $M = 2$

saturation near zero.

4.2 Phase Portraits

In this integrable regime, the phase portraits in Figure 3.1 are still applicable. However, there is an additional phase portrait, seen in Figure 4.2, that accounts for the sharp traveling wave between $u_- = 1$ and u_+ near zero. In the figure, $(u_-, u_+) = (1, 0.025)$, $M = 2$ and $\tau = 10$. The bottom equilibrium, $u_{bot} = u_+$ is a saddle while the middle equilibrium, u_{mid}, is an unstable spiral. Using Eq. (3.3), the top equilibrium $u_{top} = u_- = 1$ has eigenvalues $\pm\infty$ with eigenvectors $(\pm 1 \ 0)$, respectively. This is visualized in Figure 4.2 as the stable and unstable manifolds are vertical at $u = 1$. Also notice that the stable and unstable manifolds of $u_+ = 0.025$ intersect the line $u = 1$ in finite time. It is specifically the stable manifold from $u_- = 1$ to $u_+ = 0.025$ that corresponds to the

sharp traveling wave previously discussed. The corner of the traveling wave is a result of the jump discontinuity in $v = u'$ at $u = 1$, as is seen in Figure 4.2.
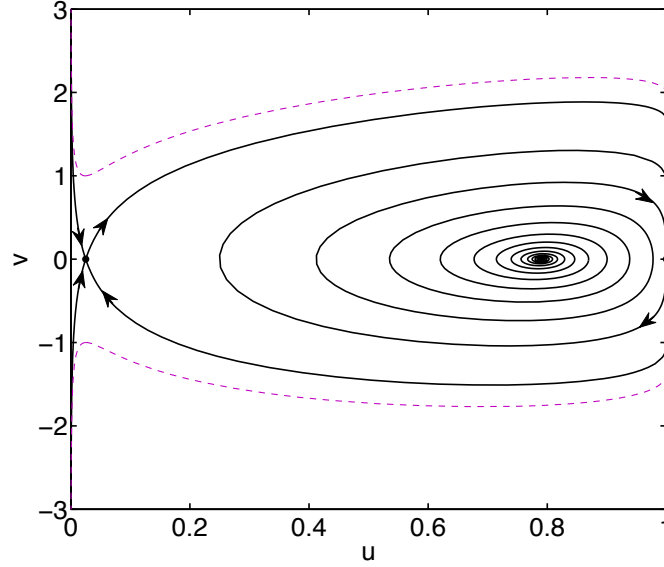
Figure 4.2: Phase portrait of system (3.2) with $f(u)$ and $H(u)$ given by Eq. (4.5), $M = 2$ and $\tau = 10$

4.3 Σ_τ Curves

The Σ_τ curves in Figure 4.3 now intersect the lines $u_- = 1$ and $u_+ = 1$ for nonzero u_+ and u_-, respectively. In the previous chapter, the non-integrability of $G(u; u_+, s)$ with quadratic relative permeabilities prevented this scenario. Recall that the Σ_τ curves in Figure 3.3 approach the corners $(0, 1)$ and $(1, 0)$ only in the limit through a balance of leading order terms for u_- near 0 and u_+ near 1 (see Proposition 3.3.1). The same asymptotic analysis is not necessary in the case of fractional exponents. Traveling waves

exist between pairs $u_- = 1, u_+ > 0$ and $u_- > 0, u_+ = 1$ for $\tau > 0$ and Eq. (4.1) is satisfied.
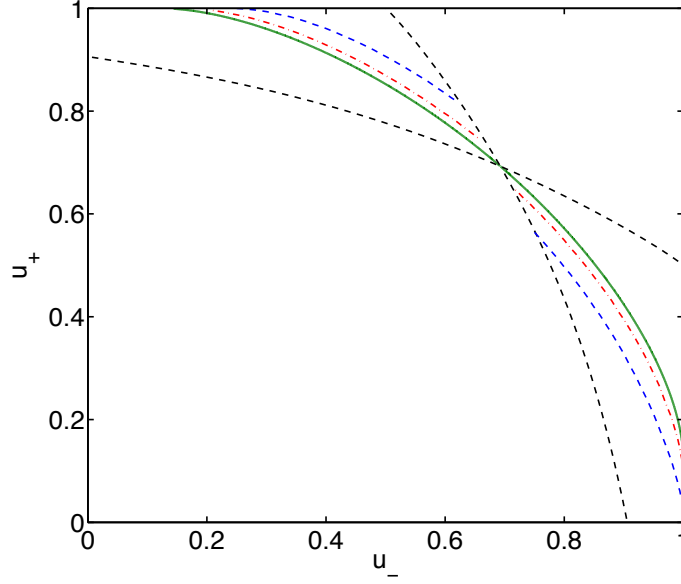
Figure 4.3: Σ_τ curves for $p = q = \frac{3}{2}$, $M = 2$, $\tau = 1$ (blue dashed), $\tau = 10$ (red dot-dashed), $\tau = \infty$ (green solid)

While the constitutive equations differ between this context and the former in chapters two and three, the separation function, $R(\nu)$, described in Section 3.2 remains applicable here with $\nu = (\beta, s, u_-, M)$ and the assumption that $u_- < u_+$. In fact, the results obtained in that section regarding the derivatives of R, specifically Eqs. (3.15), (3.16), (3.17), remain unchanged as they do not depend on the exponents of the relative permeability functions. Note that the inequality $f'(u_-^0) < s^0$ used in Eq. (3.16) still holds because the fractional exponents in the relative permeability functions are greater than one; thus the flux function $f(u)$ retains its convex-concave shape, ensuring that, for sat-

urations in the region for which saddle-saddle connections exist, the slope of the chord connecting $u_\pm$ is larger than the slope of the tangent at either value.

Figure 4.4 shows Σ_τ curves in cases for which $p \neq q$: $p = \frac{3}{2}, q = 2$ in Figure 4.4a while $p = 2, q = \frac{3}{2}$ in Figure 4.4b. These specific values are chosen with an aim of better understanding the condition on p given in Proposition 4.1.1, for which a quadratic exponent is a boundary between existence and non-existence of traveling wave solutions. Observe that the curves in Figure 4.4a intersect the lines $u_\pm = 0$ for $u_\mp \neq 1$ even though $q = 2$. Likewise, the Σ_τ curves in Figure 4.4b intersect the lines $u_\pm = 1$ for $u_\mp \neq 0$.
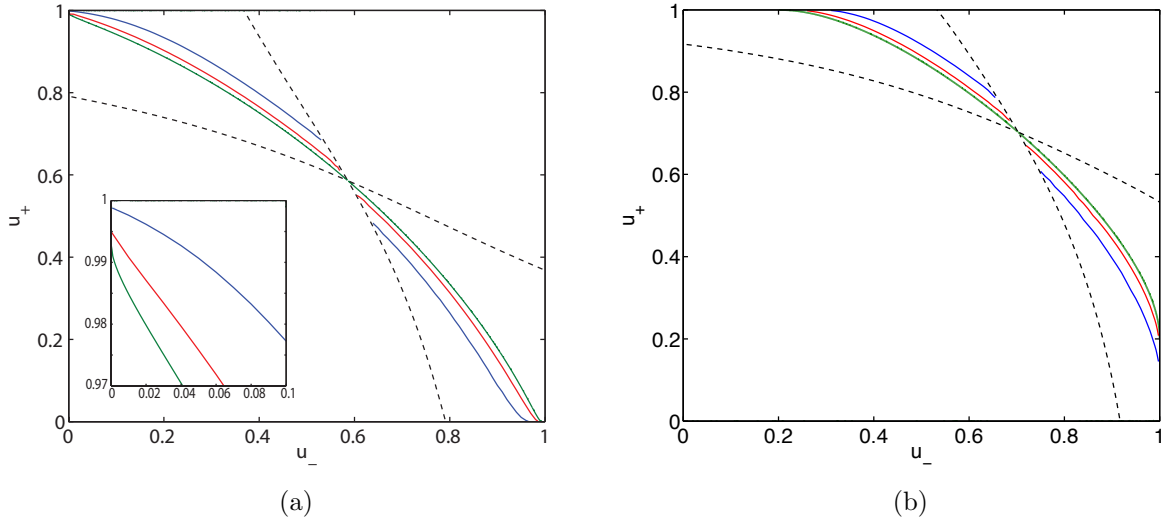
Figure 4.4: Σ_τ curves when $M = 2$, $\tau = 1$ (blue), $\tau = 10$ (red), $\tau = \infty$ (green) and (a) $p = \frac{3}{2}, q = 2$, inset shows behavior of Σ_τ curves near corner $(u_-, u_+) = (0, 1)$ (b) $p = 2, q = \frac{3}{2}$

The behavior of these curves near the boundaries $u_\pm = 0$ and $u_\pm = 1$ can be understood in the context of Proposition 4.1.1, specifically Eq. (4.1), by considering for what

values of $u_\pm$ the function $G(u; u_+, s)$ remains integrable. As in Eq. (3.26), let

$$\int_{u_+}^{u_-} G(y; u_+, s)dy = \int_{u_+}^{a} G(y; u_+, s)dy + \int_{a}^{b} G(y; u_+, s)dy + \int_{b}^{u_-} G(y; u_+, s)dy$$

where $a, b \in (0, 1)$ are fixed and chosen such that $\int_{a}^{b} G(y; u_+, s)dy < \infty$.

Let $p \in (1, 2), q \geq 2$ (as in Figure 4.4a) and consider u_+ near zero, u_- near one. Then, using Eq. (4.3),

$$\int_{u_+}^{a} G(y; u_+, s)dy \sim \frac{sM}{2-p} \left(a^{2-p} - u_+^{2-p}\right) < \infty \quad \text{as } u_+ \to 0+ . \tag{4.6}$$

On the other hand, using Eq. (4.4),

$$\int_{b}^{u_-} G(y; u_+, s)dy \sim \frac{s}{2-q} \left[(1-u_-)^{2-q} - (1-b)^{2-q}\right] \quad \text{as } u_- \to 1-, \tag{4.7}$$

which becomes infinite for $q \geq 2$. In order for saddle-saddle connections to exist and $G(u; u_+, s)$ to remain integrable, u_- must not reach one when $u_+ = 0$. In the specific case of $q = 2$, shown in Figure 4.4a, Eq. (4.7) is replaced by

$$\int_{b}^{u_-} G(y; u_+, s)dy \sim s \left[ln(1-u_-) - ln(1-b)\right] \quad \text{as } u_- \to 1-,$$

so that $\int_{u_+}^{u_-} G(y; u_+, s)dy < \infty$ for $u_- < 1$ again. Thus the Σ_τ curves avoid the corner $(u_-, u_+) = (1, 0)$ in Figure 4.4a, instead intersecting the horizontal line $u_+ = 0$ for some $u_- < 1$.

Now consider u_- near zero and u_+ near one with $p \in (1, 2), q \geq 2$ again. Notice that,

by using Eq. (4.4),

$$\int_{u_+}^{a} G(y; u_+, s) dy \sim \frac{s}{2-q} \left[(1-a)^{2-q} - (1-u_+)^{2-q} \right] \quad \text{as } u_+ \to 1-, \qquad (4.8)$$

blows up but

$$\int_{b}^{u_-} G(y; u_+, s) dy \sim \frac{sM}{2-p} \left(u_-^{2-p} - b^{2-p} \right) < \infty \quad \text{as } u_- \to 0+ \qquad (4.9)$$

with the leading order terms given in Eq. (4.3). Thus $G(u; u_+, s)$ remains integrable for u_- near zero as long as $u_+ < 1$. Taking $q = 2$ specifically, as in Figure 4.4a,

$$\int_{u_+}^{a} G(y; u_+, s) dy \sim s \left[ln(1-a) - ln(1-u_+) \right] \quad \text{as } u_- \to 1-$$

is finite as long as $u_+ < 1$. Thus it is clear that the Σ_τ curves intersect the vertical line $u_- = 0$ for some $u_+ < 1$ instead of approaching the corner $(u_-, u_+) = (0, 1)$.

The Σ_τ curves in Figure 4.4b, for which $p = 2, q = \frac{3}{2}$, behave similarly to those in Figure 4.3 with $p = q = \frac{3}{2}$. This can be explained by investigating where $G(u; u_+, s)$ becomes non-integrable again. Now, for $p \geq 2, q \in (1, 2)$, Eq. (4.6) is not finite as $u_+ \to 0+$ while Eq. (4.7) is finite as $u_- \to 1-$. Thus traveling waves exist near $u_- = 1$ with $u_+ > 0$, illustrated by the Σ_τ curve in Figure 4.4b intersecting the vertical line $u_- = 1$ for $u_+ > 0$. Similarly, as $u_+ \to 1-$, Eq. (4.8) is finite but Eq. (4.9) increases to infinity as $u_- \to 0+$. Therefore, $G(u; u_+, s)$ remains integrable and the Σ_τ curves continue as $u_+ \to 1-$ as long as $u_- > 0$.

4.4 The Riemann Problem: New Solution Structure

In this section, solutions of Eq. (3.31) are considered again but now with $p = q = \frac{3}{2}$ throughout and with the Σ_τ curves shown in Figure 4.3. The value $\tau = 10$ is used to illustrate the various solution types in Figure 4.5. It is clear that the same classical (R, S, RS) and nonclassical $(S\Sigma, R\Sigma)$ solutions appear in this integrable context as in the non-integrable case considered in chapter three. As previously addressed, the Σ_τ curves intersect the line $u_\ell = 1$, opening a new region of solutions that incorporate a shock corresponding to the sharp traveling wave from $u_- = 1$ to $u_+ = u_r$. This region is denoted by $S\Sigma^*$ since the solutions are comprised of a Lax shock (S) from u_ℓ to 1, followed by a sharp shock (Σ^*) from 1 to u_r. The sharp shock is not a Lax shock since it does not satisfy Eq. (2.27). Additionally, it is not an undercompressive shock since it is not admissible; there is not a corresponding traveling wave with $(u, v)(-\infty) = (1, 0)$ and $(u, v)(\infty) = (u_r, 0)$.

Notice that there is not a similar region for u_ℓ near zero and u_r near 1 even though the Σ_τ curves intersect the line $u_r = 1$. For pairs (u_ℓ, u_r) in this region, a rarefaction connects u_ℓ to the left state of an undercompressive shock. Then the undercompressive shock connects the middle state to $u_r = u_\Sigma$. Symmetry of the solution regions about the diagonal $u_\ell = u_r$ is not expected because the modified Buckley-Leverett equation is not symmetric itself.

Recall from chapter three that the curves separating the S and $S\Sigma$ regions consist of pairs (u_{mid}, u_r) where u_{mid} is the middle equilibrium between some u_- and $u_r = u_\Sigma$ on the Σ_τ curve. In Figure 4.5, the short curve between regions S and $S\Sigma^*$ represents the middle equilibria of the sharp shocks between 1 and u_r. For a fixed value of u_r small enough to generate such sharp fronts, the speeds of the Lax and sharp shocks become
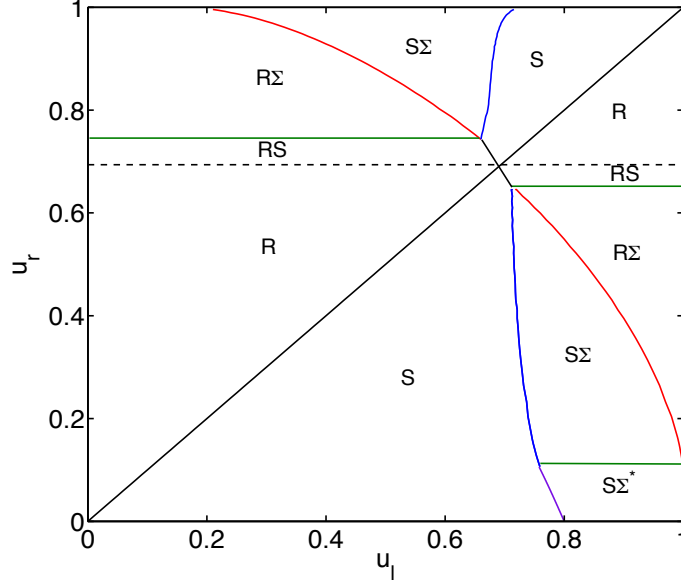
Figure 4.5: Riemann problem solutions for $p = q = \frac{3}{2}$, $M = 2$ and using Σ_{10} from Figure 4.3

closer as u_ℓ decreases until the speeds equal each other and the two shocks degenerate into a single Lax shock.

4.5 PDE Simulations

Numerical simulations of Eq. (3.5), the full PDE with a scaling parameter ϵ, are presented in this section in order to confirm and visualize the new solution structure ($S\Sigma^*$) for the Riemann problem. The approach used is based on the explicit scheme in [19] for a pseudoparabolic adaptation of Burgers equation. Eq. (3.5) is rewritten as

$$u_t = F(u, w_x)_x$$

for

$$F(u, w_x) = -f(u) + \epsilon H(u)w_x, \qquad (4.10)$$

$$w = u + \epsilon\tau u_t. \qquad (4.11)$$

Then w satisfies the elliptic equation

$$u - \epsilon\tau f(u)_x - w + \epsilon^2\tau \left(H(u)w_x\right)_x = 0. \qquad (4.12)$$

Eq. (4.11) and Eq. (4.12) are discretized on $x = [-2, 38]$ using an explicit first order upwinding scheme as in [19]. A nonlinear multigrid method originally developed for Cahn-Hilliard equations by Kim *et al.* [41] is modified to solve the discretized equations simultaneously at each iteration. See [61, 41, 64] for further details about the nonlinear full approximation storage (FAS) multigrid scheme.

Instead of the jump initial conditions used in [19], with either the upstream or downstream saturation being set equal to one, the initial condition here is a hyperbolic tangent function which approximates the discontinuity between $u_\ell = 0.9$ and $u_r = 0.025$. It is interesting to note that the simulation detects the increase to $u = 1$ without the prescribed initial condition as in [19]. Dirichlet boundary conditions are used for both variables u, w. The other parameter values used are $p = q = \frac{3}{2}, M = 2, \tau = 1$ and $\epsilon = 0.2$.

Figure 4.6 illustrates the new solution structure in which a Lax shock from $u_\ell = 0.9$ to 1 trails behind a large shock corresponding to a sharp traveling wave between 1 and $u_r = 0.025$. The oscillations in Figure 4.6a are due to the unstable spiral seen in Figure 4.2. In this integrable context, the plateau at $u = 1$ is possible and the leading sharp traveling wave has a corner at the transition from $u = 1$ to $u < 1$. Figure 4.6b only

includes the sharp traveling wave of Figure 4.6a so that the corner from $u = 1$ to $u < 1$ can be seen more clearly. It is also possible to see the traveling wave's smooth transition from $u > 0.025$ to $u = 0.025$. Finally, Figure 4.6c shows the extremely close agreement between the PDE simulation and the traveling wave generated from simulating the ODE system (3.2). The oscillations present in the traveling wave simulation are also due to the unstable spiral at the middle equilibrium shown in Figure 4.2.
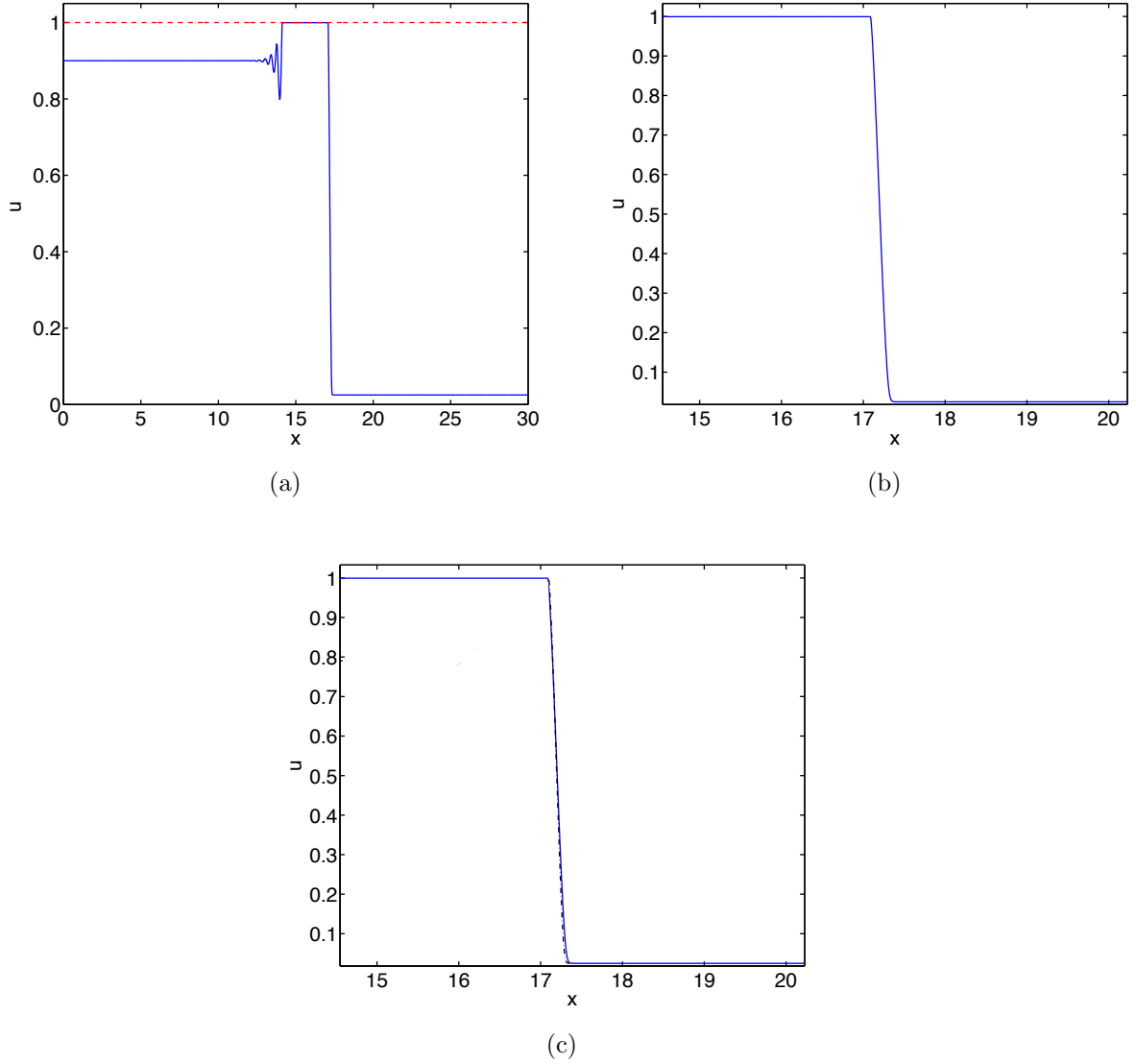
Figure 4.6: (a) Admissible Lax shock trailing a large shock corresponding to a sharp traveling wave for $u_\ell = 0.9, u_r = 0.025, \epsilon = 0.2, \tau = 1, M = 2$ (b) Traveling wave from $u_- = 1$ to $u_+ = u_r = 0.025$ in (a) with a sharp corner at the transition from $u = 1$ to $u < 1$ and a smooth corner at the transition from $u > 0.025$ to $u = 0.025$ (c) ODE simulation overlaid on PDE simulation from (b)

Chapter 5

Rate Dependent Regularization in the Modified Benjamin-Bona-Mahony-Burgers Equation

In this chapter, the Benjamin-Bona-Mahony (BBM) equation is considered with the modification of a cubic flux and Burgers dissipation term. This particular study is motivated by the mixed third order dispersion term arising in the modified Buckley-Leverett equation, due to dynamic capillary pressure. With a simpler flux function and linear regularization terms in this present context, it is possible to analytically characterize the existence of saddle-saddle connections as well as the dependence of the middle equilibrium on the speed of the traveling wave and the balance of dissipation and dispersion terms.

5.1 Introduction

The BBM equation is a third order PDE,

$$u_t + \left(\frac{1}{2}u^2 \right)_x = \mu u_{xxt}, \tag{5.1}$$

in a moving frame and with μ a constant. With the modification of a cubic (thus non-convex) flux function and a Burgers term, Eq. (5.1) becomes the modified BBM-Burgers equation

$$u_t + \left(u^3 \right)_x = \beta u_{xx} + \mu u_{xxt}. \tag{5.2}$$

The constant β is required to be positive so that the second order term is dissipative. Through Eq. (5.2), the role of the time derivative in the regularization is more simply elucidated than in the preceding chapters since the flux function here is less complicated than the Buckley-Leverett flux and the nonlinearity of the dissipation and dispersion terms in Eq. (2.17) is removed.

Jacobs, McKinney and Shearer [39] consider in detail traveling waves for the *modified* Korteweg-de Vries-Burgers (KdVB) equation in which $f(u) = u^3$,

$$u_t + \left(u^3 \right)_x = \beta u_{xx} - \mu u_{xxx}. \tag{5.3}$$

While both positive and negative cases for μ are considered in [39], admissible under-compressive shocks arise in the case $\mu < 0$. However, undercompressive shocks appear with $\mu > 0$ in Eq. (5.2) because of the sign difference of the third order terms.

5.2 Traveling Waves

As in [39], Eq. (5.2) is transformed into a third order ODE by considering traveling wave solutions of the form $u(x,t) = \tilde{u}(\eta)$, $\eta = x - st$,

$$-su' + (u^3)' = \beta u'' + \mu s u''' \tag{5.4}$$

where $s \geq 0$ represents the speed of the wave and $' = d/d\eta$. Integrating Eq. (5.4) with the same boundary conditions as in Eq. (2.21) gives the second order ODE

$$-s(u - u_-) + u^3 - u_-^3 = \beta u' + \mu s u''. \tag{5.5}$$

Then Eq. (5.5) is rescaled such that $\hat{u}(\xi) = u(\eta)$ where $\xi = \eta/\sqrt{\mu s}$, following the treatment in Section 2.3, and becomes (hats omitted)

$$u'' = -\frac{\beta}{\sqrt{\mu s}} u' + u^3 - u_-^3 - s(u - u_-), \tag{5.6}$$

where now $' = d/d\xi$. Finally, Eq. (5.6) is expressed as a first order system of ODEs:

$$u' = v \tag{5.7a}$$

$$v' = -\frac{\beta}{\sqrt{\mu s}} v + u^3 - u_-^3 - s(u - u_-). \tag{5.7b}$$

Equilibria for system (5.7) are points $(u, v) = (u, 0)$, where $u^3 - u_-^3 - s(u - u_-) = 0$; these correspond to points of intersection between the graph of $f(u) = u^3$ and the line with slope s through the point (u_-, u_-^3).

The Jacobian of system (5.7), evaluated at an equilibrium point, is

$$J(u,0) = \begin{pmatrix} 0 & 1 \\ 3u^2 - s & -\dfrac{\beta}{\sqrt{\mu s}} \end{pmatrix}$$

with eigenvalues

$$\lambda_\pm = \frac{1}{2}\left\{ -\frac{\beta}{\sqrt{\mu s}} \pm \sqrt{\frac{\beta^2}{\mu s} + 4(3u^2 - s)} \right\}.$$

In the case of three equilibria, the outside equilibria $u = u_\pm$ are saddles since $\lambda_\pm$ are real and of opposite sign as $f'(u) = 3u^2 > s$. In what follows, let u_0 denote the middle equilibrium such that $u_+ < u_0 < u_-$ with $u_+ < 0$ and $u_- > 0$. This assumption breaks down when the chord through the point (u_-, u_-^3) is tangent to the curve $f(u) = u^3$ at $u = u_+$. In this case, $u_+ = u_0 = -\dfrac{u_-}{2}$ and $s = \dfrac{3}{4}u_-^2$, so there are only two equilibria. Similarly, there are two equilibria when the chord is tangent to $f(u)$ at u_-, when $s = 3u_-^2$. Thus the speed of a traveling wave must satisfy $\dfrac{3}{4}u_-^2 < s < 3u_-^2$ in order to have three non-degenerate equilibria.

5.3   Parameter Dependencies

Mimicking the development in [39], the saddle-saddle connection between $(u_\pm, 0)$ is expressed as an invariant parabola

$$v = k(u - u_-)(u - u_+) \tag{5.8}$$

with k a constant. Note that the function $c(u) = u^3 - u_-^3 - s(u - u_-)$ in Eq. (5.7b) is a cubic polynomial; since $c(u)$ has zeros at the equilibria $u_\pm, u_0$, it can then be expressed

71

in factored form:

$$u^3 - u_-^3 - s(u - u_-) = (u - u_-)(u - u_0)(u - u_+) \tag{5.9}$$

$$= u^3 - (u_- + u_0 + u_+)u^2 + (u_-u_+ + u_0u_+ + u_-u_0)u - u_-u_0u_+. \tag{5.10}$$

By matching coefficients of the quadratic, linear and constant terms in Eq. (5.10), it is
required that

$$0 = u_- + u_0 + u_+, \tag{5.11}$$

$$-s = u_-u_+ + u_0u_+ + u_-u_0, \tag{5.12}$$

$$-u_-^3 + su_- = -u_-u_0u_+, \tag{5.13}$$

respectively.

Now Eq. (5.7), Eq. (5.8) and Eq. (5.9) are combined as follows to determine the
constant k in Eq. (5.8):

$$v\frac{dv}{du} = -\frac{\beta}{\sqrt{\mu s}}v + u^3 - u_-^3 - s(u - u_-) \tag{5.14}$$

$$[k(u - u_-)(u - u_+)][k(2u - u_- - u_+)] = -\frac{\beta}{\sqrt{\mu s}}k(u - u_-)(u - u_+) + (u - u_-)(u - u_0)(u - u_+) \tag{5.15}$$

$$k^2(2u - u_- - u_+) = -\frac{\beta k}{\sqrt{\mu s}} + (u - u_0). \tag{5.16}$$

Again equating the coefficients of the linear terms in Eq. (5.16), $2k^2 = 1$ so $k = \pm\frac{1}{\sqrt{2}}$.
With the assumption that $u_+ < u_-$, k must be positive in order for the invariant parabola
to lie below the horizontal axis in the phase plane. Specifically, then, $k = \frac{1}{\sqrt{2}}$. The
constants in Eq. (5.16) are now equated to obtain an expression for the middle equilibrium

u_0 in the case of a saddle-saddle connection (using Eq. (5.11) to eliminate $u_\pm$):

$$u_0 = -\frac{\sqrt{2}}{3\sqrt{s}}\delta \qquad (5.17)$$

where $\delta = \frac{\beta}{\sqrt{\mu}} > 0$. In [39], the equation obtained for u_0 does not depend on s; that is, $u_0 = u_0(\delta) = -\frac{\sqrt{2}}{3}\delta$ only. The dependence of u_0 on the wave speed s in this context is due to the time dependent dispersion term μu_{xxt}.

To determine the relationship between u_- and δ, Eq. (5.17) is rewritten as

$$\sqrt{u_+^2 + u_- u_+ + u_-^2}\,(u_+ + u_-) = \frac{\sqrt{2}}{3}\delta \qquad (5.18)$$

by using Eq. (5.11) and Eq. (5.12). In the limiting case of a degenerate equilibrium at u_+, let $u_+ = -\frac{u_-}{2}$ in Eq. (5.18),

$$u_-^2 = \frac{4\sqrt{2}}{3\sqrt{3}}\delta; \qquad (5.19)$$

thus δ is a quadratic function of u_-. By comparison, in [39], $u_- = \frac{2\sqrt{2}}{3}\delta$ which is linear in u_-.

5.4 Saddle-Saddle Connections

In this section, two results pertaining to values of $u_\pm$ for which there is a saddle-saddle connection (i.e., Eq. (5.18) is satisfied) are stated and proven.

Proposition 5.4.1. *Suppose $\delta = \frac{\beta}{\sqrt{\mu}} > 0$ and $u_-^2 > \frac{4\sqrt{2}}{3\sqrt{3}}\delta$ for some fixed $u_- > 0$. Then there exists a unique solution $u_+ = u_+(u_-, \delta)$ of Eq. (5.18) with $-u_- < u_+ < -\frac{u_-}{2}$; that is, there is a unique saddle-saddle connection from $(u_-, 0)$ to $(u_+, 0)$.*

Proof. Suppose that $u_+ = -u_- < 0$. Then

$$\sqrt{u_+^2 + u_- u_+ + u_-^2}\,(u_+ + u_-) - \frac{\sqrt{2}}{3}\delta < 0.$$

On the other hand, if $u_+ = -\frac{u_-}{2}$, then

$$\sqrt{u_+^2 + u_- u_+ + u_-^2}\,(u_+ + u_-) - \frac{\sqrt{2}}{3}\delta > 0$$

since $u_-^2 > \frac{4\sqrt{2}}{3\sqrt{3}}\delta$. By the Intermediate Value Theorem, there exists a solution $u_+ = u_+(u_-, \delta) \in (-u_-, -\frac{u_-}{2})$ of Eq. (5.18).

In order to demonstrate uniqueness, Eq. (3.15), Eq. (3.16) and Eq. (3.17) from chapter three are revisited in the current context. The separation function, $R(u_-, s, \gamma)$, is zero when a saddle-saddle connection from u_- to u_+ exists. The signs of the derivatives establish the uniqueness of a saddle-saddle connection. First, the vector field in system (5.7) is written as

$$K(\phi; \nu) = \begin{pmatrix} v \\ -\gamma v + s(u - u_-) - u^3 + u_-^3 \end{pmatrix}$$

where $\gamma = \frac{\beta}{\sqrt{\mu s}}$. Here, $\nu = (\delta, s, u_-)$ and the notation ν^0 represents specific parameter values. As in chapter three, the parameters in ν are treated as being independent from each other.

Then

$$\frac{\partial K}{\partial u_-} = \begin{pmatrix} 0 \\ 3(u_-)^2 - s \end{pmatrix}, \quad K \times \frac{\partial K}{\partial u_-} = v(3(u_-)^2 - s),$$

74

so that
$$\frac{\partial R}{\partial u_-}(\nu^0) = \int_{-\infty}^{\infty} e^{\gamma^0 \xi} v^0 (3(u_-^0)^2 - s^0) d\xi < 0.$$

Note that $v^0 < 0$ since $u_- > u_+$ and the saddle-saddle connection is in the lower half plane. Next, consider the parameter s:

$$\frac{\partial K}{\partial s} = \begin{pmatrix} 0 \\ u - u_- \end{pmatrix}, \qquad K \times \frac{\partial K}{\partial s} = v(u - u_-)$$

and

$$\frac{\partial R}{\partial s}(\nu^0) = \int_{-\infty}^{\infty} e^{\gamma^0 \xi} v^0 (u^0 - u_-^0) d\xi > 0. \tag{5.20}$$

Finally,

$$\frac{\partial K}{\partial \gamma} = \begin{pmatrix} 0 \\ -v \end{pmatrix}, \qquad K \times \frac{\partial K}{\partial \gamma} = -v^2.$$

Then the dependence of the separation function on γ is expressed as

$$\frac{\partial R}{\partial \gamma}(\nu^0) = -\int_{-\infty}^{\infty} e^{\gamma^0 \xi} (v^0)^2 d\xi < 0. \tag{5.21}$$

As in chapter three, let $\hat{R}(u_-, u_+, \delta) = R(u_-, s(u_-, u_+), \gamma)$ in which $\delta = \frac{\beta}{\sqrt{\mu}}$ and $\gamma = \frac{\delta}{\sqrt{s}}$. Then

$$\frac{\partial \hat{R}}{\partial u_+} = \frac{\partial R}{\partial s} \frac{\partial s}{\partial u_+} + \frac{\partial R}{\partial \gamma} \frac{\partial \gamma}{\partial s} \frac{\partial s}{\partial u_+}.$$

Note that $\frac{\partial s}{\partial u_+}$ is negative since $u_+ < -\frac{u_-}{2}$ in the region of saddle-saddle connections. Further,

$$\frac{\partial \gamma}{\partial s} = \frac{\partial}{\partial s} \left(\frac{\beta}{\sqrt{\mu s}} \right) = -\frac{\beta}{2\sqrt{\mu}} s^{-3/2} < 0 \tag{5.22}$$

since β and s are strictly positive. Thus, uniqueness follows from Eq. (5.20), Eq. (5.21)

and Eq. (5.22) so that $\frac{\partial \hat{R}}{\partial u_+} < 0$. □

Proposition 5.4.2. *Suppose $u_+ = u_+(u_-, \delta) < u_-$ is a solution of Eq. (5.18) with fixed u_-. Then, $u_-^2 > \frac{4\sqrt{2}}{3\sqrt{3}}\delta$ if and only if $u_+ < u_0$.*

Proof. First note that Eq. (5.18) is monotonic in u_+ since

$$\frac{\partial}{\partial u_+}\left(\sqrt{u_+^2 + u_- u_+ + u_-^2}(u_+ + u_-)\right) = \sqrt{u_+^2 + u_- u_+ + u_-^2} + (u_+ + u_-)\frac{2u_+ + u_-}{2\sqrt{u_+^2 + u_- u_+ + u_-^2}}$$

$$= \frac{4u_+^2 + 5u_- u_+ + 3u_-^2}{2\sqrt{u_+^2 + u_- u_+ + u_-^2}}$$

$$\neq 0.$$

Now assume that $u_-^2 > \frac{4\sqrt{2}}{3\sqrt{3}}\delta$. In order to prove $u_+ < u_0$, it suffices to show that $u_+ < -\frac{u_-}{2}$ since there are three equilibria and $u_\pm$ are saddles in this region (so $u_0 > -\frac{u_-}{2}$). The argument proceeds by contradiction; suppose that $u_+ \geq -\frac{u_-}{2}$. Then

$$\sqrt{u_+^2 + u_- u_+ + u_-^2}(u_+ + u_-) \geq \frac{\sqrt{3}\,u_-^2}{4}.$$

Thus,

$$\sqrt{u_+^2 + u_- u_+ + u_-^2}(u_+ + u_-) > \frac{\sqrt{2}}{3}\delta$$

since $\frac{4}{\sqrt{3}} > 1$. This is a contradiction to the assumption that u_+ is a solution of Eq. (5.18).

Now suppose that $u_+ < u_0$. Since there are three equilibria, it is known that $u_+ < -\frac{u_-}{2}$. Then

$$\sqrt{u_+^2 + u_- u_+ + u_-^2}(u_+ + u_-) < \frac{\sqrt{3}u_-^2}{4}.$$

Using Eq. (5.18),

$$\frac{\sqrt{2}}{3}\delta < \frac{\sqrt{3}u_-^2}{4}$$

and thus $\dfrac{4\sqrt{2}}{3\sqrt{3}}\delta < u_-^2$. $\qquad\qquad\qquad\qquad\qquad\qquad\qquad\qquad\qquad\qquad\qquad$ $\square$

5.5 The Riemann Problem

The Riemann problem associated with both Eq. (5.2) and Eq. (5.3) is:

$$u_t + (u^3)_x \;=\; 0 \qquad\qquad\qquad\qquad\qquad (5.23a)$$

$$u(x,0) \;=\; \begin{cases} u_\ell & \text{if } x < 0 \\[2mm] u_r & \text{if } x > 0. \end{cases} \qquad\qquad\qquad (5.23b)$$

Classical and nonclassical solutions of Eq. (5.23) are presented using Σ_δ curves to separate the regions of nonclassical solutions as in chapter three. The parameter δ is taken to be one for simplicity. Recall from chapters three and four that rarefactions, Lax shocks and undercompressive shocks are denoted by R, S and Σ, respectively.

In Figure 5.5, the solution regions are separated by various curves similarly appearing in Figure 3.4 and Figure 4.5. For clarity, the curves are described again but in the current context. The long diagonal black line between the region of rarefactions and Lax shocks is the line $u_r = u_\ell$. The short black curve separating the S and SR regions is the set of points (u_ℓ, u_α) such that the chord between u_ℓ and u_α is tangent to $f(u) = u^3$ at $u = u_\alpha$. In the case $\delta = 1$, the value of u_ℓ for which saddle-saddle connections no longer exist is $\sqrt{\dfrac{4\sqrt{2}}{3\sqrt{3}}}$, from Eq. (5.19); thus the vertical green line at $u_\ell = \sqrt{\dfrac{4\sqrt{2}}{3\sqrt{3}}}$ is the boundary between regions of classical and nonclassical solutions, SR and ΣR. The red Σ_1 curve separates the nonclassical solution regions as it represents pairs (u_ℓ, u_r) for which there is a saddle-saddle connection and thus a single admissible undercompressive shock solution to Eq. (5.23). Finally, the blue curve between the S and ΣS regions represents the middle

equilibria of the saddle-saddle connections on Σ_1.
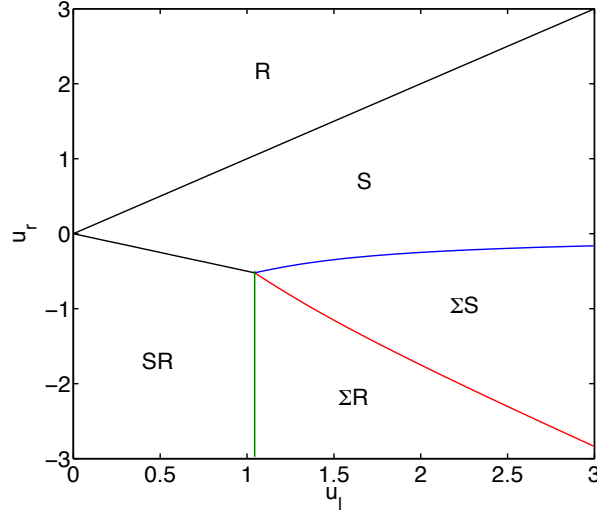
Figure 5.1: Solutions of Eq. (5.23) for various initial conditions (u_ℓ, u_r) such that $u_\ell > 0, \delta = 1$

Two general solution sets are obtained by fixing u_ℓ and letting u_r vary. First, if $u_\ell < \sqrt{\dfrac{4\sqrt{2}}{3\sqrt{3}}}$, the classical solutions of a rarefaction, Lax shock and combination rarefaction-Lax shock are observed as u_r decreases. However, if $u_\ell > \sqrt{\dfrac{4\sqrt{2}}{3\sqrt{3}}}$, then the nonclassical solutions appear for negative values of u_r. Specifically, a rarefaction connects the left and right states if $u_r > u_\ell$. As u_r decreases, a Lax shock is obtained as long as u_r is larger than the middle equilibrium of the saddle-saddle connection between u_ℓ and u_Σ on the Σ_1 curve. Once u_r is small enough, it is connected to u_ℓ by a combination of an admissible undercompressive shock trailing behind a leading Lax shock. Finally, for even more negative u_r, the solution of Eq. (5.23) consists of a rarefaction followed by an admissible undercompressive shock. Notice that the order of solutions in the SR, ΣR

and ΣS regions is reversed from those in Figure 3.4 and Figure 4.5. This is due to the opposite concavity between the Buckley-Leverett flux and the current cubic flux function.

Even though the formulae obtained here for Eq. (5.2) differ from those in [39], the regions of solutions are very similar. The values of (u_ℓ, u_r) which separate them differ between these two accounts due to the time dependent regularization; however, the general structure for solutions of the Riemann problem is preserved.

Chapter 6

Stability of Plane Waves

The stability of a planar sharp front is analyzed for a simplified system in which capillary pressure is ignored. The analysis is based on linearizing the equations about the front solution, which includes linearization of suitable jump conditions. Solutions of the linearized system are calculated to leading order in the wave number $\alpha << 1$ of long-wave transverse perturbations of the front. Perturbations grow or decay exponentially with rate $\sigma(\alpha)$ which has a dispersion relation of the form $\sigma(\alpha) \sim \sigma_1 \alpha$ as $\alpha \to 0$, just as in Saffman and Taylor's original paper [52]. Numerical simulations of both stable and unstable waves support the analytical results.

6.1   Simplified Equations and Plane Waves

In the limit of vanishing capillary pressure, Eq. (2.6) and Eq. (2.8) become

$$\varphi \frac{\partial u}{\partial t} - \nabla \cdot (\lambda^w(u)\nabla p) = 0 \tag{6.1}$$

$$\nabla \cdot (\lambda^T(u)\nabla p) = 0. \tag{6.2}$$

Here, p^w is written as p for simplicity. In what follows, $\varphi = 1$ without loss of generality, since it can be absorbed into the time variable. These simplified equations admit solutions with sharp interfaces, i.e. jump discontinuities in the saturation u and the pressure gradient ∇p.

Since perturbations are about a sharp planar interface $x = Vt$ moving with speed V, sharp curved interfaces of the form $x = \hat{x}(y, t)$ are considered. Then the normal vector to the surface $F(x, y, t) \equiv x - \hat{x}(y, t) = 0$ is $\mathbf{n} = (\partial_x F, \partial_y F, \partial_t F) = (1, -\hat{x}_y, -\hat{x}_t)$. Both Eqs. (6.1), (6.2) are in divergence form (in space-time), so that jump conditions are

$$-\hat{x}_t[u] - [\lambda^w(u)p_x] + \hat{x}_y[\lambda^w(u)p_y] \;=\; 0 \tag{6.3}$$

$$[\lambda^T(u)p_x] - \hat{x}_y[\lambda^T(u)p_y] \;=\; 0. \tag{6.4}$$

In what follows, Eq. (6.1) and Eq. (6.2) are considered with a single interface satisfying Eq. (6.3) and Eq. (6.4).

Plane waves depend on a single spatial variable and time; consequently, the phase velocities are scalar in the direction of propagation of the plane wave. Taking the direction to be parallel to the x - axis, plane wave solutions $u = u(x, t)$, $p = p(x, t)$ of Eq. (2.6), Eq. (2.7) are independent of y. The incompressibility condition Eq. (2.2) reduces to $\partial_x U = 0$, where U is the (scalar) total velocity. In principle, this velocity could depend on time, but it can be taken to be constant by adjusting the time scale accordingly. In terms of u, p we find from Eq. (2.7),

$$\lambda^T(u)p_x + \lambda^n(u)p^c(u)_x = -U = const. \tag{6.5}$$

Now p_x can be eliminated, resulting in a scalar equation which is the one-dimensional

version of Eq. (6.1):

$$u_t + f(u)_x = -\left(H(u)p^c(u)_x\right)_x \tag{6.6}$$

where $f(u)$ and $H(u)$ are given by Eq. (2.12) and Eq. (2.13), respectively. Eq. (6.6) has smooth traveling wave solutions that can be analyzed directly. Sharp interfaces are realized when the capillary pressure is taken to be negligible: $p^c(u) \equiv 0$. The associated saturations and pressures can be interpreted as far-field states for the smooth traveling waves.

Consider a planar interface $x = Vt$ moving with speed V. Let $u = \bar{u}_\pm, p = \bar{p}_\pm$ denote the saturation and pressure on either side of the interface. Then $\bar{u}_\pm$ are constant, and $\bar{p}_\pm$ are linear. Letting $p^c(u) \equiv 0$ in Eq. (6.6) the equation reduces to the scalar conservation law

$$u_t + f(u)_x = 0.$$

An alternative form of the flux function,

$$f(u) = -\lambda^w(u)p_x = U\frac{\lambda^w(u)}{\lambda^T(u)}, \tag{6.7}$$

and its derivative

$$f'(u) = U\frac{\lambda^w(u)}{\lambda^T(u)}\left[\frac{(\lambda^w(u))'}{\lambda^w(u)} - \frac{(\lambda^T(u))'}{\lambda^T(u)}\right] \tag{6.8}$$

will be useful in the following analysis.

The jump in u is a shock wave

$$u(x,t) = \begin{cases} \bar{u}_-, & x < Vt \\ \\ \bar{u}_+, & x > Vt \end{cases}$$

that necessarily satisfies the Rankine-Hugoniot condition

$$V = \frac{f(\bar{u}_+) - f(\bar{u}_-)}{\bar{u}_+ - \bar{u}_-}.$$

The total velocity, U, and the speed of the interface, V, are not necessarily equal when the saturations are variable; using Eq. (6.7),

$$V = U \frac{\frac{\lambda^w(\bar{u}_+)}{\lambda^T(\bar{u}_+)} - \frac{\lambda^w(\bar{u}_-)}{\lambda^T(\bar{u}_-)}}{\bar{u}_+ - \bar{u}_-}.$$

In the case of pure fluids, as considered by Saffman and Taylor, $\bar{u}_+ = 0$ and $\bar{u}_- = 1$ so that $V = U$.

Associated with this shock wave are pressure fields $\bar{p}_\pm$ on either side, that are calculated from Darcy's law (Eq. (2.3)). This is contained in the jump condition Eq. (6.4) involving the pressures, which together with Eq. (6.5) gives

$$\lambda^T(\bar{u}_+)(\bar{p}_+)_x = \lambda^T(\bar{u}_-)(\bar{p}_-)_x = -U. \tag{6.9}$$

Thus, expressions for $\bar{p}_\pm$ are obtained by integrating $(\bar{p}_\pm)_x = \frac{-U}{\lambda^T(\bar{u}_\pm)}$:

$$\bar{p}_\pm = \frac{-U}{\lambda^T(\bar{u}_\pm)} x + c_\pm(t)$$

where $c_\pm(t)$ are arbitrary functions. Continuity of pressure at the interface $x = Vt$ determines $c_\pm(t)$:

$$c_+(t) - c_-(t) = \frac{-U}{\lambda^T(\bar{u}_+)} Vt - \frac{-U}{\lambda^T(\bar{u}_-)} Vt.$$

Then let $c_+(t) = \frac{-U}{\lambda^T(\bar{u}_+)}Vt$ and $c_-(t) = \frac{-U}{\lambda^T(\bar{u}_-)}Vt$ so that

$$\bar{p}_\pm = \frac{-U}{\lambda^T(\bar{u}_\pm)}(x - Vt). \tag{6.10}$$

To summarize, the planar interface whose stability is studied in the next section involves a jump in u, whereas the pressure is linear on each side and continuous across the interface.

6.2 Long Wave Stability Analysis

Investigated here is the long wave stability of the sharp interface solution presented in the previous section. To start, the equations and jump conditions are linearized. Let $x = \hat{x}(y,t) = Vt + \hat{z}(y,t)$ denote the perturbed interface. Consider a discontinuous saturation function

$$u = \begin{cases} u_-(z,y,t), & z < \hat{z}(y,t) \\ \\ u_+(z,y,t), & z > \hat{z}(y,t), \end{cases}$$

in which $z = x - Vt$. Corresponding pressures are denoted $p_\pm(z,y,t)$ on either side of the interface. Specifically, we choose perturbations with transverse wave number $\alpha \geq 0$ and temporal growth rate σ :

$$\begin{aligned} u_\pm(z,y,t) &= \bar{u}_\pm + W_\pm(z), \quad W_\pm(z,y,t) = w_\pm(z)e^{i\alpha y + \sigma t} & (6.11) \\ p_\pm(z,y,t) &= \bar{p}_\pm(z) + Q_\pm(z), \quad Q_\pm(z,y,t) = q_\pm(z)e^{i\alpha y + \sigma t} & (6.12) \\ \hat{z}(y,t) &= ae^{i\alpha y + \sigma t}, & (6.13) \end{aligned}$$

where a is constant and the functions $W_\pm(z), Q_\pm(z)$ are required to be bounded as $z \to \pm\infty$ (respectively).

The goal is to determine the leading order dependence of the functions $w_\pm, q_\pm$ on small values of α (long waves). The leading order behavior of the growth rate σ is linear in α :

$$\sigma = \sigma_1 \alpha + \sigma_2 \alpha^2 + \ldots, \qquad \text{as } \alpha \to 0.$$

The coefficient σ_1 controls stability of the front to transverse perturbations; if $\sigma_1 > 0$, then the plane wave is unstable to long waves, and if σ_1 is negative, then the front is stable, assuming that $\sigma(\alpha) < 0$ also at larger wave numbers.

Substituting Eq. (6.11) and Eq. (6.12) into Eq. (6.1) and Eq. (6.2) and linearizing gives the ODE system

$$(W_\pm)_t - (\lambda^w(\bar{u}_\pm))' \bar{p}_\pm (W_\pm)_x - \lambda^w(\bar{u}_\pm) \Delta Q_\pm = 0 \tag{6.14}$$

$$(\lambda^T(\bar{u}_\pm))' \bar{p}_\pm (W_\pm)_x + \lambda^T(\bar{u}_\pm) \Delta Q_\pm = 0. \tag{6.15}$$

Next it is argued that $W_\pm(z) \equiv 0$ if $Re(\sigma) \geq 0$. From Eq. (6.15),

$$\Delta Q_\pm = -\frac{(\lambda^T(\bar{u}_\pm))' \bar{p}_\pm (W_\pm)_x}{\lambda^T(\bar{u}_\pm)}.$$

Using this in Eq. (6.14) gives

$$(W_\pm)_t - \bar{p}_\pm (W_\pm)_x \lambda^w(\bar{u}_\pm) \left[\frac{(\lambda^w(u))'}{\lambda^w(u)} - \frac{(\lambda^T(u))'}{\lambda^T(u)} \right] = 0,$$

which reduces to

$$\sigma w_\pm - V w_\pm' - \bar{p}_\pm w_\pm' \frac{f'(\bar{u}_\pm) \lambda^T(\bar{u}_\pm)}{U} = 0 \tag{6.16}$$

after substituting $W_\pm(z, y, t) = w_\pm(z) e^{i\alpha y + \sigma t}$ and using Eq. (6.8). Notice that $p_x =$

85

$(\bar{p}_\pm)_x = -\frac{U}{\lambda^T(\bar{u}_\pm)}$ from Eq. (6.7) and Eq. (6.10). Then Eq. (6.16) simplifies to

$$\sigma w_\pm = w'_\pm (V - f'(\bar{u}_\pm))$$

and indicates that $w_\pm(z) = \gamma_\pm e^{\frac{\sigma}{V - f'(\bar{u}_\pm)} z}$. In the absence of capillary pressure, all shocks are Lax shocks so that if $z > 0$, then $V - f'(\bar{u}_+) > 0$. Assuming that $Re(\sigma) \geq 0$, $w_\pm$ grows exponentially so that $W_\pm$ is not bounded as $z \to \infty$ as required. On the other hand, if $z < 0$, then $V - f'(\bar{u}_-) < 0$ and $w_\pm$ again grows exponentially as $z \to -\infty$ if $Re(\sigma) \geq 0$. Again, $W_\pm$ is not bounded. Thus, if $Re(\sigma) \geq 0$, then $W_\pm \equiv 0$ as claimed.

With $W_\pm \equiv 0$, system (6.14), (6.15) reduces to the same equation for $q_\pm$:

$$q''_\pm - \alpha^2 q_\pm = 0.$$

Thus,

$$\begin{cases} q_-(z) = b_- e^{\alpha(z - \hat{z})}, & z < \hat{z} \\ \\ q_+(z) = b_+ e^{-\alpha(z - \hat{z})}, & z > \hat{z}. \end{cases} \tag{6.17}$$

Next, the coefficients $b_\pm$ are related to the amplitude a of the perturbed interface and the coefficient σ_1. This calculation is simplified by the result $w_\pm \equiv 0$. The linearized jump conditions then reduce to leading order to

$$\sigma_1 \alpha a [\bar{u}] + [\lambda^w(\bar{u}) q'] = 0 \quad \text{from Eq. (6.3)} \tag{6.18}$$

$$[\lambda^T(\bar{u}) q'] = 0 \quad \text{from Eq. (6.4)}. \tag{6.19}$$

Here, quadratic and higher order terms in α have been dropped. Using Eq. (6.17) in

86

Eq. (6.19) at the interface $z = \hat{z}$, a linear equation is obtained for the constants $b_{\pm}$:

$$\lambda^T(\bar{u}_-)b_- + \lambda^T(\bar{u}_+)b_+ = 0. \tag{6.20}$$

Similarly, Eq. (6.18) becomes

$$\sigma_1 a(\bar{u}_+ - \bar{u}_-) - \lambda^w(\bar{u}_+)b_+ - \lambda^w(\bar{u}_-)b_- = 0. \tag{6.21}$$

Now $\lambda^w(u) = f(u)\lambda^T(u)/U$, from Eq. (6.7), so that Eq. (6.21) becomes

$$\sigma_1 a(\bar{u}_+ - \bar{u}_-) - \frac{f(\bar{u}_+)\lambda^T(\bar{u}_+)}{U}b_+ - \frac{f(\bar{u}_-)\lambda^T(\bar{u}_-)}{U}b_- = 0. \tag{6.22}$$

Finally, continuity of pressure, $p_+(z) = p_-(z)$, is used at the interface $z = \hat{z} = ae^{i\alpha y + \sigma t}$ with Eq. (6.17) to arrive at a third linear equation for the coefficients $a, b_{\pm}$:

$$-\frac{U}{\lambda^T(\bar{u}_+)}a + b_+ = -\frac{U}{\lambda^T(\bar{u}_-)}a + b_-. \tag{6.23}$$

Nontrivial solutions for the constants $a, b_{\pm}$ can be determined from the linear system of Eq. (6.20), Eq. (6.22) and Eq. (6.23) precisely when the coefficient matrix is singular. After some manipulation, an expression for the coefficient σ_1 is obtained:

$$\sigma_1 = V\frac{\lambda^T(\bar{u}_-) - \lambda^T(\bar{u}_+)}{\lambda^T(\bar{u}_-) + \lambda^T(\bar{u}_+)}. \tag{6.24}$$

This relation governs the growth or decay of perturbations, to leading order in the wave number. In particular, it controls whether the sharp interface is stable or unstable: when the total mobility upstream, $\lambda^T(\bar{u}_-)$, is larger than that downstream, $\lambda^T(\bar{u}_+)$, then

$\sigma_1 > 0$, so that for long waves, the growth rate is positive and the interface between the phases is susceptible to the Saffman-Taylor fingering instability.

When the variable saturations are restricted to constant states $\bar{u}_- = 1, \bar{u}_+ = 0$, in the context of pure fluids considered by Saffman and Taylor in [52],

$$
\begin{aligned}
\lambda^T(\bar{u}_-) &= \lambda^w(1) = \frac{K\kappa^w}{\mu^w}, \\
\lambda^T(\bar{u}_+) &= \lambda^n(0) = \frac{K\kappa^n}{\mu^n}
\end{aligned}
$$

using Eq. (2.4) and the associated notation from chapter two. Now Eq. (6.24) becomes

$$
\sigma_1 = V \frac{\frac{\kappa^w}{\mu^w} - \frac{\kappa^n}{\mu^n}}{\frac{\kappa^w}{\mu^w} + \frac{\kappa^n}{\mu^n}}
$$

which reduces to

$$
\sigma_1 = V \frac{\kappa^w \mu^n - \kappa^n \mu^w}{\kappa^w \mu^n + \kappa^n \mu^w}. \tag{6.25}
$$

Recalling the viscosity ratio $M = \frac{\kappa^n \mu^w}{\kappa^w \mu^n}$, the general result of Eq. (6.24) is reduced to

$$
\sigma_1 = V \frac{1 - M}{1 + M} \tag{6.26}
$$

after multiplying both the numerator and denominator of Eq. (6.25) by $\frac{1}{\kappa^w \mu^n}$. Eq. (6.26) is the original result from [52]; it states that the viscous fingering instability develops when $M < 1$, i.e. the viscosity of the displacing fluid (e.g. water) is less than the viscosity of the fluid displaced (e.g. oil).

6.3 Stable and Unstable Lax Shocks

The boundary between regions of stable and unstable shocks is the curve

$$\lambda^T(\bar{u}_-) = \lambda^T(\bar{u}_+) \tag{6.27}$$

in the $(\bar{u}_-, \bar{u}_+)$ plane. How this relates to the Lax entropy condition, $f'(\bar{u}_+) < V < f'(\bar{u}_-)$, is elucidated below. In the case of quadratic relative permeabilities, Eq. (6.27) becomes

$$\bar{u}_-^2 + M(1 - \bar{u}_-)^2 = \bar{u}_+^2 + M(1 - \bar{u}_+)^2.$$

Factoring $\bar{u}_+ - \bar{u}_- \neq 0$ gives the linear equation

$$\bar{u}_+ + \bar{u}_- \;\; = \;\; \frac{2M}{1 + M}$$

for $\bar{u}_- > \bar{u}_+$. This line is shown in Figure 6.1 and separates the region of stable Lax shocks from the region of unstable Lax shocks. The right boundary of the region of unstable Lax shocks represents the pairs $\bar{u}_\pm$ for which the chord between them is tangent to the flux curve f at $\bar{u}_+$; for values of $\bar{u}_\pm$ past this curve, the Lax entropy condition is no longer satisfied. The inflection point of the flux function $(u_i, f(u_i))$ is marked in the figure.

6.4 Numerical Calculations

Equations (2.6), (2.8) are solved numerically with the simplifying assumption $p^c(u) = -u$ as in chapters two and three. The domain is a rectangle given by $[-L, L] \times [-H, H]$.
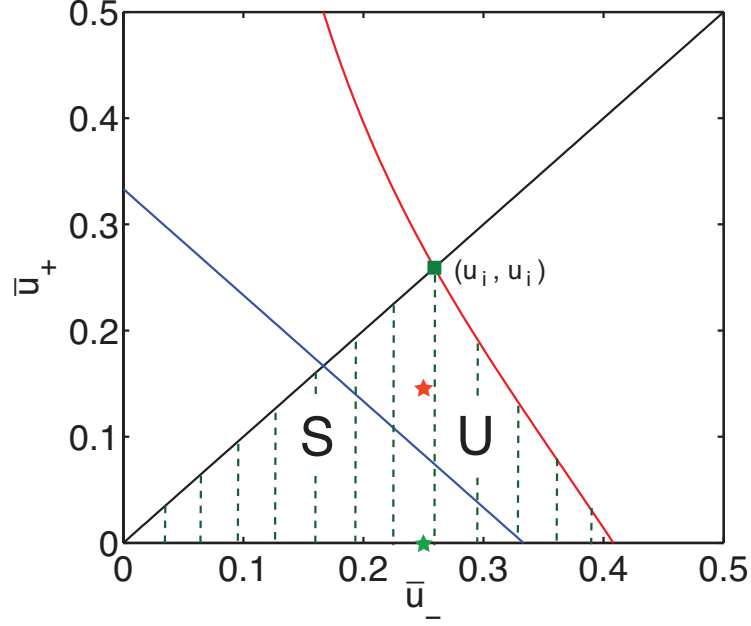
Figure 6.1: Regions of stable (S) and unstable (U) Lax shocks for quadratic relative permeabilities and M=0.2. The stars are representative points used in the numerical simulations.

With $\nabla p^c(u) = -\nabla u$, Eq. (2.6) and Eq. (2.8) become

$$\phi\frac{\partial u}{\partial t} - \nabla \cdot (\lambda^w(u)\nabla p) = 0 \tag{6.28}$$

$$\nabla \cdot \left(\lambda^T(u)\nabla p - \lambda^n(u)\nabla u\right) = 0. \tag{6.29}$$

As previously mentioned, the system has traveling wave solutions with the same speed as the sharp planar interface satisfying Eq. (6.1) and Eq. (6.2). Since any instability is localized around the sharp interface $x = Vt$, Eq. (6.29) is transformed into a moving frame with speed V:

$$\varphi\frac{\partial u}{\partial t} - V\frac{\partial u}{\partial x} - \nabla \cdot (\lambda^w(u)\nabla p) = 0. \tag{6.30}$$

The boundary conditions in the transverse y-direction are periodic in both u and p

while those in the x-direction are

$$u(-L) = u_-, \quad u(L) = u_+, \quad p(-L) = 0, \quad \frac{\partial p}{\partial x}(L) = -\frac{U}{\lambda^T(u(L))},$$

the final condition derived from Eq. (6.9).

The y direction is scaled by $2H$, the width of the domain, to allow for better illustrations of the long wavelength profile. As earlier, $\varphi = 1$, effectively choosing a timescale based on the porosity φ. Then Eq. (6.30) and Eq. (6.15) become

$$\frac{\partial u}{\partial t} - V\frac{\partial u}{\partial x} - \frac{\partial}{\partial x}\left(\lambda^w(u)\frac{\partial}{\partial x}p\right) - \frac{1}{4H^2}\frac{\partial}{\partial y}\left(\lambda^w(u)\frac{\partial}{\partial y}p\right) = 0 \quad (6.31)$$

$$\frac{\partial}{\partial x}\left(\lambda^T(u)\frac{\partial}{\partial x}p - \lambda^n(u)\frac{\partial}{\partial x}u\right) + \frac{1}{4H^2}\frac{\partial}{\partial y}\left(\lambda^T(u)\frac{\partial}{\partial y}p - \lambda^n(u)\frac{\partial}{\partial y}u\right) = 0. \quad (6.32)$$

These equations are solved using a fully implicit Crank-Nicolson time step, a centered difference discretization for second-order spatial derivatives and upwinding for the convective term $V\frac{\partial u}{\partial x}$ in Eq. (6.31). The nonlinear multigrid method from [41], mentioned in chapter four, efficiently solves the discrete system at the implicit time level.

Representative values of $\bar{u}_\pm$ are used in the simulations in order to confirm the stability boundary discussed in the previous section. The initial saturation is represented by a hyperbolic tangent function with its interface perturbed by a sinusoidal wave and superimposed random noise:

$$u_0(x, y) = \frac{\bar{u}_+ - \bar{u}_-}{2}\left(1 - \tanh\left(\frac{x - \eta(x, y) - 0.01\sin(2\pi y)}{2M}\right)\right) + \bar{u}_-,$$

where $\eta(x, y)$ is a random number at (x, y) satisfying $-0.01 \leq \eta(x, y) \leq 0.01$. Note that the perturbation is chosen to be consistent with the longest wavelength for the

chosen domain. Specifically, the wave number is related to the width by $\alpha = \dfrac{\pi}{H}$. In both simulations, $M = 0.2, L = 4$ and $H = 6$.

To visualize solutions in the stable region of Figure 6.1, let $\bar{u}_- = 0.25$ and $\bar{u}_+ = 0$. Additionally, let $U = 1$. The saturation contour $u = \frac{1}{2}(\bar{u}_- + \bar{u}_+)$ is plotted in Figure 6.2a-f at various times. The amplitude of the perturbed interface decays in time, as expected. Figure 6.2g shows the amplitude of the saturation contour compared with the linear (Eq. (6.24)) and the quadratic (from [66]) approximations to the growth rate $\sigma(\alpha)$. In the latter case,

$$\sigma(\alpha) \approx \sigma_1 \alpha + \sigma_2 \alpha^2, \tag{6.33}$$

with σ_1 given by Eq. (6.24) and

$$
\begin{aligned}
\sigma_2 \;=\;& \frac{-4\lambda^T(\bar{u}_+)\lambda^T(\bar{u}_-)}{(\bar{u}_- - \bar{u}_+)(\lambda^T(\bar{u}_+)+\lambda^T(\bar{u}_-))^2} \int_{\bar{u}_+}^{\bar{u}_-} \frac{\lambda^n(u)\lambda^w(u)}{\lambda^T(u)}\, du \\
&+ \frac{2}{(\bar{u}_- - \bar{u}_+)(\lambda^T(\bar{u}_+)+\lambda^T(\bar{u}_-))^2} \int_{\bar{u}_+}^{\bar{u}_-} \frac{\lambda^n(u)\lambda^w(u)}{\lambda^T(u)(f(u)-f(\bar{u}_+)-V(u-\bar{u}_+))}I\, du,
\end{aligned}
\tag{6.34}
$$

where $I = \lambda^T(\bar{u}_-)(\lambda^T(u)-\lambda^T(\bar{u}_+))(f(\bar{u}_-)-f(u))+\lambda^T(\bar{u}_+)(\lambda^T(\bar{u}_-)-\lambda^T(u))(f(u)-f(\bar{u}_+))$. The flux function $f(\cdot)$ in Eq. (6.34) is calculated by using quadratic relative permeabilities as in chapters two and three. The original version of Eq. (6.34) appearing in [66] includes the derivative of the equilibrium capillary pressure with respect to the wetting saturation in the first integral; taking $p_e^c(u) = -u$ (as mentioned previously) gives $\frac{dp_e^c}{du} = -1$ and produces the negative coefficient in the first term. Also, Yortsos and Hickernell integrate along the traveling wave in the second term of Eq. (6.34) whereas it has been re-expressed here much more simply as an integral with respect to u. With the given parameter values stated above ($\bar{u}_- = 0.25, \bar{u}_+ = 0, U = 1, M = 2, L = 4, H = 6$), $\sigma_1 = -0.09524$ and $\sigma_2 = -0.01431$.

While the saturation contour and approximations are nearly indistinguishable, it can

be seen that the linear approximation slightly under-predicts the decay rate. As expected, the quadratic approximation matches the simulation values better. However, there is not a significant difference between the two approximations in this stable case.

The advantage of the quadratic approximation is much clearer when $(\bar{u}_-, \bar{u}_+)$ is taken from the unstable region in Figure 6.1. Specifically, let $\bar{u}_- = 0.25, \bar{u}_+ = 0.15$ and $U = 2$. Now $\sigma_1 = 0.05203$ and $\sigma_2 = -0.04212$. Figure 6.3a-f illustrate the development of the Saffman-Taylor fingering instability with the aforementioned parameter values. In early times (Figure 6.3a-c), the short wavelength perturbations decay quickly, as they correspond to high, and thus stable, amplitudes. On the other hand, the long wavelength perturbations grow slowly, as seen in Figure 6.3d-f. Figure 6.3g is another comparison plot but now in the unstable case. As in Figure 6.2g, the quadratic approximation very closely agrees with the simulation. There is a significant difference between the accuracies of the linear and quadratic approximations now; the former dramatically over-predicts the growth rate from the contour plot.

It has been shown, through exploitation of the underlying hyperbolic structure in the model, that stability of planar fronts in two phase immiscible flow in a porous medium is governed by the mobility difference between the two phases. The interpretation is that, with realistic relative permeability ratios, to stabilize a front in which water is displacing oil, the displacing fluid should be an oil-rich mixture of oil and water. While such a mixture may not be achievable in practice, nonetheless the analysis here is indicative of how these fronts can be analyzed. In particular, the Saffman-Taylor analysis of sharp fronts can be extended to allow for variable saturations, demonstrating that stability depends on the interplay between the hyperbolic conservation law derived by Buckley and Leverett and the elliptic equation that expresses incompressibility of the two phase mixture.

Figure 6.2: Simulation results in the stable case. (a)-(f) Contours of the saturation at $u = \frac{1}{2}(\bar{u}_- + \bar{u}_+)$ at various times. (g) Amplitude versus time. Black circles: numerical amplitude calculated at $u = \frac{1}{2}(\bar{u}_- + \bar{u}_+)$, blue dashed line: amplitude predicted by Eq. (6.24), and red solid line: amplitude predicted by Eq. (6.33)
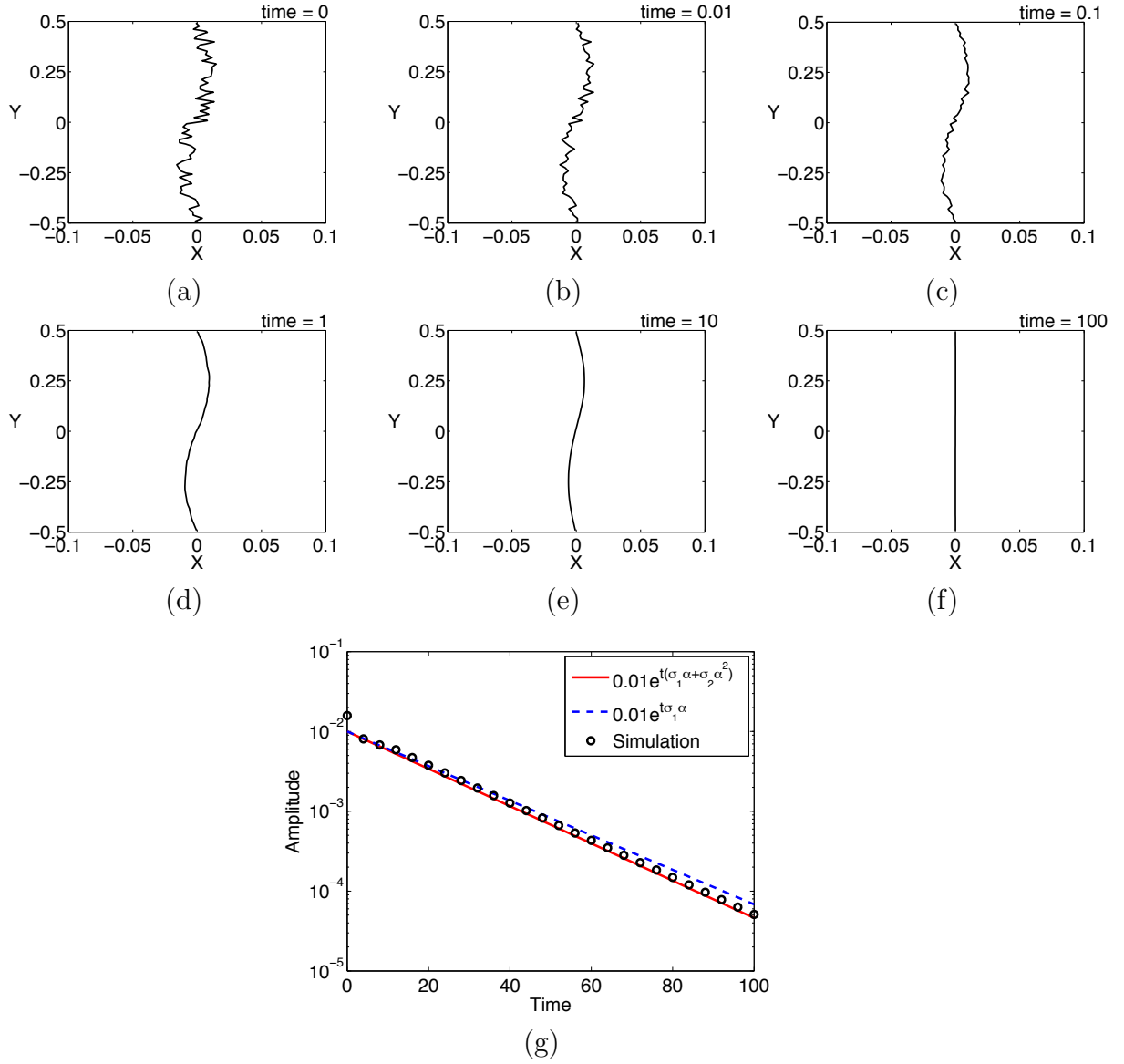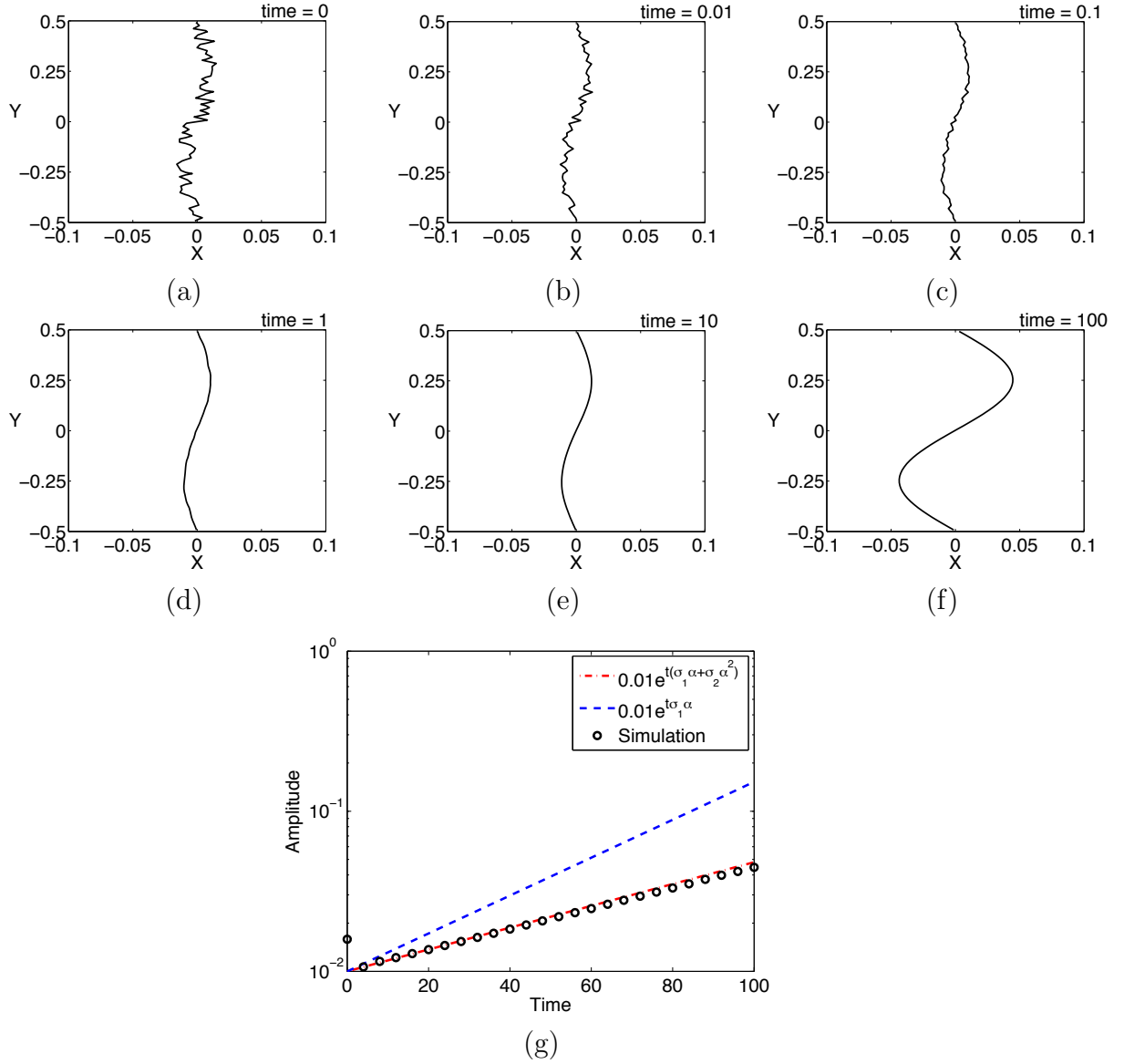
Figure 6.3: Simulation results of unstable case. (a)-(f) Contours of the saturation at $u = \frac{1}{2}(\bar{u}_- + \bar{u}_+)$ at various times. (g) Amplitude versus time. Black circles: numerical amplitude calculated at $u = \frac{1}{2}(\bar{u}_- + \bar{u}_+)$, blue dashed line: amplitude predicted by Eq. (6.24), and red dashed-dotted line: amplitude predicted by Eq. (6.33)

Chapter 7

Conclusions

The results described in the previous chapters elucidate how solutions to the modified Buckley-Leverett equation evolve. New solution structures are considered in chapters three and four while the impact of time dependent dispersion is investigated in chapter five. The stability of sharp planar fronts is analyzed and characterized in chapter six. The remainder of the current chapter is a summary of the work and aforementioned conclusions.

In chapter three, a new perspective is offered in the analysis of the Buckley-Leverett equation with time dependent regularization, specifically in the case of quadratic relative permeability functions. By considering traveling wave solutions to the PDE, the equation is transformed into a first order system of ODEs. Regions are identified for which the ODE system has three equilibria; that is, the upstream and downstream saturations are connected by undercompressive shocks. Phase portraits, as in Figure 3.2, and a separation function described in Section 3.2 are used to identify when a saddle-saddle connection exists between an upstream saturation u_- and a downstream saturation u_+. These pairs lead to the Σ_τ curves illustrated in Figure 3.3 with the specific properties addressed in

Propositions 3.3.1, 3.3.2: namely the smoothness and asymptotic behavior of Σ_∞ as well as existence, uniqueness, smoothness and monotonicity of Σ_τ (τ finite) in τ and u_-. Classical and nonclassical solutions of the Riemann problem are then presented in Figure 3.4 with a Σ_τ curve as the boundary between the two nonclassical solution structures involving undercompressive shocks. Finally, numerical simulations of the full PDE verify the theoretical results. In particular, simulation of the Lax shock-undercompressive shock combination produces the same qualitative non-monotonic behavior of the saturation front as in physical experiments described in [22].

With the general framework established in chapter three, sharp traveling wave solutions of the modified Buckley-Leverett equation are investigated in chapter four. The integrability condition from [18] and reproduced in Proposition 4.1.1 is satisfied when the relative permeability functions are no longer both quadratic. Fractional exponents, specifically $p = q = \frac{3}{2}$, are used to establish a new context in which sharp traveling waves are possible. Figure 4.2 illustrates the mechanism behind the sharp traveling wave; the unstable manifolds leaving u_+ intersect the line $u = 1$ in finite time and provide the discontinuity in u' which accounts for the corner in the traveling wave at the transition from $u = 1$ to $u < 1$. The Σ_τ curves now intersect the lines $u_\pm = 1$ for nonzero $u_\mp$. This is significantly different from the case considered in chapter three, in which the Σ_τ curves approach the corners $(u_-, u_+) = (0, 1), (1, 0)$ in a limiting sense only. Solutions to the Riemann problem now include a combination of an admissible Lax shock and a leading shock corresponding to a sharp traveling wave between an upstream saturation of one and a downstream saturation close to zero. Numerical simulations are provided again to validate and visualize solutions from the $S\Sigma^*$ region in Figure 4.5.

In an effort to better understand the role of time dependent regularization on solutions of the modified Buckley-Leverett equation, the modified BBM-Burgers equation is

considered in chapter five. The flux is now only a cubic function, much simpler and easier to analyze than the Buckley-Leverett flux, and the dissipation and dispersion terms are linear. A completely analytical characterization (Eq. (5.18)) of saddle-saddle connections is possible with these amendments. Existence and uniqueness of such a connection are given in Proposition 5.4.1 and shown by using Eq. (5.18) and the separation function introduced in chapter three. Proposition 5.4.2 describes the required relationship between the three equilibria u_-, u_0, u_+ and the balance between dissipation and dispersion coefficients in the case of a saddle-saddle connection. Finally, the Riemann problem is solved for $u_\ell > 0$ with the boundary between ΣR and ΣS regions in Figure 5.5 determined from Eq. (5.18). The same types of solutions are obtained as those in chapter three.

In chapter six, the two-dimensional stability of plane waves in two phase flow is analyzed in a broader context than the single Buckley-Leverett equation. The governing equations used are conservation of mass, Darcy's law and incompressibilty. The analysis presented in chapter six is for variable saturations and is based on Saffman and Taylor's original approach for constant saturations from [52]. The long wave stability analysis determines the sign of the growth rate to leading order (σ_1). The hyperbolic nature of the equations is exploited here as opposed to the asymptotic analysis from [66]. The expression for σ_1 given by Eq. (6.24) provides a boundary between regions of stable and unstable Lax shocks in the case of quadratic relative permeabilities. Once again, numerical simulations illustrate and verify the theoretical results. Values of $\bar{u}_\pm$ are chosen according to the stability boundary in Figure 6.1. Then Figure 6.2 and Figure 6.3 show how the perturbations to the planar front either decay or grow, respectively.

All of the work presented here offers new insights into two phase flow in porous media: understanding new and physically relevant solutions of the modified Buckley-Leverett equation, clarifying the impact of time dependent regularization and providing

a new approach to stability analysis that relies heavily on the structure of two phase flow governing equations. One area of future research is to compare the modified Buckley-Leverett equation of chapters two, three and four with the model of Barenblatt *et al.* [5, 6]. Several sources of experimental data [45, 56, 68] provide a physical baseline with which the models can be measured. Another future project is to investigate the Cauchy problem using the solutions of the Riemann problems included in chapters three and four and wave front tracking, modifying the analysis in [46].

REFERENCES

[1] A. Abeyaratne and J.K. Knowles. Kinetic relations and the propagation of phase boundaries in solids. *Arch. Ration. Mech. Anal.*, 114:119–154, 1991.

[2] D. J. Acheson. *Elementary Fluid Dynamics*. Oxford University Press, New York, 1990.

[3] A. Babchin, I. Brailovsky, P. Gordon, and G. Sivashinsky. Fingering instability in immiscible displacement. *Physical Review E*, 77:026301–1–7, 2008.

[4] G. I. Barenblatt, V. M. Entov, and V. M. Ryzhik. *Theory of Fluid Flows Through Natural Rocks*. Kluwer Academic Publishers, Dordrecht, The Netherlands, 1984.

[5] G.I. Barenblatt, J.G. Azorero, A. De Pablo, and J.L. Vazquez. Mathematical model of the non equilibrium water oil displacement in porous strata. *Applicable Analysis*, 65:19–45, 1997.

[6] G.I. Barenblatt, T.W. Patzek, and D.B. Silin. The mathematical model of nonequilibrium effects in water-oil displacement. *SPE Journal*, pages 409–416, 2003.

[7] J. Bear and A.H.-D. Cheng. *Modeling Groundwater Flow and Contaminant Transport*, volume 23. Springer Science+Business Media B.V., Dordrecht, The Netherlands, 2010.

[8] N. Bedjaoui and P.G. LeFloch. Diffusive-dispersive travelling waves and kinetic relation. ii a hyperbolic-elliptic model of phase-transition dynamics. *Proc. Roy. Soc. Edinburgh*, 132A:545–565, 2002.

[9] T.B. Benjamin, J.L. Bona, and J.J. Mahoney. Model equations for long waves in nonlinear dispersive systems. *Phil. Trans. Roy. Soc. Ser. A*, 272:47–78, 1972.

[10] I. Brailovsky, A. Babchin, M. Frankel, and G. Sivaslinsky. Fingering instability in water-oil displacement. *Transport in Porous Media*, 63(3):363–380, 2006.

[11] R.H. Brooks and A.T. Corey. Properties of porous media affecting fluid flow. *J. Irrigation and Drainage Division*, pages 61–87, 1966.

[12] S. E. Buckley and M. C. Leverett. Mechanism of fluid displacement in sands. *Trans. Amer. Inst. Mining and Metallurgical Eng. Petroleum Development and Techn. Petroleum Div.*, 146:107–116, 1942.

[13] E.D. Chikhliwala, A.B. Huang, and Y.C. Yortsos. Numerical study of the linear stability of immiscilbe displacement in porous media. *Transport in Porous Media*, 3:257–276, 1988.

[14] R. L. Chouke, P. van Meurs, and C. van der Poel. The instability of slow immiscible, viscous liquid-liquid displacements in permeable media. *Petroleum Transactions, AIME*, 216:188–194, 1959.

[15] C.T. Crowe, editor. *Multiphase Flow Handbook*. CRC Press LLC, Boca Raton, Florida, 2005.

[16] C. Cuesta and J. Hulshof. A model problem for groundwater flow with dynamic capillary pressure: stability of traveling waves. *Nonlinear Analysis*, 52:1199–1218, 2003.

[17] C. Cuesta, C. J. van Duijn, and J. Hulshof. Infiltration in porous media with dynamic capillary pressure: travelling waves. *Euro. J. Appl. Math.*, 11:381–397, 2000.

[18] C. M. Cuesta, C. J. van Duijn, and I. S. Pop. Non-classical shocks for Buckley-Levertt: degenerate pseudo-parabolic regularisation. In A. Di Bucchianico, R. M. M. Mattheij, and M. A. Peletier, editors, *Progress in Industrial Mathematics at ECMI 2004*, Mathematics in Industry 8, pages 569–573. European Consortium for Mathematics in Industry, Springer Berlin Heidelberg, 2006.

[19] C.M. Cuesta and I.S. Pop. Numerical schemes for a pseudo-parabolic burgers equation: discontinuous data and long-time behaviour. *J. Comp. Appl. Math.*, 224:269–283, 2009.

[20] P. Daripa and G. Pasa. On capillary slowdown of viscous fingering in immiscible displacement in porous media. *Transport in Porous Media*, 75(1):1–16, 2008.

[21] M. Delshad and G. A. Pope. Comparison of the three-phase oil relative permeability models. *Transport in Porous Media*, 4:59–83, 1989.

[22] D. A. DiCarlo. Experimental measurements of saturation overshoot on infiltration. *Water Resources Research*, 40:W04215.1–W04215.9, 2004.

[23] D.A. DiCarlo. Capillary pressure overshoot as a function of imbition flux and initial water content. *Water Resources Research*, 43:W08402.1–W08402.7, 2007.

[24] D.A. DiCarlo and M.J. Blunt. Determination of finger shape using the dynamic capillary pressure. *Water Resources Research*, 36(9):2781–2785, 2000.

[25] D.A. DiCarlo, R. Juanes, T. LaForce, and T.P. Witelski. Nonmonotonic traveling wave solutions of infiltration into porous media. *Water Resources Research*, 44:W02406–17, 2008.

[26] W.F. Engelberts and L.J. Klinkenberg. Laboratory experiments on the displacement of oil by water from packs of granular material. In *Proceedings Third World Petroleum Congress - Section II*, pages 544–554, The Hague, The Netherlands, 1951. World Petroleum Congress.

[27] Y. Fan. *Dynamic Capillarity in Porous Media - Mathematical Analysis*. PhD thesis, Eindhoven University of Technology, Eindhoven, The Netherlands, January 2012.

[28] F.J. Fayers and J.D. Matthews. Evaluation of normalized stone's methods for estimating three-phase relative permeabilities. *SPE Journal*, 24(2):224–232, 1984.

[29] J. Hagoort. Displacement stability of water drives in water-wet connate-water-bearing reservoirs. *SPE Journal*, 14(1):63–74, 1974.

[30] S. M. Hassanizadeh and W. G. Gray. Mechanics and thermodynamics of multiphase flow in porous media including interphase boundaries. *Adv. Water Resour.*, 13:169–186, 1990.

[31] S. M. Hassanizadeh and W. G. Gray. Thermodynamic basis of capillary pressure in porous media. *Water Resources Research*, 29:3389–3405, 1993.

[32] B. Hayes and P. G. LeFloch. Nonclassical shocks and kinetic relations: finite difference schemes. *SIAM J. Numer. Analysis*, 35:2169–2194, 1998.

[33] B. Hayes and M. Shearer. Undercompressive shocks and Riemann problems for scalar conservation laws with nonconvex fluxes. *Proc. Roy. Soc. Edinburgh Sect. A*, 129:733–754, 1999.

[34] R. Helmig, A. Weiss, and B. J. Wohlmuth. Dynamic capillary effects in heterogeneous porous media. *Computational Geosciences*, 11:261–274, 2007.

[35] S. Hill. Channeling in packed columns. *Chemical Engineering Science*, 1(6):247–253, 1952.

[36] G. M. Homsy. Viscous fingering in porous media. *Ann. Rev. Fluid Mechanics*, 19(1):271–311, 1987.

[37] Z. Hu. Personal communications, 2010-2011.

[38] J. Hulshof and J. R. King. Analysis of a Darcy flow model with a dynamic pressure saturation relation. *SIAM J. Appl. Math.*, 59:318–346, 1998.

[39] D. Jacobs, W. R. McKinney, and M. Shearer. Traveling wave solutions of the modified Korteweg-de Vries-Burgers equation. *J. Differential Equations*, 116:448–467, 1995.

102

[40] G.R. Jerauld, L.C. Nitsche, G.F. Teletzke, H.T. Davis, and L.E. Scriven. Frontal structure and stability in immiscible displacement. In *SPE Enhanced Oil Recovery Symposium*, Tulsa, Oklahoma, 1984. SPE/DOE Fourth Symposium on Enhanced Oil Recovery.

[41] J. S. Kim, K. Kang, and J. S. Lowengrub. Conservative multigrid methods for Cahn-Hilliard fluids. *J. Comp. Phys.*, 193(2):511–543, 2004.

[42] B.H. Kueper and E.O. Frind. An overview of immiscible fingering in porous media. *J. Contaminant Hydrology*, 2:95–110, 1988.

[43] L. W. Lake, R. L. Schmidt, and P. B. Venuto. A niche for enhanced oil recovery in the 1990s. *Oilfield Review*, pages 55–61, 1992.

[44] P. D. Lax. Hyperbolic systems of conservation laws ii. *Comm. Pure and Appl. Math.*, 10:537–566, 1957.

[45] S.S. Le Guen and A.R. Kovscek. Non-equilibrium effects during spontaneous imbibition. *Transport in Porous Media*, 63:127–146, 2006.

[46] P. G. LeFloch. *Hyberbolic Systems of Conservation Laws. The Theory of Classical and Nonclassical Shock Waves*. Lectures Math. Birkhauser Verlag, Zurich, 2002.

[47] S. Manthey, S. M. Hassanizadeh, R. Helmig, and R. Hilfer. Dimensional analysis of two-phase flow including a rate-dependent capillary pressure-saturation relationship. *Adv. Water Resour.*, 31(9):1137–1150, 2008.

[48] A. Mikelic. A global existence result for the equations describing unsaturated flow in porous media with dynamic capillary pressure. *J. Differential Equations*, 248(6):1561 – 1577, 2010.

[49] D. Peaceman. *Fundamentals of Numerical Reservoir Simulation*. Elsevier Scientific Pub. Co., Amsterdam; New York, 1977.

[50] A. Riaz and H. A. Tchelepi. Numerical simulation of immiscible two-phase flow in porous media. *Physics of Fluids*, 18(1):014104, 2006.

[51] A. Riaz and H. A. Tchelepi. Stability of two-phase vertical flow in homogeneous porous media. *Physics of Fluids*, 19(7):072103–1–17, 2007.

[52] P. G. Saffman and G. I. Taylor. The penetration of a fluid into a porous medium or Hele-Shaw cell containing a more viscous liquid. *Proc. Roy. Soc. London Series A*, 245:312–329, 1958.

[53] S. Schecter. The saddle-node separatrix-loop bifurcation. *SIAM J. Math. Anal.*, 18(4):1142–1156, 1987.

[54] S. Schecter. Simultaneous equilibrium and heteroclinic bifurcation of planar vector fields via the Melnikov integral. *Nonlinearlity*, 3:79–99, 1990.

[55] A. E. Scheidegger. *The Physics of Flow Through Porous Media.* University of Toronto Press, New York, 1960.

[56] J.M. Schembre and A.R. Kovscek. Estimation of dynamic relative permeability and capillary pressure from countercurrent imbibition experiments. *Transport in Porous Media*, 65:31–51, 2006.

[57] M. Shearer, D.G. Schaeffer, D. Marchesin, and P. Paes-Leme. Solution of the Riemann problem for a prototype 2×2 system of non-strictly hyperbolic conservation laws. *Arch. Ration. Mech. Anal.*, 97:299–320, 1987.

[58] M. Shearer and J. A. Trangenstein. Loss of real characteristics for models of three-phase flow in a porous medium. *Transport in Porous Media*, 4:499–525, 1989.

[59] D. Silin and T. Patzek. On Barenblatt's model of spontaneous countercurrent imbibition. *Transport in Porous Media*, 54:297–322, 2004.

[60] J. A. Trangenstein. *Numerical Solution of Hyperbolic Partial Differential Equations.* Cambridge University Press, Cambridge, 2007.

[61] U. Trottenberg, A. Schuller, and C. Oosterlee. *Multigrid.* Academic Press, New York, 2005.

[62] C. J. van Duijn, Y. Fan, L. A. Peletier, and I.S. Pop. Travelling wave solutions for degenerate pseudo-parabolic equation modelling two-phase flow in porous media. *CASA Report, Eindhoven Univ. Tech.*, 10-01, 2010.

[63] C. J. van Duijn, L. A. Peletier, and I. S. Pop. A new class of entropy solutions of the Buckley-Leverett equation. *SIAM J. Math. Anal.*, 39(2):507–536, 2007.

[64] S. Wise, J. Kim, and J. S. Lowengrub. Solving the regularized, strongly anisotropic Cahn-Hilliard equation by an adaptive nonlinear multigrid method. *J. Comp. Phys.*, 226(1):414–446, 2007.

[65] A. Wright. Personal communications, 2010-2011.

[66] Y. C. Yortsos and F. J. Hickernell. Linear stability of immiscible displacement in porous media. *SIAM J. Appl. Math.*, 49(3):730–748, 1989.

[67] Y.C. Yortsos and A.B. Huang. Linear-stability analysis of immiscible displacement part 1 - simple basic flow profiles. *SPE Reservoir Engineering*, 1(4):378–390, 1986.

[68] D. Zhou, L. Jia, J. Kamath, and A.R. Kovscek. An investigation of counter-current imbibition processes in diatomite. In *SPE Western Regional Meeting*, Bakersfield, California, 2001. SPE.

APPENDIX

Appendix A

Numerical Code

A.1 Phase Portraits

```
%%%% Generate phase portrait of ODE system for Buckley-Leverett equation
close all; clear all;
format long;
%%%%Setting parameters:  p and q are exponents of relative permeability
%%%%functions, T is tau parameter
uminus=1;
uplus=.025;
M=2;
p=1.5;
q=1.5;
T=1;
fminus=uminus^p/(uminus^p+M*(1-uminus)^q);
fplus=uplus^p/(uplus^p+M*(1-uplus)^q);
```

```
s=(fminus-fplus)/(uminus-uplus);

epsilon=.000001;

%%%%Forwards in time with tspan1, backwards in time with tspan2

tspan1=[0 30];

tspan2=[0 -30];

%%%%Initial conditions for ode45 solver are small perturbations to uplus

%%%%and uminus along the horizontal axis

uazero=[uplus+epsilon; 0];

ubzero=[uplus-epsilon; 0];

uczero=[uminus+epsilon; 0];

udzero=[uminus-epsilon; 0];

%%%%Options command allows parameters to pass to BL function

options=odeset('AbsTol', 1e-7, 'RelTol', 1e-4);

[ta1, ua1]=ode45(@BL, tspan1, uazero, options, s, T, p, M, q, uminus,
fminus);

[ta2, ua2]=ode45(@BL, tspan2, uazero, options, s, T, p, M, q, uminus,
fminus);

[tb1, ub1]=ode45(@BL, tspan1, ubzero, options, s, T, p, M, q, uminus,
fminus);

[tb2, ub2]=ode45(@BL, tspan2, ubzero, options, s, T, p, M, q, uminus,
fminus);

[tc1, uc1]=ode45(@BL, tspan1, uczero, options, s, T, p, M, q, uminus,
fminus);

[tc2, uc2]=ode45(@BL, tspan2, uczero, options, s, T, p, M, q, uminus,
fminus);
```

```
[td1, ud1]=ode45(@BL, tspan1, udzero, options, s, T, p, M, q, uminus,
fminus);
[td2, ud2]=ode45(@BL, tspan2, udzero, options, s, T, p, M, q, uminus,
fminus);
plot(ua1(:,1), ua1(:,2), ua2(:,1), ua2(:,2), ub1(:,1), ub1(:,2),...
ub2(:,1), ub2(:,2), uc1(:,1), uc1(:,2), uc2(:,1), uc2(:,2), ...
ud1(:,1), ud1(:,2), ud2(:,1), ud2(:,2))
axis([01 1 -3 3])




%%%BL function is ODE system from traveling wave solutions to Buckley-
%%%%Leverett PDE
function uprime=BL(t, u, s, T, p, M, q, uminus, fminus)
    uprime=[u(2); (1/(.2*sqrt(s*T)))*u(2)+(u(1)^p+M*(1-u(1))^q)/((.2^2)*...
    u(1)^p*(1-u(1))^q)*(s*(u(1)-
    uminus)-u(1)^p/(u(1)^p+M*(1-u(1))^q)+fminus)];
end
```

A.2   Finding Saddle-Saddle Connections

```
%%%%This script calculates the values of u_alpha and u_gamma as
%%%%functions of Uminus
Uminus=0:.04:1;
l=length(Uminus);
for g=1:l
```

```matlab
        syms a
        solveforalpha=double(solve(fprime(a)*(a-Uminus(g))-f(a)+f(Uminus(g))));
        done=0;
        while ~done
            for h=1:length(solveforalpha)
                if solveforalpha(h)>0 && solveforalpha(h)~=Uminus(g)
                    alpha(g)=solveforalpha(h);
                    done=1;
                end
            end
        end
end
gamma=zeros(length(Uminus),1);
for r=1:(length(Uminus)+1)/2
    gamma(r)=1;
end
tol=10^-8;
for m=2:l-1
    syms b
    solveforgamma=double(solve(fprime(Uminus(m))*(b-Uminus(m))-f(b)+...
    f(Uminus(m))));
    for n=1:length(solveforgamma)
        if solveforgamma(n)<1 && abs(solveforgamma(n)-Uminus(m))>tol...
         && solveforgamma(n)>0
                gamma(m)=solveforgamma(n);
```

```matlab
        end

    end

end



%%This script uses MATLAB's contour command to calculate the values

%%of uplus and uminus that satisfy h=0, i.e. when  tau=infinity.

uminusvector=0:.005:1;

uplusvector=0:.005:1;

hmatrix=zeros(length(uplusvector), length(uminusvector));

for j=1:length(uplusvector)

    for k=1:length(uminusvector)

        hmatrix(j,k)=integral(uminusvector(k), uplusvector(j));

     end

end

v=[0 0];

contour(uminusvector, uplusvector, hmatrix, v);

axis([0 1 0 1]);



%%%%This script finds a saddle-saddle connection between uplus and

%%%%fixed uminus for tau<infinity.

Uminus=sparse(30,1);

Uplus=sparse(30,1);

tau=1;
```

```
tol=.0001;

for j=1:length(Uminus)

    uminus=.05+.01*j

uplus1=.0000000001

s1=(f(uminus)-f(uplus1))/(uminus-uplus1);

d1=distbt(uplus1, uminus, tau)

uplus2=.9999999999

s2=(f(uminus)-f(uplus2))/(uminus-uplus2);

d2=distbt(uplus2, uminus, tau)

if d1>0 && d2>0

    disp('No saddle-to-saddle connection exists in the interval of...
 uplus values')

elseif d1<0 && d2<0

    disp('No saddle-to-saddle connection exists in the interval of ...
uplus values')

else disp('There exists a saddle-to-saddle connection between these...
 values of uplus')

end

done=0;

while ~done

if d1>0 && d2>0

    done=1;

elseif d1<0 && d2<0

    done=1;

elseif abs(d1)<=tol
```

```
    done=1;
elseif abs(d2)<=tol
    done=1;
else uplusave=.5*(uplus1+uplus2)
    dave=distbt2(uplusave, uminus, tau)
     if dave<0
     uplus1=uplusave
     d1=dave
     elseif dave>0
     uplus2=uplusave
     d2=dave
     end
end
end
if abs(d1)<abs(d2)
    Uplus(j)=uplus1
else Uplus(j)=uplus2
end
Uminus(j)=uminus
end
filedate=datestr(now,30)
save(filedate, 'Uminus', 'Uplus')



%%%%dist function calculates distance between stable and unstable
```

```matlab
%%%manifolds for uplus and uminus
function dist=distbt(uplus, uminus, tau)
format long;
s=(f(uplus)-f(uminus))/(uplus-uminus);
p=s*tau;
%Solve for middle equilibrium um by solving linear equation of y-f(uplus)
%=s(x-uplus) with y=f(um) and x=um
syms a
umlist=sort(double(solve(f(a)-s*a+s*uminus-f(uminus))));
um=umlist(2);
%Set up system of first-order ODEs symbolically so we can determine
%Jacobian later
syms U1 U2;
U=[U1, U2];
Uprime=[U2; (1/sqrt(p))*U2+(1/H(U1))*(s*(U1-uminus)-f(U1)+f(uminus))];
%Determine Jacobian evaluated at (uminus,0) and (uplus,0) then find
%slopes of eigenvectors corresponding to unstable and stable manifolds
J=jacobian(Uprime, U);
Jplus=subs(J, {U1, U2}, {uplus, 0});
[~,D]=eig(Jplus);
mplus=D(1,1);
Jminus=subs(J, {U1, U2}, {uminus, 0});
[~,E]=eig(Jminus);
mminus=E(2,2);
%Use (uminus+.00001,0) and (uplus-.00001) to get trajectories
```

```
upluspert=mplus*.00001;

uminuspert=mminus*.00001;

%Set tolerances for ode solver

options= odeset('AbsTol', 1e-10, 'RelTol', 1e-10);

%xif goes forward to generate unstable manifold from (uminus,0)

xif=0:.001:80;

uminus0=[uminus+.0001; uminuspert];

%xib goes backward to generate stable manifold into (uplus,0)

xib=80:-.001:0;

uplus0=[uplus-.0001; -upluspert];

%ODE SOLVERS

[~, uminustraj]=ode15s(@PS, xif, uminus0, options, p, s, uminus,...
 f(uminus));

[~, uplustraj]=ode15s(@PS, xib, uplus0, options, p, s, uminus,...
 f(uminus));

%Find trajectory value (vertical axis) on unstable manifold closest to

%u=um; uplush is vector of values along horizontal axis (u) from ODE

%solver; uplusv is vector of values along vertical axis (v=uprime) from

% ODE solver

uplush=uplustraj(:,1);

uplusv=uplustraj(:,2);

j=1;

vplus=uplusv(1);

while uplush(j)>=um

    vplus=uplusv(j+1);
```

```
    j=j+1;
end
%Find trajectory value (vertical axis) on stable manifold closest to
%u=um; uminush, uminusv are horizontal and vertical components,
%respectively, of trajectory from ODE solver
uminush=uminustraj(:,1);
uminusv=uminustraj(:,2);
k=1;
vminus=uminusv(1);
while uminush(k)<=um
    vminus=uminusv(k+1);
    k=k+1;
end
%Calculate vertical distance between uplus and uminus trajectories at
%u=um
dist=vminus-vplus;
end



% %%%f function calculates the value of the flux function for a given
%%%%value of u
function  y = f(u)
M=2;
p=2;
q=2;
```

```
y=u.^p./(u.^p+M*(1-u).^q);

end



%%%% fprime function calculates the value of the derivative of the

%%%%flux function for a given value of u in the case of quadratic relative

%%%%permabilities

function  y = fprime(u)

M=2;

y=((u.^2+M*(1-u).^2).*(2*u)-(u.^2).*(2*u-2*M*(1-u)))./((u.^2+M*(1-u).^2).^2);

%y=0*u;

end
```

A.3   Numerical Simulations from Chapter Three

```
%%%%This script is the master file for 1-d PDE simulations of modified

%%%%Buckley-Leverett equation

close all; clear all;

format long

N=200;

h=1/N;

a=-2;

b=4;

X=a:h:b;

k=.1*h^2;
```

```
ul=.9;

ur=.4;

tau=1;

M=2;

epsilon=.05;

%IC

 gamma=250;

 for j=1:length(X)

     Uo(j,1)=(ul-(ur+ul)/2)*-tanh(gamma*X(j))+(ur+ul)/2;

 end

%P is an empty matrix with 1s on superdiagonal, M is an empty matrix with

%1s on subdiagonal

P=diag(ones(length(X)-1,1),1);

Mmatrix=diag(ones(length(X)-1,1),-1);

eps_step=1e-8;

NN=10;

    %%%%updating U

    %%%%U_old is previous time step, define new variable Uo to be update

    %%%%but U_old doesn't change

T=400000;

for n=1:T

     U_old=Uo;

     U_old_p=P*U_old;

     U_old_p(length(X))=U_old(length(X));

     U_old_pp=P*U_old_p;
```

```matlab
    U_old_pp(length(X))=U_old_p(length(X));

    U_old_m=Mmatrix*U_old;

    U_old_m(1)=Uo(1);

    U_old_mm=Mmatrix*U_old_m;

    U_old_mm(1)=U_old_m(1);

for nn=1:NN

    Up=P*Uo;

    Upp=P*Up;

    Um=Mmatrix*Uo;

    Umm=Mmatrix*Um;

    %%Boundary conditions - set for Um and Up

    Um(1)=Uo(1);

    Umm(1)=Um(1);

    Umm(2)=Um(2);

    Up(length(X))=Uo(length(X));

    Upp(length(X))=Up(length(X));

    Upp(length(X)-1)=Up(length(X)-1);

    Jacob=jacob(Upp,Up,Uo,Um,Umm,U_old_pp,U_old_p,U_old,U_old_m,...

    U_old_mm,epsilon,h,tau,k);

    GG=G(Upp,Up,Uo,Um,Umm,U_old_pp,U_old_p,U_old,U_old_m,U_old_mm,...

    epsilon,k,h,tau);

U_new=Uo-Jacob\GG;

    if norm(Uo-U_new,inf)<eps_step

        break;

    elseif nn==NN
```

```matlab
        error('Newtons method did not converge');
    end

    Uo=U_new;
end
%%%Create new matrix UU to store only every mod n time step output
if mod(n,100000)==0
    UU(:,n/100000)=Uo;
end
end
filedate=datestr(now,30)
save(filedate, 'UU', 'ul', 'ur', 'h')




%%%%G function is right hand side of discritization for modified Buckley-
%%%%Leverett PDE
function rhs=G(Upp,Up,Uo,Um,Umm,U_old_pp,U_old_p,U_old,U_old_m,...
U_old_mm,epsilon,k,h,tau)
format long
lr=length(U_old);
Grhs=zeros(lr,1);
%Complete discritization
Grhs=Uo-U_old+(k/(12*h))*(-1*f(Upp)+8*f(Up)-8*f(Um)+f(Umm))-...
    (epsilon*k/(h^2))*(H(.5*(Up+Uo)).*(Up-Uo)-H(.5*(Um+Uo)).*(Uo-Um))-...
    (epsilon^2*tau/(h^2))*(H(.5*(Uo+Up)).*(Up-Uo-U_old_p+U_old)-...
    H(.5*(Um+Uo)).*(Uo-Um-U_old+U_old_m));
```

```
rhs=Grhs;



%%%%jacob function is Jacobian of discritization in G function
function J=jacob(Upp,Up,Uo,Um,Umm,U_old_pp,U_old_p,U_old,U_old_m,...
U_old_mm,epsilon,h,tau,k)
format long
lr=length(U_old);
jac=sparse(length(U_old),length(U_old));
%%Derivative of G with respect to Umm
Ju(:,1)=(k/(12*h))*(fprime(Umm));
%%Derivative of G with respect to Um
Ju(:,2)=(k/(12*h))*-8*fprime(Um)-epsilon*k/(h^2)*-1*(H(.5*(Um+Uo))*-1+...
(Uo-Um).*Hprime(.5*(Um+Uo))*.5)-...
    epsilon^2*tau/(h^2).*-1*(H(.5*(Um+Uo))*-1+(Uo-Um-U_old+U_old_m)...
    .*Hprime(.5*(Um+Uo))*.5);
%%Derivative of G with respect to Uo
Ju(:,3)=1-...
    epsilon*k/(h^2)*(H(.5*(Up+Uo))*-1+(Up-Uo).*Hprime(.5*(Up+Uo))*.5-...
    (H(.5*(Um+Uo))*1+(Uo-Um).*Hprime(.5*(Um+Uo))*.5))-...
    epsilon^2*tau/(h^2)*(H(.5*(Uo+Up))*-1+(Up-Uo-U_old_p+U_old)...
    .*Hprime(.5*(Uo+Up))*.5-...
    (H(.5*(Um+Uo))*1+(Uo-Um-U_old+U_old_m).*Hprime(.5*(Um+Uo))*.5));
%%Derivative of G with respect to Up
```

```
Ju(:,4)=(k/(12*h))*8*fprime(Up)-epsilon*k/(h^2)*(H(.5*(Up+Uo))*1+(Up-Uo)...

.*Hprime(.5*(Up+Uo))*.5)-...

    epsilon^2*tau/(h^2)*(H(.5*(Uo+Up))*1+(Up-Uo-U_old_p+U_old)...

    .*Hprime(.5*(Uo+Up))*.5);

%%Derivative of G with respect to Upp

Ju(:,5)=(k/(12*h))*-1*fprime(Upp);

%For implicit flux, leave top 2 and bottom 2 rows empty

for j=2:lr-3

    jac(j+1,j-1:j+3)=Ju(j+1,:);

end

%Reassign diagonal values at top and bottom when using implicit flux

jac(1,1)=Ju(1,3);

jac(1,2)=Ju(1,4);

jac(1,3)=Ju(1,5);

jac(2,1)=Ju(2,2);

jac(2,2)=Ju(2,3);

jac(2,3)=Ju(2,4);

jac(2,4)=Ju(2,5);

jac(lr-1,lr-3)=Ju(lr-1,1);

jac(lr-1,lr-2)=Ju(lr-1,2);

jac(lr-1,lr-1)=Ju(lr-1,3);

jac(lr-1,lr)=Ju(lr-1,4);

jac(lr,lr-2)=Ju(lr,1);

jac(lr,lr-1)=Ju(lr,2);

jac(lr,lr)=Ju(lr,3);
```

```
J=jac;



%%%%H function calculates the value of the nonlinear dispersion

%%%%coefficient for a given value of u

function y = H(u)

M=2;

y=(u.^2.*(1-u).^2)./(u.^2+M*(1-u).^2);

end



%%%% Hprime function is the derivative of the nonlinear dispersion

%%%%coefficient for a given value of u

function y = Hprime(u)

M=2;

y=((u.^2+M*(1-u).^2).*(u.^2.*-2.*(1-u)+(1-u).^2.*2.*u)-u.^2.*(1-u).^2...

.*(2*u-2*M*(1-u)))./((u.^2+M*(1-u).^2).^2);

end
```